UNIVERSITY OF CALGARY

Seismic acquisition footprint: modelling and mitigation

by

Joanna Kathleen Cooper

A THESIS

SUBMITTED TO THE FACULTY OF GRADUATE STUDIES

IN PARTIAL FULFILMENT OF THE REQUIREMENTS FOR THE

DEGREE OF MASTER OF SCIENCE

DEPARTMENT OF GEOSCIENCE

CALGARY, ALBERTA

APRIL, 2010

© Joanna Kathleen Cooper 2010



UNIVERSITY OF
CALGARY

The author of this thesis has granted the University of Calgary a non-exclusive license to reproduce and distribute copies of this thesis to users of the University of Calgary Archives.

Copyright remains with the author.

Theses and dissertations available in the University of Calgary Institutional Repository are solely for the purpose of private study and research. They may not be copied or reproduced, except as permitted by copyright laws, without written authority of the copyright owner. Any commercial use or re-publication is strictly prohibited.

The original Partial Copyright License attesting to these terms and signed by the author of this thesis may be found in the original print version of the thesis, held by the University of Calgary Archives.

Please contact the University of Calgary Archives for further information:
E-mail: uarc@ucalgary.ca
Telephone: (403) 220-7271
Website: http://archives.ucalgary.ca

Abstract

Acquisition footprint is a phenomenon occurring in seismic images whereby amplitude variations relate to the survey geometry, rather than solely to the physical properties of the subsurface. In this study, 2D and 3D exhaustive datasets, exhibiting no spatial aliasing in either source or receiver gathers, were produced via numerical modelling and were subsequently decimated to examine the effect of spatial sampling on acquisition footprint. The exhaustive and decimated datasets were processed using common-midpoint stacking, poststack migration, and prestack migration. Footprint artefacts were found to depend strongly on the processing flow applied to the data. Footprint consisting of spatially periodic amplitude variations was prominent in only the decimated datasets, and was most severe in prestack-migrated data. In 2D, spatial aliasing of receiver gathers was coincident with the presence of footprint. Delta-ratio weighting, a prestack migration weighting scheme developed in the course of this study, was found to reduce footprint artefacts significantly.

Acknowledgements

Foremost, I thank my supervisors, Dr. Gary Margrave and Dr. Don Lawton, for their guidance and patience, for helping me learn so much, and for providing me with such an enriched experience during my time as their student.

I am also grateful to the faculty, staff, and students of CREWES (the Consortium for Research in Elastic Wave Exploration Seismology) and the Department of Geoscience, in particular: Kevin Hall for helping me with my many "quick" technical support questions; Laura Baird and Louise Forgues for keeping me on the administrative straight-and-narrow; and Kelley Classen and Heather Ainsworth for providing me with daily sanity checks.

A portion of this study was undertaken as part of a MITACS Internship, in partnership with Talisman Energy, Sensor Geophysical, Divestco, and Husky Energy; I thank MITACS (Mathematics of Information Technology and Complex Systems) and Talisman for financial support, and David D'Amico (Talisman), Peter Cary and Rod Couzens (Sensor), Mike Perz and Ye Zheng (Divestco), and Larry Mewhort and Ken Hedlin (Husky) for their helpful suggestions and contributions to the project.

Additional financial support was provided by the industrial sponsors of CREWES, the industrial sponsors of POTSI (Pseudodifferential Operator Theory in Seismic Imaging), as well as by NSERC (the Natural Sciences and Engineering Research Council of

Canada), AIF (the Alberta Ingenuity Fund), and SEG (the Society of Exploration Geophysicists).

Finally, and most importantly, I thank my family for their support.

Table of Contents

Approval Page ii
Abstract iii
Acknowledgements iv
Table of Contents vi
List of Tables viii
List of Figures and Illustrations ix
List of Symbols, Abbreviations and Nomenclature xv

CHAPTER ONE: INTRODUCTION 1
1.1 Introduction 1
1.2 Seismic acquisition footprint 2
1.2.1 Possible causes 4
1.2.2 Spatial aliasing and the exhaustive dataset 5
1.2.3 Strategies for footprint removal or prevention 10
1.3 Objectives and scope of project 13
1.4 Organisation of thesis 15

CHAPTER TWO: MODELLING METHODS 17
2.1 Introduction 17
2.2 Modelling exhaustive datasets 19
2.3 Kirchhoff modelling 21
2.4 Rayleigh-Sommerfeld modelling 26
2.5 2D model 30
2.5.1 2D Geological Model 35
2.6 3D model 39
2.7 Summary 55

CHAPTER THREE: PROCESSING OF MODELLED DATA AND OBSERVED FOOTPRINT 56
3.1 Introduction 56
3.2 Processing methods 56
3.2.1 CMP stacking 57
3.2.2 Poststack migration 58
3.2.3 Prestack migration 59
3.3 2D results 65
3.4 3D results 75
3.5 Summary 88

CHAPTER FOUR: DELTA WEIGHTING METHOD AND RESULTS 90
4.1 Introduction 90
4.2 Delta weighting 91
4.2.1 Illumination compensation 91
4.2.2 Delta angles 93
4.2.3 Delta distributions and weights 98
4.2.4 Implementation of weights 104

4.3 Application in 2D.....105
4.4 Application in 3D.....115
4.5 Comparison to 3D common-offset weighting 119
4.6 Application to additional 3D decimations 125
4.7 Discussion.....131
4.8 Summary.....134

CHAPTER FIVE: CONCLUSIONS 136

REFERENCES 141

List of Tables

Table 2.1: The number of traces required for an exhaustive survey of size L^2 having square spatial sample size of Δx. Trace numbers are given in millions..... 20

Table 2.2: Velocity, depth, and reflector information for the 3D model. 40

Table 3.1: Summary of processing methods applied to the model data. 77

List of Figures and Illustrations

Figure 1.1: Example of acquisition footprint consisting of periodic amplitude variations on a horizon slice from a 3D volume (courtesy Talisman Energy Inc.). ... 3

Figure 1.2: Typical orthogonal 3D survey geometry. Source positions are red stars and receiver positions are blue triangles. ... 9

Figure 1.3: Data with spatial aliasing a) before migration, and b) after migration; corresponding f-k amplitude spectra c) before migration, and d) after migration, after Bancroft (2006). ... 10

Figure 2.1: The logarithm of the number of traces required to form an exhaustive 3D dataset is shown versus velocity. Assumed here are a maximum frequency of 100Hz and an aperture of 1km. ... 21

Figure 2.2: The geometry relevant to the derivation of the Kirchhoff diffraction formula for the classic case of an opaque screen with a hole, after Ersoy (2007). ... 23

Figure 2.3: Rayleigh-Sommerfeld modelling is depicted as described by equation (2.14). The source wavefield is extrapolated by phase shift to the screen. At the screen it is multiplied by the function ρ describing the "transmissivity" of the screen, and then it is phase-shifted to the observation plane. ... 28

Figure 2.4: Rayleigh-Sommerfeld modelling applied to the seismic reflection case. Here the screen of Figure 2.3 becomes the reflector and the screen transmissivity becomes the reflectivity. Also the source and observation planes become identical. ... 29

Figure 2.5: Source wavelet and wavelet amplitude spectrum. ... 33

Figure 2.6: 2D geological model used throughout this study, displaying velocities and densities. ... 36

Figure 2.7: Model shot record of flat reflector with channel from x=175-225m. ... 37

Figure 2.8: Migrated shot record from channel model. Channel is located from x=175-225m. ... 38

Figure 2.9: The velocity profile chosen for the 3D model. ... 40

Figure 2.10: The third reflector, placed at a depth of 200m in the model. The black colour corresponds to a reflection coefficient of +0.1 whereas white is -0.1. ... 41

Figure 2.11: Rayleigh-Sommerfeld modelling compared to Kirchhoff at two different grid spacings. Each panel is a constant-time slice through a 3D response. ... 43

Figure 2.12: An entire 3D shot record for a source location at the center of Figure 2.10. Each small hyperbolic event is a reflection as recorded on a line y=constant. The more complicated nature of the third reflector, compared to the first two, is readily apparent. 44

Figure 2.13: The 3D response of Figure 2.12 is shown isolated along a single 2D receiver line at x=200m. 45

Figure 2.14: The 3D response of Figure 2.12 is shown isolated along a single 2D line at y=200m. 45

Figure 2.15: A time slice at t=0.2 seconds through the 3D source record of Figure 2.12. 46

Figure 2.17: A single depth slice at 100m from a 3D migration of the data of Figure 2.12. The crossing red lines locate the source position and the red square denotes the boundary of the CMPs expected. This was modelled as a featureless reflector with a negative reflection coefficient. 47

Figure 2.18: Similar to Figure 2.17 except that the depth slice is at 180m, where a featureless reflector with a positive reflection coefficient was modelled. The zero phase (non causal) wavelet has allowed the reflector at a depth of 200m (Figure 2.19) to influence this image. 48

Figure 2.19: Similar to Figure 2.17 and Figure 2.18 except that the depth slice is at 200m, where the reflector of Figure 2.10 was modelled. 48

Figure 2.20: A 3D source record for a source located at x=y=0m (Figure 2.10). Compare with Figure 2.12. 49

Figure 2.21: A 2D receiver line sorted from the data of Figure 2.20. The receivers were all at x=0m. 50

Figure 2.22: A 2D receiver line sorted from the data of Figure 2.20 for receivers at y=0m. 50

Figure 2.23: A time slice from the data of Figure 2.20, taken at t=0.2 seconds. 51

Figure 2.24: A depth slice at 100m after 3D migration of the data in Figure 2.20. 51

Figure 2.25: A depth slice at 180m after 3D migration of the data in Figure 2.20. 52

Figure 2.26: A depth slice at 200m after 3D migration of the data in Figure 2.20. 52

Figure 2.27: Geometry of a) the exhaustive survey and b) the decimated survey. 54

Figure 2.28: The f-k spectra for slices at x=240m through 3D shot records from a) the exhaustive dataset and b) the decimated dataset, produced by a source at (240m, 0m). 54

Figure 3.1: Illustration of source, receiver, and image point geometry in prestack migration, after Bleistein et al. (2001). 64

Figure 3.2: Common-midpoint stacks created using shot spacings of a) 5m, b) 10m, c) 25m, d) 50m, e) 100m, and f) 200m. Mean scaling applied. 67

Figure 3.3: Poststack migrations applied to stacks created using shot spacings of a) 5m, b) 10m, c) 25m, d) 50m, e) 100m, and f) 200m. Mean scaling applied. 68

Figure 3.4: Prestack-migrated sections created using a) 5m, b) 10m, c) 25m, d) 50m, e) 100m, and f) 200m shot intervals. 71

Figure 3.5: Common-receiver gathers created using a) 5m, b) 10m, c) 25m, d) 50m, e) 100m, and f) 200m shot intervals. 72

Figure 3.6: The f-k spectra of common-receiver gathers created using a) 5m, b) 10m, c) 25m, d) 50m, e) 100m, and f) 200m shot intervals. 73

Figure 3.7: Time slices from UofC stacks for the exhaustive and decimated datasets. 78

Figure 3.8: Depth slices from UofC poststack migrations for the exhaustive and decimated datasets. 79

Figure 3.9: Depth slices from UofC prestack migrations for the exhaustive and decimated datasets. 80

Figure 3.10: Time slices from Algorithm A prestack migrations for the exhaustive and decimated datasets. 81

Figure 3.11: Time slices from Algorithm B prestack migrations for the exhaustive and decimated datasets. 82

Figure 3.12: Percent difference plots for stacks. 85

Figure 3.13: Percent difference plots for poststack migrations. 86

Figure 3.14: Percent difference plots for prestack migrations at the shallow featureless reflector (left-hand column) and at the channel (right-hand column). Each row compares a particular migration algorithm run on the decimated dataset with the same algorithm run on the exhaustive dataset. 87

Figure 4.1: Delta angles in 2D and 3D, defining the orientation of the vector bisecting the opening angle between source and receiver rays. The positions of sources and receivers on the surface determine the distribution of delta angles on the imaging hemisphere. 94

Figure 4.2: Common-midpoint fold for the exhaustive (left) and decimated (right) surveys from the 3D footprint simulation, as an example of delta hit count maps changing between exhaustive and decimated surveys, in this case for delta dip=0. 96

Figure 4.3: 2D migration impulse response divided into individual delta angle contributions. Each delta bin has a width of 25°. Delta angles above 60° were attenuated by the dip limit parameter in the migration. Delta is determined by the opening angle bisector vector (refer to Figure 4.1), which is also the normal to the impulse response. 97

Figure 4.4: Delta bin hit count distributions for two image points from the 2D model. Left (a): image point at x=2.5m, z=200m, at the edge of the model. Right (b): x=200m, z=200m, in the middle of the model. The six panels for each image point are the exhaustive dataset, and the 10m, 25m, 50m, 100m, and 200m decimations. 99

Figure 4.5: Fold weights (a, b) and ratio weights (c, d) for the two image points from Figure 4.4 for the exhaustive and decimated surveys. Left (a, c): image point at x=2.5m, z=200m, at the edge of the model. Right (b, d): x=200m, z=200m, in the middle of the model. Fold weights appear to emphasize large deltas in the middle of the model, while ratio weights down-weight the large deltas. Ratio weights do nothing to the exhaustive survey. 101

Figure 4.6: Hit count maps for delta dip angles between 0 and 0.01 degrees for a shot located at x=240m, y=400m (position indicated by the yellow star), from the exhaustive dataset (left) and from the decimated dataset (right). Receiver locations for both datasets are indicated by green dots. These essentially zero delta dip hit count maps are identical to common-midpoint fold maps for the shots. 102

Figure 4.7: Hit count maps for non-zero delta dip angles for a shot located at x=240m, y=400m, from the exhaustive dataset (top six panels) and from the decimated dataset (bottom six panels). The six delta dip bins were [0.01, 10), [10, 20), [20, 30), [30, 40), [40, 60), and [60, 90] degrees. 103

Figure 4.8: Repeat display of images produced from stacking migrated shot records from the 2D exhaustive dataset and the five 2D decimated datasets, using the prestack migration method from Chapter 3. 107

Figure 4.9: Images produced from stacking migrated shot records from the exhaustive dataset and the five decimated datasets. Similar to Figure 4.8 except here delta-ratio weights were applied when migrated traces were stacked. Compared to Figure 4.8, residual migration wavefronts are less pronounced. 108

Figure 4.10: Same as Figure 4.9 except delta-fold weights were used instead of delta-ratio weights. Fold weights do not appear to be as effective as ratio weights in reducing footprint, though they do compensate for limited aperture more effectively than the ratio weights. 109

Figure 4.11: Detailed comparison of images produced without delta weights (left), with delta-ratio weights (middle), and with delta-fold weights (right), for the 50m decimated dataset (top row) and the 100m decimated dataset (bottom row). 110

Figure 4.12: Same as Figure 4.9 except 1 degree delta bins were used instead of 5 degree bins for calculating delta-ratio weights. 111

Figure 4.13: Same as Figure 4.9 except 15 degree delta bins were used instead of 5 degree bins for calculating delta-ratio weights. 112

Figure 4.14: Detailed comparison of using different delta bin widths for calculation of delta-ratio weights for the 50m decimated dataset (top row) and the 100m decimated dataset (bottom row). The three different bin widths used were 1 degree (left), 5 degrees (middle), and 15 degrees (right). 113

Figure 4.15: Similar to Figure 4.9 except the absolute value of delta was used in binning instead of signed delta. This simulates not considering the azimuth of the delta angle when computing the delta-ratio weights. 114

Figure 4.16: Detailed comparison of images produced without delta weights (left), with signed delta-ratio weights (middle), and with absolute value of delta-ratio weights (right), for the 50m decimated dataset (top row) and the 100m decimated dataset (bottom row). 115

Figure 4.17: Repeat display of depth slices from UofC prestack migrations for the exhaustive and decimated datasets, from Chapter 3. 117

Figure 4.18: Depth slices from delta-ratio weighted prestack migrated images at the three reflectors: 100m featureless (left), 180m featureless (middle), and 200m channel (right). From top to bottom, the azimuthal binning involved 1, 4, 8, and 16 azimuth bins. 118

Figure 4.19: Depth slices at 100m, 180m, and 200m from delta-fold weighted prestack migrations of the decimated dataset. 119

Figure 4.20: Depth slices from common-offset-weighted prestack migrated images at the three reflectors: 100m featureless (left), 180m featureless (middle), and 200m channel (right). From top to bottom, the offset binning involved 1, 2, and 6 offset bins. 121

Figure 4.21: Aperture estimate (top) and aperture-removed migrated depth slices (bottom) at 100m, 180m, and 200m for the delta-ratio weighted prestack migration of the decimated dataset with 8 azimuth bins. 123

Figure 4.22: Percent difference between migrated depth slices and the true reflectivity at 100m (left), 180m (middle), and 200m (right). Top to bottom: no weights (reference), delta-ratio weights, delta-fold weights, and common-offset weights.. 124

Figure 4.23: Geometry of decimated surveys with a hole introduced by removing shots (a) and by moving shots (b). 125

Figure 4.24: Prestack-migrated depth slices at 100m (left), 180m (middle), and 200m (right) for the survey with removed shots. Top to bottom: no weights (reference), delta-ratio weights, delta-fold weights, and common-offset weights.. 127

Figure 4.25: Prestack-migrated depth slices at 100m (left), 180m (middle), and 200m (right) for the survey with moved shots. Top to bottom: no weights (reference), delta-ratio weights, delta-fold weights, and common-offset weights. 128

Figure 4.26: Percent difference between migrated depth slices and the true reflectivity at 100m (left), 180m (middle), and 200m (right) for the survey with removed shots. Top to bottom: no weights (reference), delta-ratio weights, delta-fold weights, and common-offset weights. 129

Figure 4.27: Percent difference between migrated depth slices and the true reflectivity at 100m (left), 180m (middle), and 200m (right) for the survey with moved shots. Top to bottom: no weights (reference), delta-ratio weights, delta-fold weights, and common-offset weights. 130

List of Symbols, Abbreviations and Nomenclature

Symbol	Definition
AVO	Amplitude Variation with Offset
CMP	Common-midpoint
CO	Common-offset
COV	Common-offset-vector
CREWES	Consortium for Research in Elastic Wave Exploration Seismology
f	Frequency
k	Wavenumber
NMO	Normal Moveout
t	Time
v	Velocity
ω	Angular frequency
x,y	Horizontal position
z	Depth

Chapter One: Introduction

1.1 Introduction

In exploration seismology, a source is initiated at specific locations on the Earth's surface, sending seismic waves into the ground. In the subsurface, the waves reflect from interfaces between different rock layers, and the reflected waves are recorded with geophones at the surface. The data collected by the geophones are processed to make an image of the Earth's subsurface. Historically, seismic data were used in the oil and gas industry for the primary purpose of delineating subsurface structures using traveltime information; the amplitudes contained in the data were not particularly important. Now, there is increasing emphasis on the amplitudes in the seismic data, for the purpose of identifying subtle stratigraphic plays, where small changes in amplitudes can indicate an important change in rock or fluid properties.

Often, and problematically, seismic interpreters observe regular stripes or grid patterns imprinted on the seismic images, caused by amplitudes in the processed data varying in relation to the acquisition geometry, i.e. the locations of the sources and receivers used in the survey, instead of varying in a geologically reasonable way related to changes in the rocks or fluids in the subsurface. This phenomenon is known as seismic acquisition footprint (Sheriff, 2002), and its presence makes it difficult to separate artefacts connected to the survey geometry from the true subsurface response, thereby increasing uncertainty in the interpretation of the seismic images. As a result, research into the causes and prevention, or alternatively remediation, of acquisition footprint is important, and is the focus of this thesis.

1.2 Seismic acquisition footprint

Seismic acquisition footprint refers to artefacts observable in a final seismic image resulting from the acquisition geometry of the seismic survey. The acquisition geometry refers to the locations of the sources and receivers used in the survey. Each seismic trace (recorded time series) is associated with a particular source location and a particular receiver location; these two locations also define the source-receiver midpoint (location midway between source and receiver), offset (distance between source and receiver), and azimuth (direction of the line connecting source and receiver). Usually, more than one trace in the survey will have the same midpoint; the number of traces sharing a given midpoint is referred to as the fold at that midpoint. Therefore, in addition to describing the source and receiver locations in the survey, the acquisition geometry also refers to how fold, offsets, and azimuths are distributed around the survey area. During seismic processing, the raw recorded traces are converted to a dataset with a single trace per midpoint, or if midpoints are irregularly distributed, per bin centre. The processing steps are designed to produce amplitudes in the processed dataset that are equal to a bandlimited version of the subsurface reflectivity. When seismic acquisition footprint is present, the processed image will also contain artefacts. These artefacts generally consist of amplitude variations that correlate with source and receiver locations, and therefore mask the true subsurface response.

Though acquisition footprint is often recognizable in seismic data, the exact nature of the effect of acquisition geometry on seismic imaging is not very well understood. An example of acquisition footprint is shown in Figure 1.1. The periodicity of the amplitude variations makes it clear that they are unrelated to changes in elastic

properties of the subsurface, but rather are artefacts of the choice of acquisition geometry and processing techniques. Footprint is often most obvious on time, depth, or horizon slices from 3D volumes, but the problem is also present in 2D data. The artefacts are observed to occur at many stages of processing, including stacked sections, poststack migrations, and prestack migrations. Strong acquisition footprint can have a negative effect on the interpretation of the seismic data, especially when techniques such as AVO (amplitude variation with offset) or seismic coherency are used (Marfurt et al., 1998).

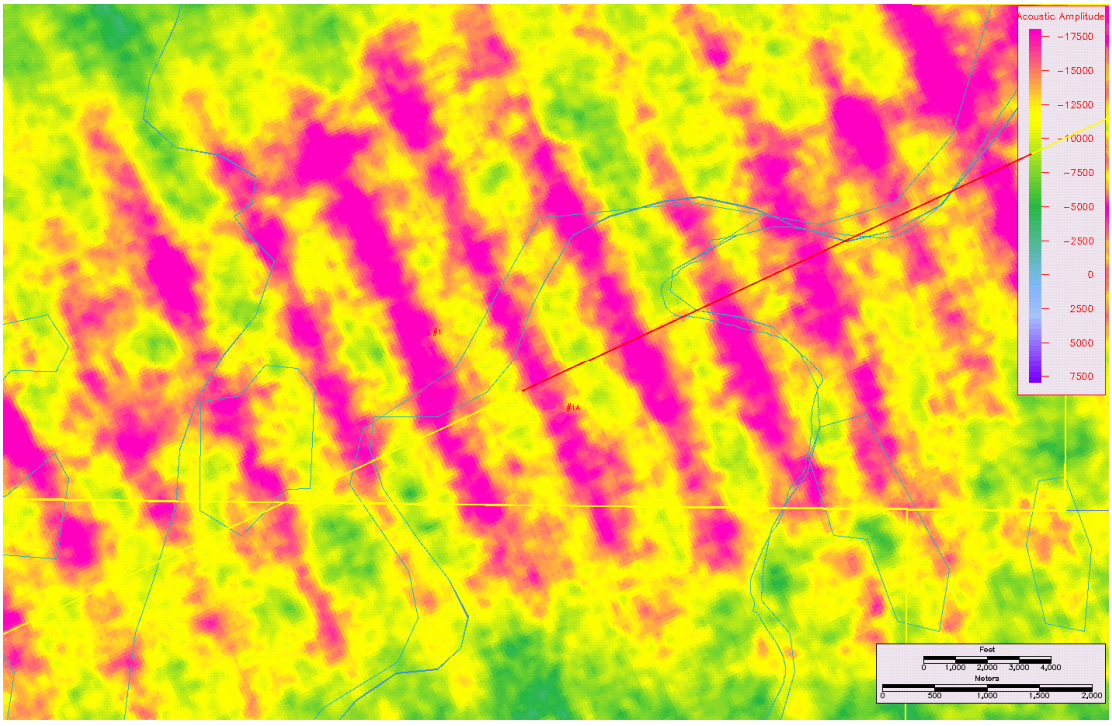


Figure 1.1: Example of acquisition footprint consisting of periodic amplitude variations on a horizon slice from a 3D volume (courtesy Talisman Energy Inc.).

1.2.1 Possible causes

Many factors are listed as causes for acquisition footprint. The reason the exact cause of footprint artefacts is not clear is because footprint is often present in some areas of a survey and not as much in others, and it varies with depth or time in the processed image, though it is sometimes observed more often in the shallow part of the section. The most likely explanation for footprint is that it is caused by an interaction between different factors. According to Cordsen et al. (2000), the factors most correlated with the enhancement of footprint are irregularities in fold, offset, and azimuth distributions. Noise in the seismic data is also a key factor, including backscattered modes as discussed by Larner et al. (1983). Though called acquisition footprint, it is known that footprint can also be processing algorithm dependent, and as a result, different processing-related effects have been identified as possible causes for footprint. The most important effect is the interaction between the processing algorithm (prestack migration in particular) and irregularly sampled or spatially aliased seismic data (e.g. Gardner and Canning, 1994; Zhang et al., 2003; Margrave, 2005; Abma et al., 2007). These studies suggest that a key factor in acquisition footprint is inadequate spatial sampling of the seismic wavefield, including signal and coherent noise, resulting in spatial aliasing. When proper sampling is not used, the irregularities associated with the survey geometry can result in footprint. Proper or adequate sampling refers to using source and receiver sampling intervals that obey the Nyquist criterion, allowing for complete reconstruction of the continuous wavefield from the recorded samples (Vermeer, 1990). Spatial sampling and aliasing are discussed in more detail in the next section.

1.2.2 Spatial aliasing and the exhaustive dataset

Because of the possible link between spatial aliasing and footprint, a brief discussion of aliasing of seismic data is warranted. Temporal aliasing is nearly nonexistent in seismic data recording and processing because the data are usually recorded continuously and passed through an antialias filter that rejects frequencies above the Nyquist frequency, $f_N = (2\Delta t)^{-1}$, defined by the chosen temporal sample interval, Δt. However, spatial sampling, defined by the locations of sources and receivers, is inherently discrete and it is not generally possible to record and process a continuous signal in space prior to sampling. For this reason, most seismic datasets suffer from a considerable degree of spatial aliasing. In the best situations usually only slow-moving coherent noise-trains show significant aliasing but, all too often, signal is also aliased.

Modern seismic datasets are commonly 5D volumes, requiring two spatial dimensions to specify receiver locations, two more for source locations, and the fifth dimension is time. The most common gathers in which spatial aliasing can be examined are *common-source* (i.e. all traces recorded with a single source), *common-receiver* (all traces recorded at a fixed receiver from any source), *common-offset* (all traces with a fixed source-receiver offset, either vector or scalar), and *common-midpoint* (all traces having the same source-receiver midpoint). A particular seismic event may be spatially aliased in one gather but not in another. Here the primary focus is on common-source and common-receiver gathers, for which the spatial sample intervals are the receiver spacing and the source spacing respectively. The common-source gather is the only gather that represents a single physical wavefield. Common-receiver gathers are

typically formed during data processing for reasons relating to the compositing of multiple source gathers into the final seismic image.

As defined for the purpose of this study, an exhaustive seismic dataset is one which shows no significant spatial aliasing in either common-source or common-receiver gathers. Of course, an exhaustive dataset may be aliased in other gathers. That an exhaustive dataset is even possible, given the impossibility of continuous spatial recording, is the consequence of the temporally bandlimited nature of the data and the physical phenomenon of evanescence. Many seismic datasets are temporally bandlimited because they were recorded with a bandlimited source such as vibroseis. However, even if dynamite was used, which can generate very high frequencies, temporal band limiting still occurs because of the antialias filters used in temporal sampling and described above. The high-frequency content of recorded seismic data is also reduced because of attenuation loss in the subsurface. The resulting highest signal frequency is denoted $f_{\max}$.

Surface seismic acquisition will be assumed here to occur on the plane z=0. A recorded shot gather can be directly analyzed for its temporal frequency spectrum and the spectra of the two horizontal wavenumbers. Denoting these as f, k_x, and k_y respectively, the vertical wavenumber, k_z, can be calculated from the scalar wave dispersion relation (e.g. Aki and Richards, 2002):

$$k_z = \sqrt{\frac{4\pi^2 f^2}{v^2} - k_x^2 - k_y^2} \qquad (1.1)$$

where v is the wavespeed. The surface recording can then be downward continued by application in the $\left(f, k_x, k_y\right)$ domain of the multiplicative operator

$$\hat{W} = \begin{cases} \exp\left(ik_z \Delta z\right), & \dfrac{4\pi^2 f^2}{v^2} \geq k_x^2 + k_y^2 \\ \exp\left(-\left|k_z\right| \Delta z\right), & \dfrac{4\pi^2 f^2}{v^2} < k_x^2 + k_y^2 \end{cases}, \tag{1.2}$$

(e.g. Gazdag and Sguazzero, 1984; Margrave and Ferguson, 1999), where Δz denotes the size of the downward step. The dual nature of the extrapolation operator in equation (1.2) is a mathematical statement of the phenomenon of evanescent waves. Essentially, propagating waves are restricted to the cone described by $\dfrac{4\pi^2 f^2}{v^2} \geq k_x^2 + k_y^2$ while the exterior of this cone refers to Fourier components that are exponentially damped in the z direction. Thus, it follows that, for temporally bandlimited data, all wavenumbers such that $k_x^2 + k_y^2 > \dfrac{4\pi^2 f^2}{v^2}$ will be exponentially damped and of no consequence in subsurface imaging. Thus, since the wavenumbers are also governed by the Nyquist criteria $k_{xN} = \pi/\Delta x$ and $k_{yN} = \pi/\Delta y$, if the spatial sample rates are such that $\left(2\Delta x\right)^{-1} > f_{\max} v^{-1}$ and $\left(2\Delta y\right)^{-1} > f_{\max} v^{-1}$, then there will be no significant spatial aliasing. Taking $\Delta x = \Delta y$, a square sampling lattice requires

$$\Delta x \leq \frac{v}{2 f_{\max}} \tag{1.3}$$

in order that spatial aliasing be negligible. In reality, the subsurface velocity is not constant; for inequality (1.3) to apply, the velocity in the equation must be equal to the minimum apparent velocity of the wavefront being sampled.

Generally, using the exhaustive sampling interval described by equation (1.3) to determine sampling intervals used in the field results in prohibitively expensive survey designs. The best way to produce artefact-free data without resorting to the exhaustive sampling interval is currently a topic of research. Though many different survey designs are used in practise, typical land 3D surveys (e.g. Figure 1.2) involve source and receiver sampling such that at least two of the five prestack dimensions (x_S, y_S, x_R, y_R, and t) are aliased. Along the source and receiver lines (the x_S and y_R directions in Figure 1.2) the sampling is good, but in the direction perpendicular to the source lines (the y_S direction) the source sampling is poor, and in the direction perpendicular to the receiver lines (the x_R direction) the receiver sampling is poor. Processing of the data, during which we map the five sampled dimensions (x_S, y_S, x_R, y_R, and t) to three image dimensions (x, y, and z), generally produces good images of the subsurface, suggesting that to some degree we can get away with these violations of the sampling theorem. Weighting schemes and regularization methods are likely key to this process, as is the fact that we sum over two of the five data dimensions in the course of imaging. Footprint artefacts, though, may result because processing is unable to completely overcome the problems introduced by poor sampling.

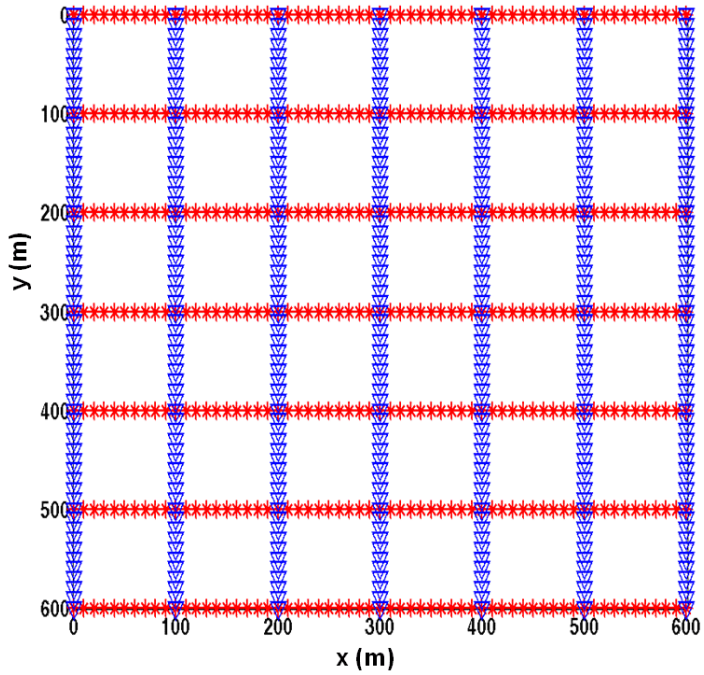


Figure 1.2: Typical orthogonal 3D survey geometry. Source positions are red stars and receiver positions are blue triangles.

Inadequacies in processing algorithms may also generate footprint artefacts. In the case of prestack migration, footprint artefacts can be a product of the migration algorithm used to create the final seismic images (Margrave, 2005). Irregularities and aliased energy in the data input to migration tend to result in noise in the migrated output. Figure 1.3 is a simple example of this effect, after Bancroft (2006), showing spatially aliased data before and after migration, as well as the corresponding f-k spectra. The aliased energy associated with the steep dips in the unmigrated data is improperly migrated. It can be shown (e.g. Vermeer, 1990; Margrave, 2005) that the wavenumber content of a stacked section comes equally from both source and receiver wavenumbers, i.e.

$$k_M = k_S + k_R, \tag{1.4}$$

where k_M is the midpoint wavenumber. This suggests that aliasing in either source or receiver sampling domains, or both, would result in aliased contributions to the final seismic image.

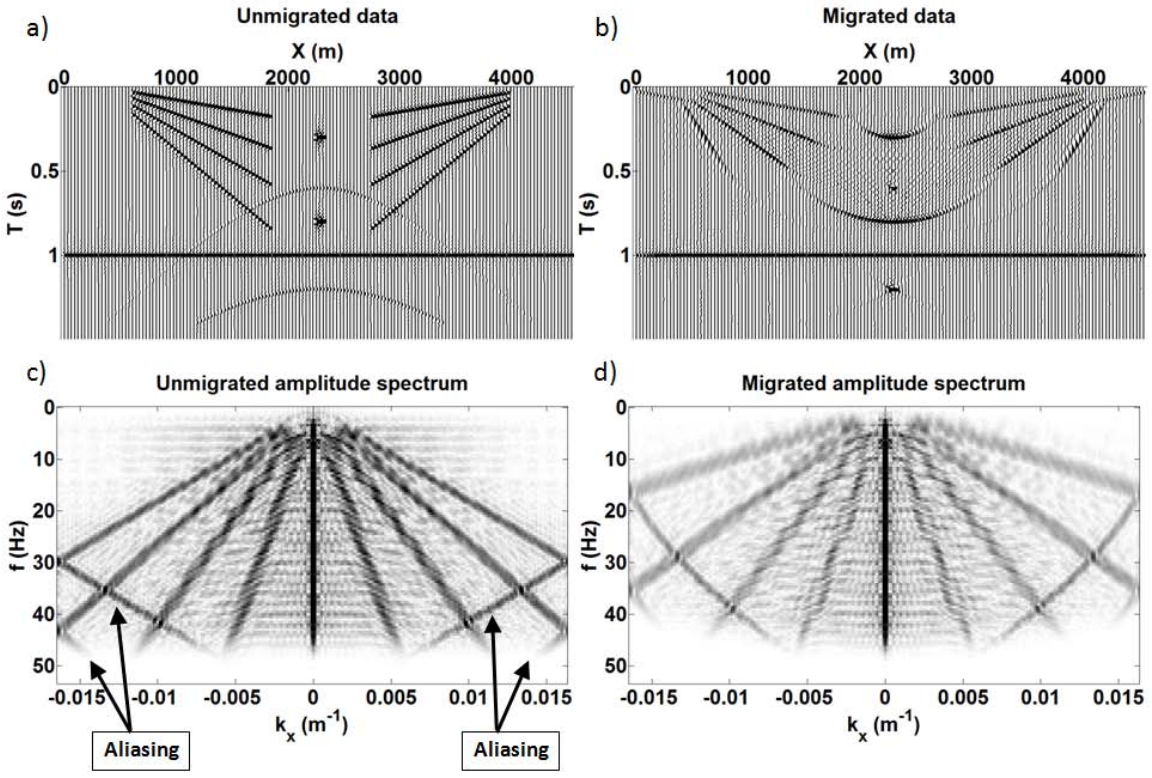


Figure 1.3: Data with spatial aliasing a) before migration, and b) after migration; corresponding f-k amplitude spectra c) before migration, and d) after migration, after Bancroft (2006).

1.2.3 Strategies for footprint removal or prevention

Taking the perspective that footprint is a type of unwanted noise in seismic data means that removal of footprint in seismic processing could be attempted by filtering. However, as is the case with filtering other types of noise, it is difficult to achieve significant footprint reduction while still ensuring that true amplitude anomalies are not

affected. Filtering can be attempted in many different domains. Treating footprint as spatially periodic noise leads to removal attempts in wavenumber space, for example kx-ky filtering of time slices (e.g. Drummond et al., 2000), or f-kx-ky filtering (e.g. Gülünay et al., 1994; Gülünay, 1999). Other methods include tau-p-q filtering (e.g. Marfurt et al., 1998) and methods based on singular-value decomposition (e.g. Trickett, 2003). This last method is mostly applied to random noise removal, but can also be adapted to the case of footprint removal (e.g. Al-Bannagi et al., 2005).

Though footprint removal is possible with the above methods to a certain degree, prevention of footprint artefacts is preferred. Since footprint is an interaction between the acquisition geometry and the processing flow applied to the data, prevention of footprint has two sides: survey design and processing algorithm design. Many different acquisition geometries, for example Vermeer's (1998) symmetric sampling, have been proposed as optimal for reducing footprint because of their ability to sample the continuous wavefield in a more acceptable way. Even random sampling (e.g. Wisecup, 1998) has been suggested as way to produce less footprint than regular but sparse geometries. Especially in the case of 3D surveys, there is almost no end to the variety of possible survey designs; however, the most common philosophy is that a good design is one in which the fold, offset, and azimuth distributions in each common-midpoint bin are as uniform as possible. Cordsen et al. (2000) and Cooper (2004a,b) provide a thorough overview of 3D survey design considerations. Though certain designs are more commonly used than others, for example the orthogonal design in land 3D surveys, this is partly due to the historical development of 3D surveys as an extension of 2D surveys and limitations imposed by the nature of the equipment used. For example, most designs

involve straight lines of receivers and shots. Cost is also a major factor in survey design, so even if an optimal geometry can be proposed using theoretical reasons, it is not necessarily economically feasible to be used in the field. As a result, no single survey design has emerged as the answer to preventing acquisition footprint.

On the processing side, a major focus for footprint prevention is on regularization methods that change the non-ideal acquired geometry into a more regular, more ideal geometry. These methods are most applicable to the case of prestack migration since the stacking process already performs regularization in the case of creating stacked sections or poststack migrations. Partial stacking is one such approach (e.g. Cary, 1999a), though the disadvantages of this approach are the same as the reasons for using prestack migration instead of poststack migration, including possible poor imaging of steeply dipping reflectors. Another approach is to use data mapping techniques to transform the offsets and azimuths of the recorded traces to other desired values (e.g. Canning and Gardner, 1996; Chiu and Stolt, 2002). A different method is to interpolate traces between existing traces to produce a more regular geometry (e.g. Manin and Spitz, 1995; Trad, 2009), though this approach can increase the data volume significantly. Instead of regularization, another focus for footprint prevention in processing is to improve the ability of the algorithms to handle poorly or irregularly sampled data, and reduce their preference for regularized input data. This approach usually results in producing particular weighting schemes, especially in prestack migration, such as those based on computing an area associated with each common midpoint, and assigning a weight based on the inverse of that area (e.g. Canning and Gardner, 1998; Jousset et al., 1999, 2000; Lee et al., 2005). Alternatively, methods can be based on prestack migration of particular

data subsets, for example offset-vector tiles (e.g. Vermeer, 2001) or common-offset vector gathers (e.g. Cary, 1999b), or other so-called minimal datasets (e.g. Gesbert, 2002), the idea being that these gathers are well-sampled and can be individually migrated without producing significant artefacts.

1.3 Objectives and scope of project

In this study, seismic acquisition footprint was examined using a numerical forward modelling approach. The modelling approach was chosen to create a controlled experiment to reduce the number of unknown variables and complexities; for example, in the numerical model the subsurface geology is known and noise can be excluded. This situation is less realistic than a study focusing on field data, but it simplifies an otherwise very complicated problem, and may increase the chances that the study will yield a useful result. The goal of the modelling was to simulate footprint artefacts observed in field data. By doing so, the purpose of the project was to increase understanding of the causes of acquisition footprint as well as to attempt to develop strategies for reducing its effect.

As discussed above, spatial sampling of the seismic wavefield may have a central role in acquisition footprint; therefore, the strategy employed in this study to investigate footprint was to compare seismic images produced with ideal or “exhaustive” spatial sampling to those produced with more typical source and receiver geometries. Exhaustive sampling involves very dense source and receiver lattices with source and receiver intervals small enough to adequately sample all seismic events without aliasing, while typical geometries generally involve sparser and more irregular source and receiver sampling. By selectively removing traces from the exhaustive dataset, sparsely sampled

datasets were formed that mimic more realistic field acquisition geometries. Processing of both the exhaustive and decimated datasets with various algorithms allowed for the examination of the effect of spatial sampling on footprint, and also allowed for observations of how algorithmic differences influence the footprint artefacts. These observations could then contribute to understanding how the processing methods interact with poorly sampled data, and potentially leading to improvements in the processing algorithms.

To produce the numerical model data, Kirchhoff modelling was used for 2D simulations, while a Rayleigh-Sommerfeld method was used in 3D. Both modelling algorithms were implemented in MATLAB. The interactions between the survey geometry and different imaging algorithms were examined by comparing results produced using "conventional" seismic processing (normal moveout correction, stack, and poststack migration) with those obtained using prestack migration algorithms. A particular prestack migration algorithm was then developed as a technique for suppression of footprint artefacts. With the exception of two industry migration algorithms, the processing was performed using code developed in MATLAB. This study was limited to examining footprint produced by inadequate sampling of reflections using coarse shot and receiver spacings; other important causes of acquisition footprint, including the effects of noise, variations in source and receiver coupling, variations in source signature, etc., were not considered here. Also, a single geological model was used and only zero-offset reflection coefficients were considered, so, although the reflection coefficient along the reflecting interface could vary with lateral position, it did not vary with angle of incidence. The range of acquisition geometries investigated

consisted solely of regularly-spaced sources and receivers positioned on a flat ground surface, spanning the entire length of the model, so no surveys involving a moving live patch of receivers were simulated. The study did not consist of an in-depth comparison of different survey designs; rather the focus was on comparing the exhaustive design to a typical decimated design. The study was also limited to using a single migration method, namely Kirchhoff migration, although different Kirchhoff algorithms were compared. Other techniques for the prevention or removal of footprint were not examined, such as interpolation or other regularization methods and filtering or other post-processing methods.

1.4 Organisation of thesis

In the first chapter of this thesis, the problem of seismic acquisition footprint has been described, including some possible factors contributing to the artefacts and several possible approaches for either preventing or reducing footprint. The concept of spatial sampling and aliasing was discussed as an issue relevant to the problem. The thesis project was described as a numerical modelling study, designed to produce simulated seismic data from a densely sampled “exhaustive” survey. The exhaustive survey and subsets of the exhaustive survey termed “decimated” surveys would then be processed to observe the resulting footprint. Variations in footprint after different processing methods would also be compared.

In Chapter 2, the methods used for numerical modelling are discussed. In 2D a Kirchhoff modelling algorithm was used, while in 3D a Rayleigh-Sommerfeld algorithm was used. The theory behind the two methods is discussed and compared, and the

reasons for using these methods are given. Then, the geological models used for the study are described, and the seismic data produced from the models are shown.

In Chapter 3, the methods used to process the modelled seismic data are described. The methods include conventional approaches involving common-midpoint stacking and poststack migration, as well as several different prestack migration algorithms. The results of processing the exhaustive and decimated datasets are displayed, and observations of the footprint produced with the different methods are made.

In Chapter 4, a new weighting scheme for Kirchhoff prestack migration called delta weighting is described. The method was developed during this study with the purpose of suppressing footprint. The results of processing the modelled data with this method are displayed and compared to the other methods used in Chapter 3.

Chapter Two: Modelling methods

2.1 Introduction

Forward modelling techniques can be used to simulate the results of a seismic survey acquired over a given geological model. Though scaled physical experiments can be performed to produce model data, numerical simulations are currently the most common modelling method. These simulations involve computer algorithms that predict the seismic response based on our knowledge of rock properties and the physics of wavefield propagation. Because of this, accurate predictions using these methods are limited to phenomena that are well understood, and many of them involve simplifying assumptions such as isotropy (Ebrom and McDonald, 1994).

A conceptually simple method is raytrace modelling. If the scale of geological heterogeneities is large compared to the seismic wavelength, plane waves and rays can be used to describe the seismic wavefield. Raytrace modelling uses a given velocity model to predict the path of rays emanating from the source and to determine where reflections will be recorded at the surface. At each subsurface interface, the rays obey Snell's law of refraction and reflection. The reflection from a given interface produces a seismic trace for each source-receiver pair that is, in most cases, the result of one ray, which interacts with the reflecting interface at a single point, the Snell's law reflection point. However, complicated geological structures produce other events besides specular reflections, such as scattered and diffracted arrivals, which are not predicted by simple ray tracing (Shearer, 1999). These events can be simulated by methods such as Kirchhoff modelling that considers subsurface interfaces to be composed of many secondary sources or scatterpoints. Each scatterpoint produces a diffraction, and the total seismic response is

the result of the constructive and destructive interference of these diffractions (Bancroft, 2006).

Other modelling methods use the wave equation more directly to propagate the seismic wavefield through the input geological model. This can be performed either in the space-time domain using a finite-difference approach, or in the Fourier domain (e.g. Gazdag, 1981). Very frequently, finite-difference algorithms are the tool of choice, because the finite-difference method can produce a very realistic response and the underlying earth model can be as highly variable as the real world. However, the method has significant problems, foremost among these being the high computational cost and the presence of significant grid dispersion. These two drawbacks usually compound each other since the way to reduce grid dispersion is either to reduce the time-step, or to increase the order of the spatial differences, or both; these strategies all increase computational cost. Consequently, 3D finite difference modelling is often so severely limited by the required computational burden that the resulting temporal frequency bandwidth is restricted to much less than comparable real datasets. This is especially true if an entire seismic survey, consisting possibly of hundreds or thousands of source records, is to be simulated.

In this study, the goal of the modelling exercise was the creation of 2D and 3D exhaustive synthetic seismic datasets. As detailed in Chapter 1, the term “exhaustive” refers to a dataset sampled sufficiently in both source and receiver positions that neither common-source gathers nor common-receiver gathers have any significant spatial aliasing. This is important because the primary purpose of the study was to examine acquisition footprint, and in particular the link between footprint and spatially aliased

data. Kirchhoff modelling was used in 2D; in 3D, the Kirchhoff method was found to be too computationally intensive, and as a result, a Rayleigh-Sommerfeld modelling method was used. The Rayleigh-Sommerfeld method is simply phase-shift migration in reverse, although it will be demonstrated to be linked theoretically to Kirchhoff modelling.

2.2 Modelling exhaustive datasets

As described in Chapter 1, an exhaustive dataset must have spatial sample intervals that conform to the inequality

$$\Delta x \leq \frac{v_{\min}}{2 f_{\max}} \tag{2.1}$$

in all four of its spatial dimensions, where Δx is the sample interval, $v_{\min}$ is the lowest apparent wavespeed, and $f_{\max}$ is the highest signal frequency. Clearly, for given values of $v_{\min}$ and $f_{\max}$, there are many sample intervals that can satisfy inequality (2.1); in this study when we refer to the exhaustive dataset, we mean the dataset with the fewest number of traces that still satisfies the inequality. Numerically modelling an exhaustive dataset, as desired in this project in order to examine the interaction between footprint and spatial aliasing, introduces some challenges to any modelling method. Assume that a 3D model is to be constructed where the source and receiver lattices are identical and consist of a square grid with spacing Δx and having area L^2, where L is the dimension of the square, or aperture. Then the exhaustive survey will require $\left(L / \Delta x\right)^2$ receivers and the same number of sources. Thus the number of seismic traces in such a model is

$$n_{tr} = \left(\frac{L}{\Delta x} \right)^4 \tag{2.2}$$

or, adopting the equality in relation (2.1) gives

$$n_{tr} = \left(\frac{2 f_{\max} L}{v_{\min}} \right)^4 . \tag{2.3}$$

The fourth power here means that the number of traces required for an exhaustive dataset can easily become too large to consider. Table 1 shows the number of traces required for an exhaustive dataset (in millions) as a function of a variety of apertures and sample sizes.

Table 2.1: The number of traces required for an exhaustive survey of size L^2 having square spatial sample size of Δx. Trace numbers are given in millions.

$\Delta x \downarrow \quad L \rightarrow$	2000	1000	500	250	125
40	6.25	0.39	0.024	0.0015	10^{-4}
20	100	6.25	0.39	0.024	0.0015
10	1600	100	6.25	0.39	0.024
5	2560	1600	100	6.25	0.39
2.5	409600	2560	1600	100	6.25

In a real setting, an exhaustive dataset of any significant aperture is nearly always impossible. This is because seismic velocities are generally very slow for shallow layers and equation (2.3) has velocity in the denominator. If waves in the slowest shallowest layers are to be sampled without aliasing, then as shown in Figure 2.1, the number of traces required, for even a modest survey, is in the billions. Since usually the slowest waves are some form of coherent “noise”, a real dataset usually has aliased noise even if the reflection signals from target zones are not aliased. This same limitation applies to

synthetic datasets produced with finite-differencing or similar techniques since these methods generally generate all possible waves. The modelling techniques used in this study, described in the next two sections, were chosen because they involve generating only primary reflections from designated reflectors and so are more appropriate for use in constructing exhaustive datasets.

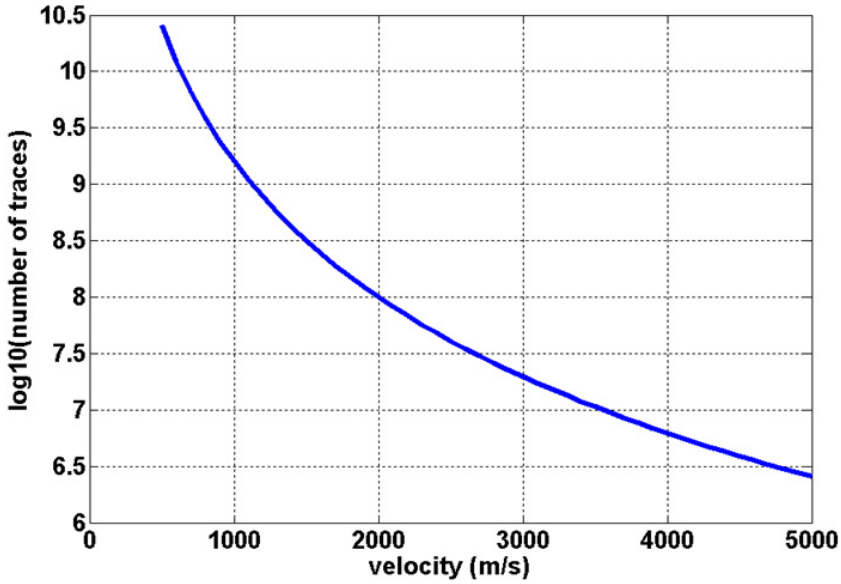


Figure 2.1: The logarithm of the number of traces required to form an exhaustive 3D dataset is shown versus velocity. Assumed here are a maximum frequency of 100Hz and an aperture of 1km.

2.3 Kirchhoff modelling

Kirchhoff theory considers that the seismic response recorded at the surface is not from one reflection point defined by a single raypath, but from scattered contributions from all points on the reflecting interface. It is based on Huygens' Principle which states that, in response to an incident wavefield, each small piece of the reflector acts as

secondary source; the interference of the waves emitted by the secondary sources produces the wavefield recorded at a later time (Liner, 2004).

Kirchhoff theory was developed in the context of optics, describing diffraction of light through small apertures. Diffraction theory explains the behaviour of waves that cannot be explained by geometrical optics (ray tracing). Generally, the theory is valid when the wavelength of the waves is small compared to the size of the aperture (Jackson, 1999). In geophysical applications, such as seismology or electromagnetics, the Kirchhoff method uses the approximation that the reflection from each point on the subsurface interface is the same as the reflection that would be produced from an infinite plane tangent to the surface at that point. Thus, the plane-wave reflection coefficient can be used to describe the wavefield immediately after encountering the reflecting interface (Shearer, 1999). This tangent-plane approximation is valid when the seismic wavelength is small compared to the scale of heterogeneity on the reflector (Beckmann and Spizzichino, 1963). The recorded wavefield at the surface is given by the reflected wavefield modified by scaling factors related to geometrical spreading and the obliquity of scattering.

The presentation of Kirchhoff diffraction theory here follows Ersoy (2007); the full derivation is not given. Figure 2.2 shows the basic geometry for the derivation of the Kirchhoff diffraction formula for the case of scalar waves that impact from the left on a perfectly opaque screen with a perfectly transparent hole and then subsequently are observed at a point P, which is taken to be on a plane to the right of the screen. The screen is assumed to be of infinite extent and the medium excluding the screen is taken to be homogeneous. Two basic results from mathematical physics, Green's theorem and the

Sommerfeld radiation condition, are then invoked. The former is simply a generalization of the fundamental theorem of calculus from 1D to 3D, while the latter describes the physical constraint that we may have only outgoing energy at infinity. Green's theorem relates the integral of a second-order differentiated scalar field over a volume to the integral of the normal derivative of that field over the surface bounding the volume. This is directly analogous to the fundamental theorem of calculus in 1D which relates the integral of a function over a line segment to the evaluation of the anti-derivative of that function at the end points of the line segment.

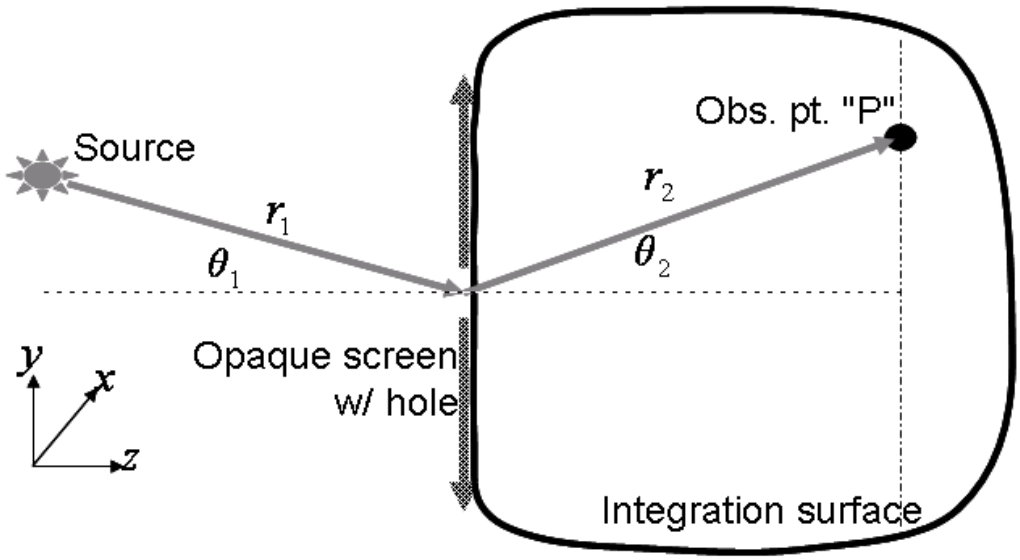


Figure 2.2: The geometry relevant to the derivation of the Kirchhoff diffraction formula for the classic case of an opaque screen with a hole, after Ersoy (2007).

In Figure 2.2, the volume of integration is formed by taking a finite, circular portion of the right-hand-side of the screen, centered over the hole and a corresponding hemisphere to the right and then letting the radius of the circle/hemisphere recede to

infinity. We denote the surface of this infinite volume by Σ. The scalar field of concern, ψ, is assumed to satisfy the homogenous media Helmholtz equation for a point source placed at the source location. The result is that the field at the observation point, $\psi(\underline{x}=\underline{P})$ ($\underline{x}$ is a general position vector while $\underline{P}$ is the specific vector pointing to the observation point), is given by

$$\psi(\underline{x}=\underline{P})=\frac{1}{4\pi}\int_{\Sigma}\left[G\frac{\partial\psi}{\partial n}-\psi\frac{\partial G}{\partial n}\right]d\underline{s} \tag{2.4}$$

where *G* is the Green's function for a source placed at the observation point, $\underline{s}\in\Sigma$, and the differentiation is taken in the direction of the outward normal to Σ. Then the Sommerfeld radiation condition may be invoked to show that the contribution to the integral in equation (2.4) from the infinite hemisphere vanishes, leaving only the integral over the screen, *S*, which is

$$\psi(\underline{x}=\underline{P})=\frac{1}{4\pi}\int_{S}\frac{e^{ikr_2}}{r_2}\left[\frac{\partial\psi}{\partial n}-ik\cos(\theta_2)\psi\right]d\underline{s} \tag{2.5}$$

where $G=\exp(ikr_2)/r_2$ has been used and $k=2\pi f/v$, with f being frequency and v being wavespeed. Figure 2.2 shows the definition of r_2 and θ_2. Also in equation (2.5), only the far-field term has been kept when evaluating the normal derivative of *G*. The further evaluation of equation (2.5) requires knowledge of the field ψ and its normal derivative at all points on the right hand side of the screen. Here Kirchhoff made the approximation that the field and normal derivative on the opaque portion of the screen are both zero while in the aperture of the hole, denoted *A*, the field and normal derivative are precisely what would be expected from a point source if there were no screen at all.

Under this approximation, and again invoking a far-field approximation in the normal derivative, the usual Kirchhoff expression is

$$\psi(\underline{x}=\underline{P})=\frac{ik}{4\pi}\int_S \frac{e^{ik(r_1+r_2)}}{r_1 r_2}\left[\cos(\theta_1)-\cos(\theta_2)\right]\rho(\underline{s})\,d\underline{s} \tag{2.6}$$

where we have defined

$$\rho(\underline{s})=\begin{cases}1, & \underline{s}\in A\\ 0, & \underline{s}\notin A\end{cases}. \tag{2.7}$$

Figure 2.2 shows the geometry defining r_1 and θ_1. The reason for defining the function $\rho(\underline{s})$ rather than simply restricting the domain of integration to the aperture, *A*, is to facilitate the generalization of equation (2.6) to the reflection seismic case. To this end, we simply fold Figure 2.2 at the screen, which becomes the reflector, to identify the source plane with the recording plane, and we allow $\rho(\underline{s})$ to generalize to the reflection coefficient of the "reflector". Thus our reflection seismic Kirchhoff formula is

$$\psi(\underline{x}_r,\underline{x}_s)=\frac{ik}{4\pi}\int_S \frac{e^{ik(r_1+r_2)}}{r_1 r_2}\left[\cos(\theta_1)-\cos(\theta_2)\right]\rho(\underline{s},\theta_1)\,d\underline{s} \tag{2.8}$$

where r_1 is the distance from the source (at $\underline{x}_s$) to a point on the reflector, r_2 is the distance from the receiver (at $\underline{x}_r$) to a point on the reflector, θ_1 is the angle of the raypath from the source at the reflector, θ_2 is the angle of the raypath from the reflector to the receiver, and $\rho(\underline{s},\theta_1)$ is no longer given by equation (2.7), but is instead allowed to take any value in the interval $[-1,1]$, equal to the value of the reflection coefficient for the incidence angle θ_1. The integration in equation (2.8) must be conducted over the entire reflection surface for each source-receiver pair. Considering the case of a fixed source

position into an exhaustive set of receivers, we let the number of points in the 2D source-receiver plane be *N*, and assume that the reflector is also gridded with *N* points. Thus the cost of the integral itself is $O(N)$ but it must be computed *N* times so that the cost of a source gather is $O(N^2)$. As a result, this leads to enormous compute times for even small 3D models.

2.4 Rayleigh-Sommerfeld modelling

Modelling based on the Rayleigh-Sommerfeld diffraction theory is very nearly as accurate as that of Kirchhoff, but as will be shown, it is $O(N \log N)$ and as a result is much less computationally intensive than Kirchhoff. It turns out that the technique is just the familiar phase-shift migration run backwards. The derivation of the Rayleigh-Sommerfeld diffraction integral, again after Ersoy (2007), follows a similar pattern with the major difference being that the Green's function used is not just that for a point source at the observation location, rather, *G* is taken as the difference between the Green's functions for a source at the observation point and for a mirror image source at the corresponding point on the other side of the screen. The result is that the $\partial\psi / \partial n$ term in equation (2.4) is cancelled and, after some calculation, we obtain

$$\psi(\underline{x} = \underline{P}) = \frac{1}{4\pi} \int_S \psi \frac{\partial}{\partial z} \left(\frac{e^{ikr_2}}{r_2} \right) d\underline{s} \qquad (2.9)$$

where the z direction is orthogonal to the screen. The integration in equation (2.9) is actually a convolution over the screen, a fact which can be appreciated by noting that

$$r_2 = \sqrt{\left(x_s - x_p\right)^2 + \left(y_s - y_p\right)^2 + \left(z_s - z_p\right)^2} \tag{2.10}$$

where the observation point coordinates are $\left(x_p, y_p, z_p\right)$ and the screen coordinates are $\left(x_s, y_s, z_s\right)$. Then, with $\psi = \psi\left(x_s, y_s, z_s\right)$ and $d\underline{s} = dx_s dy_s$, equation (2.9) becomes recognizable as a convolution of the wavefield on the screen with the function

$$W\left(x, y, z\right) = \frac{\partial}{\partial z}\left(\frac{e^{ikr_2}}{r_2}\right) = \int_S e^{iz\sqrt{k^2 - k_x^2 - k_z^2}} e^{i\left(k_x x + k_y y\right)} dk_x dk_y \,. \tag{2.11}$$

That is, the wavefield is convolved with the function *W* which is the *z* derivative of the Green's function. The last form given for *W* is not at all obvious but is well-known from imaging theory (e.g. Robinson and Silvia, 1981), and identifies *W* as the extrapolator for scalar waves, to within a constant scale factor. If the Kirchhoff approximation (see discussion preceding equation (2.6)) is now made for the field on the screen, then we can write equation (2.9) as

$$\psi\left(\underline{x} = \underline{P}\right) = \frac{1}{4\pi}\int_S \psi_o\left(x_s, y_s, z_s\right) W\left(x_p - x_s, y_p - y_s, z_p - z_s\right) \rho\left(\underline{s} = \left(x_s, y_s\right)\right) d\underline{s} \tag{2.12}$$

where ψ_0 is the field from a point source evaluated on the screen and $\rho\left(\underline{s}\right)$ is given by equation (2.7). As was done previously, we generalize to the seismic reflection case by simply interpreting $\rho\left(\underline{s}\right)$ as the reflectivity function on the reflector and identifying the source and image planes with each other. Since equation (2.12) is a convolution, we can express it in the Fourier domain as

$$\psi\left(\underline{x}_r, \underline{x}_s\right) = \frac{1}{4\pi}\int_S \widehat{W}\left(k_x, k_y, z_p - z_s\right) \widehat{\psi_o \rho}\left(k_x, k_y, z_s\right) e^{ik_x x + ik_y y} dk_x dk_y \tag{2.13}$$

where the "hats" indicate 2D Fourier transforms over *x* and *y*. Now it is apparent that the Rayleigh-Sommerfeld diffraction theory is just modelling by running the familiar Gazdag

(1978) phase-shift migration backwards. Equation (2.13) states that the field of the source is evaluated at the reflector, ψ_0, and then multiplied by the reflectivity function, ρ. This product is then Fourier transformed, multiplied by the phase-shift operator $\widehat{W}$, and inverse Fourier transformed. Furthermore, since ψ_0 can be computed as the source response extrapolated to the reflector, we have the algorithm

$$\psi(\underline{x}_r, \underline{x}_s) = \mathbf{F}^{-1}\widehat{W}\mathbf{F}\rho\mathbf{F}^{-1}\widehat{W}\mathbf{F}\psi_{source} \tag{2.14}$$

where $\mathbf{F}$ is the 2D Fourier transform. Thus the algorithm is: (1) phase shift the source wavefield to the reflector, (2) multiply by the reflectivity function, (3) phase shift the result of (2) back to the surface. This is illustrated in Figure 2.3 and Figure 2.4. In contrast to equation (2.6), which must be evaluated independently at a cost of $O(N)$ for each of *N* receivers for a cost of $O(N^2)$, equation (2.14) gives a result for all receivers simultaneously. Since this is accomplished entirely with Fourier transforms, the computational effort is $O(N \log N)$.

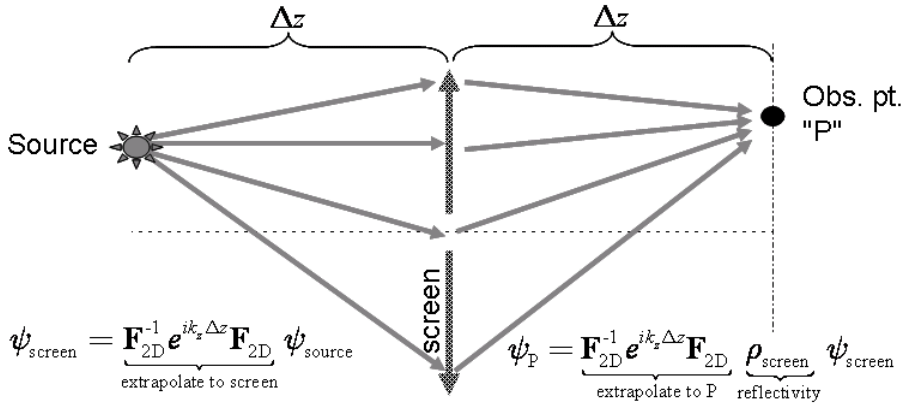


Figure 2.3: Rayleigh-Sommerfeld modelling is depicted as described by equation (2.14). The source wavefield is extrapolated by phase shift to the screen. At the screen it is multiplied by the function ρ describing the "transmissivity" of the screen, and then it is phase-shifted to the observation plane.

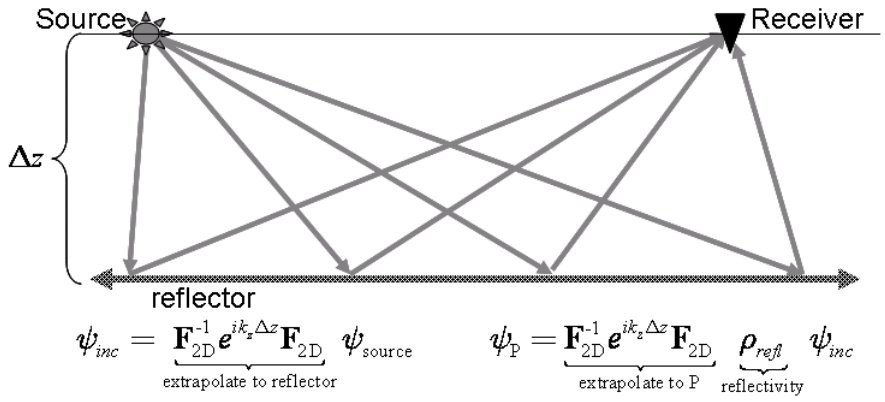


Figure 2.4: Rayleigh-Sommerfeld modelling applied to the seismic reflection case. Here the screen of Figure 2.3 becomes the reflector and the screen transmissivity becomes the reflectivity. Also the source and observation planes become identical.

Although the Kirchhoff and Rayleigh-Sommerfeld theories are called "diffraction theories" they actually compute the entire scattering response of the reflector and so include the specular component as well. While the Rayleigh-Sommerfeld approach is much faster than the Kirchhoff one, the latter adapts easily to circumstances such as a non-horizontal reflector while the former does not. Also, as developed here, both theories do not include the variation of reflection coefficient with incidence angle. This is somewhat easier to accommodate with Kirchhoff theory since ray tracing must be done anyway to obtain the incidence angles. In the Rayleigh-Sommerfeld case, it would still be possible to include this effect by separately ray tracing to compute the incidence angles.

Both theories can be extended in the same approximate way to a multi-reflector setting. For this case, the first-order Born approximation can be adopted, which means (i) the reflectivity and the background velocity model are considered to be decoupled (independent); (ii) the background velocity model is taken to be smooth and describes

wave propagation; (iii) the reflectivity is only non-zero on reflecting surfaces; and (iv) only primary reflections are generated. With these considerations, the Rayleigh-Sommerfeld response of a multi-reflector model is

$$\psi(\underline{x}_r, \underline{x}_s) = \sum_{k=1}^{N_{reflectors}} \mathbf{F}^{-1}\widehat{W}_k\mathbf{F}\rho_k\mathbf{F}^{-1}\widehat{W}_k\mathbf{F}\psi_{source} \qquad (2.15)$$

where ρ_k is the reflectivity, and $\widehat{W}_k$ is the WKBJ phase shift extrapolator appropriate for the kth reflector given the background velocity mode. While transmission coefficients are not explicitly included here they can be made a part of $\widehat{W}_k$.

2.5 2D model

The 2D Kirchhoff modelling algorithm was implemented in MATLAB following the description given by Shearer (1999). The MATLAB function, ***kirkshot2D***, produces a synthetic shot record with the seismic response from a single reflector using the input velocity-depth profile of the overburden, spatial positions of the source and receivers, and reflection coefficient of the reflector as a function of lateral position. As described in section 2.3, the seismic trace recorded at each receiver in the shot record is calculated as a summation of diffractions produced by all points on the reflector; the amplitude of each contribution is scaled by factors related to geometrical spreading and raypath obliquity. The modelling technique includes effects such as scattering, diffraction, and rays that do not obey Snell's law of reflection.

The function takes as input the spatial positions of the source and receivers, a vector defining the reflection coefficient at the reflecting interface, and the velocity-depth profile of the overburden. For the source position given, the function performs a loop

over receivers. For each receiver, the simulated seismic trace is calculated by a summation over the reflector, as described by a discrete version the Kirchhoff integral from equation (2.8). The ***kirkshot2D*** function performs the summation as a loop over the vector of lateral positions along the reflector. This summation is performed in the time domain, by adding together the traces that would be recorded coming from each contributing point along the reflector. However, the calculation of the amplitude and arrival time of each contribution is computed in the frequency domain. The contribution is scaled by the reflection coefficient for that position on the reflector, by the geometrical spreading factors for the paths from source-to-reflector and from reflector-to-receiver, and by the cosines of the incidence and scattering angles. The arrival time for the contribution from each point on the reflector is calculated by ray tracing from the reflector to each source and receiver. The inverse Fourier transform then returns the result to the time domain, where it is summed into the trace recorded at the receiver. Once the traces for all receivers have been modelled, the shot record is output as a matrix, where each column corresponds to a receiver position. The equation implemented in the ***kirkshot2D*** code is found by first multiplying equation (2.8) by the Fourier spectrum of the source wavelet used in the modelling, $\hat{w}$, and then taking the inverse Fourier transform to find the time domain equivalent of the wavefield in equation (2.8). The order of integration is switched so that the integration over the reflecting surface is performed after the inverse Fourier transform. Finally, the surface integral is approximated by a sum, producing the expression

$$\phi(\underline{x}_r, \underline{x}_s) = \sum_S \left(F^{-1}\left(\frac{i\omega\, \hat{w}}{4\pi v} \frac{e^{i\omega(t_s+t_r)}}{g_S g_r} \left[\cos(\theta_s) - \cos(\theta_r) \right] \right) \rho\, \Delta A \right), \tag{2.16}$$

where $\phi(\underline{x}_r, \underline{x}_s)$ is the expression of $\psi(\underline{x}_r, \underline{x}_s)$ in the time domain, and ρ is a function of position on the reflector representing the reflectivity. The subscripts on the angles have been modified to reflect their connection to the source and receiver raypaths; similarly, the spreading factors have been generalized from simple raypath lengths to the arbitrary factors g_s and g_r to allow for more complicated spreading in non-constant velocity media. The expression $k = 2\pi f / v$ has been used to convert the distances in the exponential to traveltimes t_s and t_r. The surface summation is performed with area elements of size ΔA.

In 2D, the derivation would involve the use of a 2D Green's function, which can be expressed asymptotically, and to within a constant scale factor, as $e^{(ikr+i\pi/4)}/\sqrt{kr}$ (Bleistein et al., 2001). Using this concept, the equivalent form of equation (2.16) in 2D is suggested to be

$$\phi(\underline{x}_r, \underline{x}_s) = \sum_S \left(F^{-1}\left(\frac{\sqrt{i\omega}\, \hat{w}}{4\pi v} \frac{e^{i\omega(t_s+t_r)}}{\sqrt{g_S}\sqrt{g_r}} \left[\cos(\theta_s) - \cos(\theta_r) \right] \right) \rho\, \Delta A \right). \tag{2.17}$$

The square roots of the spreading factors and the factor of $\sqrt{i\omega}$ (representing the half-derivative in time) make the difference between equations (2.17) and (2.16) similar to the difference between implementations of Kirchhoff migration in 2D and 3D.

The source wavelet used in the modelling was defined in the frequency domain, using the ***filtspec*** function, which is part of the Consortium for Research in Elastic Wave Exploration Seismology (CREWES) toolbox in MATLAB. Using ***filtspec***, a wavelet can be defined by choosing a sample rate, a frequency range over which the spectrum is flat, and the width of Gaussian tapers at the edges of the flat portion of the spectrum. The wavelet used in this project and its amplitude spectrum are shown in Figure 2.5. The wavelet sample interval was 0.002s, and the frequency band of the wavelet was 10-100Hz. The wavelet was defined to be zero phase.

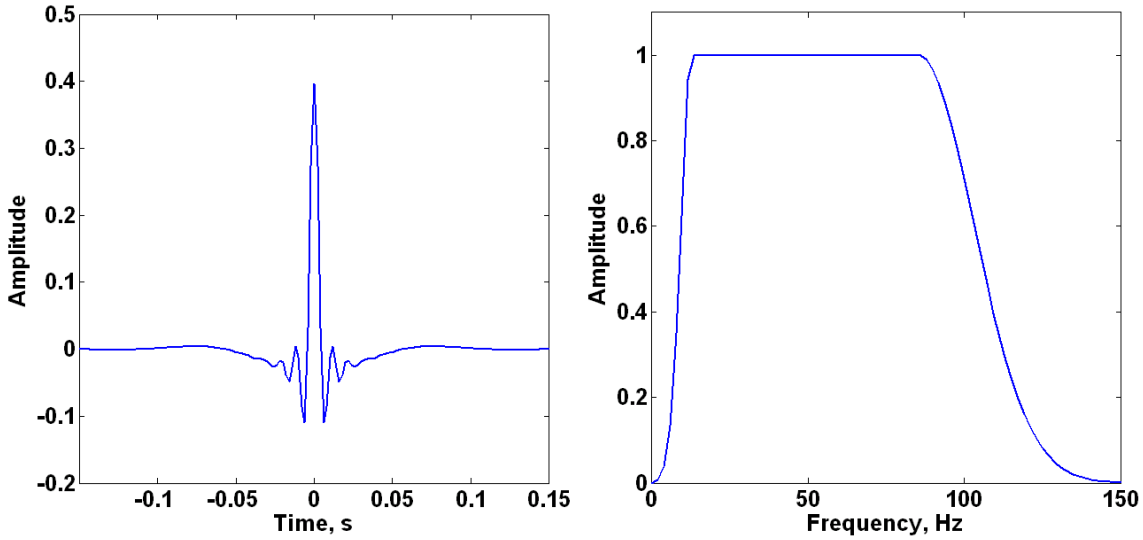


Figure 2.5: Source wavelet and wavelet amplitude spectrum.

The ***kirkshot2D*** function uses ray tracing to calculate the source-to-reflector and reflector-to-receiver traveltimes that are used in the phase-shift term. First, the critical angle at the reflector, θ_c, is calculated. Then a fan of rays is defined, spanning incidence angles between $-\theta_c$ and $+\theta_c$. The ray parameters for this ray fan are input to the ***shootray***

function, which is also part of the CREWES toolbox. ***Shootray*** performs one-way ray tracing through the v(z) medium and outputs vectors of traveltimes and horizontal distances, corresponding to each ray parameter. Given the horizontal distance between source and reflection point, and between receiver and reflection point, values for the source-to-reflector and reflector-to-receiver traveltimes are found by interpolation of the time-horizontal distance relationship output by ***shootray***. Also, the incidence and scattering angles used in the cosine scaling factors are found by interpolation of the vector of ray parameters, given the source-to-reflection point and receiver-to-reflection point offsets. The built-in MATLAB function ***interp1*** is used to perform the interpolation, using a linear method. The ray parameters are also used to calculate the geometrical spreading scaling factors for the source-to-reflector and reflector-to-receiver paths. This is accomplished using the ***sphdiv*** function in the CREWES toolbox, which uses the approach described by Krebes (2005, Equation 7-11).

The value of the reflection coefficient used to define the amplitude of the contribution from each reflection point is defined by the vector input to the ***kirkshot2D*** function. The reflection coefficient can be constant along the reflector or can vary with lateral position. One value for the reflection coefficient must be specified for each reflection point. Since the distance between reflection points is half of the distance between source and receiver positions, the reflection coefficient vector must be defined at half the source/receiver sampling interval. Only regularly-spaced sources and receivers, and therefore regularly-sampled reflectors, were considered in this project. When only one value for the reflection coefficient is input to the ***kirkshot2D*** function at each reflection point, that value is used for all angles of incidence. In this particular study

changes in the reflection coefficient with angle were not incorporated; the reflection coefficient used at each reflection point was the zero-offset reflection coefficient. This choice was made primarily for simplicity and to avoid very large reflection coefficient amplitudes near the critical angle.

2.5.1 2D Geological Model

A simple 2D geological model was created for use in modelling; it is shown in Figure 2.6. The model has a width of 400m and the target reflector is at a depth of 190m, producing an approximate survey aperture-to-depth ratio of 2. Above the target reflector are four flat, constant velocity layers. The velocities and densities of these layers increase with depth. The near-surface layer has a velocity of 1200m/s; this low velocity, coupled with the strong step-wise velocity gradient, makes emergent raypaths near-vertical for all source-receiver offsets. The velocity of the near-surface layer also defines the fundamental spatial sampling interval necessary to prevent aliasing of reflection energy. Using the relationship defined in equation (2.1), the minimum velocity in the geological model and the maximum frequency in the source wavelet define the fundamental spatial sampling interval. Since $v_{\min}$ = 1200m/s and $f_{\max}$ = 100Hz, Δx must be less than $v_{\min}/2f_{\max}$ = 6m.

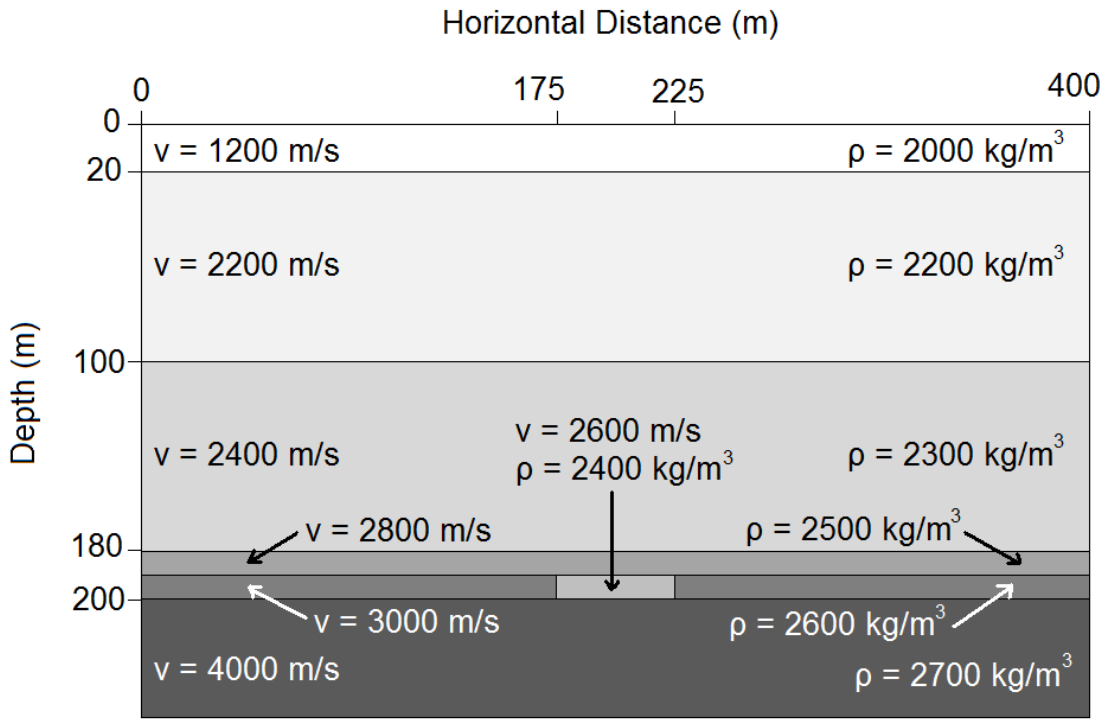


Figure 2.6: 2D geological model used throughout this study, displaying velocities and densities.

The reflector at 190m constitutes the top of the geological target zone. The target zone consists of a channel in the middle of the model with lower velocity and density compared to the laterally-adjacent rocks. Since the velocities and densities of the rock layers in the target zone vary with lateral position, the reflection coefficient at the top of the zone also varies with position. Given the velocities and densities shown in Figure 2.6, the zero-offset reflection coefficient associated with the top of the channel is -0.05, while the off-channel reflection coefficient is +0.05. The target zone sits on a half-space representing the geological basement. Only the reflection from the top of the target was modelled in this study, despite the presence of the shallower interfaces. This choice was made in order to minimize model run-times. The channel was added to the reflecting

interface by changing the value of the reflection coefficient over the region between x=175m and 225m. As shown in Figure 2.7, this produced diffractions from the edges of the channel, and a region of reflection amplitude with opposite polarity. Migration of the shot record with a prestack migration algorithm to be described in Chapter 3 collapsed the diffractions and resulted in a flat reflection with a change in amplitude corresponding to the channel location, from x=175-225m, as seen in Figure 2.8. There are migration artefacts present due to the termination of the reflections and diffractions at the edge of the modelled section.

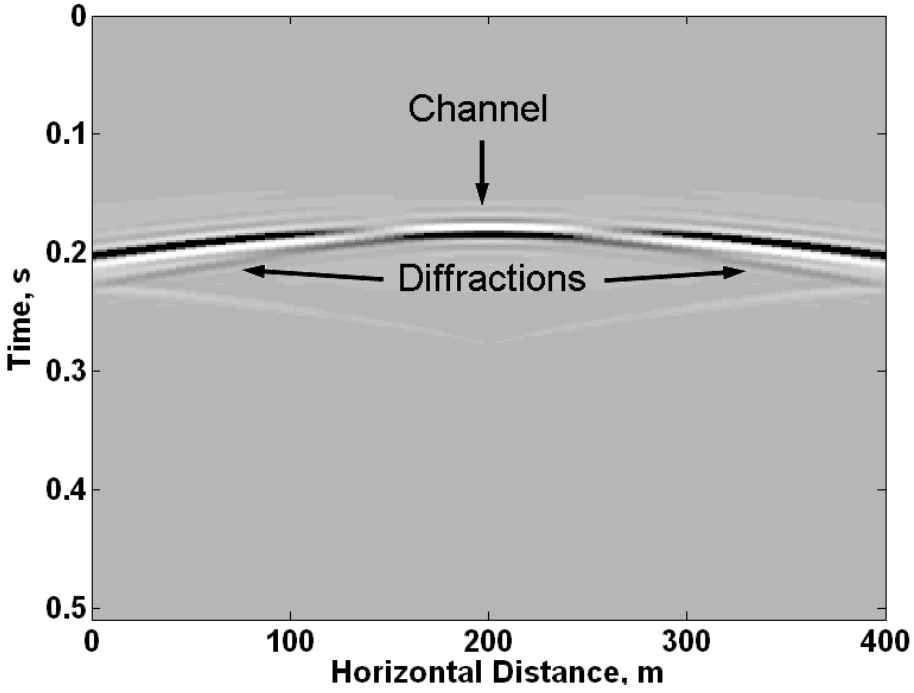


Figure 2.7: Model shot record of flat reflector with channel from x=175-225m.

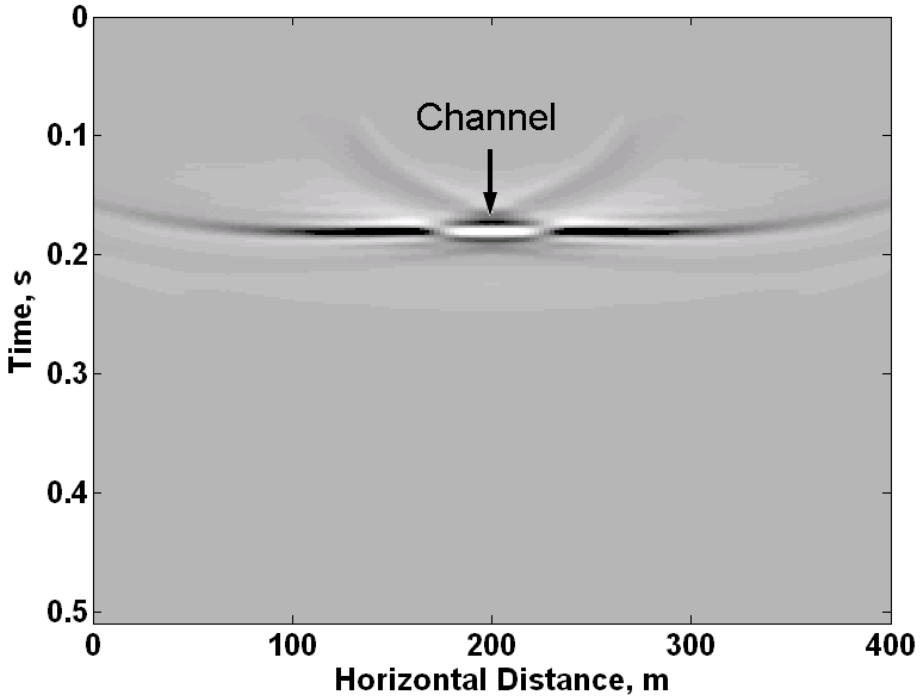


Figure 2.8: Migrated shot record from channel model. Channel is located from x=175-225m.

Based on the calculation of the appropriate spatial sampling interval required to prevent aliasing, a fundamental sample interval of 5m was chosen. As a result, the 2D exhaustive dataset corresponded to a survey geometry with sources located from x=0-400m in 5m intervals. Receivers were also located from x=0-400m at 5m intervals. Five decimated datasets were created with the purpose of examining footprint; these involved removing shots from the exhaustive dataset, to simulate shot-reduced survey geometries. The five decimated shot intervals were 10m, 25m, 50m, 100m, and 200m. The receiver positions remained the same as for the exhaustive survey. From a traditional perspective of seismic processing involving NMO correction and CMP stack, receivers on a 5m grid sample the reflector in the subsurface on a 2.5m grid. To accommodate this effect, the reflector was specified on a 2.5m grid for all of the modelling.

2.6 3D model

In 3D, the computational requirements for modelling became much larger. Kirchhoff modelling was too slow to allow for an exhaustive survey to be modelled. This prompted the use of the Rayleigh-Sommerfeld technique. After consideration of the available computing resources and the technical requirements of the study, a survey of 400m by 400m sampled at 10m was chosen. This means that there are $41^2 = 1681$ receivers and the same number of sources, and $41^4 = 2825761$ traces. Figure 2.9 shows the velocity model, which was chosen to be laterally invariant (to conform with the phase-shift formulation of Rayleigh-Sommerfeld modelling), and which was constructed to have a low velocity surface layer as is typical for land surveys. The data were modelled with an impulsive source and subsequently bandlimited with Ormsby parameters of [0 0 110 180] Hz, with Gaussian tapers on the corners, as used in the 2D modelling. This means that the primary signal band was 0->110 Hz. Three horizontal reflectors were modelled at depths of 100m, 180m, and 200m. The first two reflectors were featureless with constant reflection coefficients of -0.05 and +0.05 respectively. The third reflector contained a channel model, shown in Figure 2.10, with reflection coefficients of +0.1 outside the channel and -0.1 inside the channel. There were also 6 point scatterers embedded in the third reflector. This information is summarized in Table 2.

Table 2.2: Velocity, depth, and reflector information for the 3D model.

Depth (meters)	Velocity (m/s)	Reflector	Comment
0	1200		
20	2200		
100	2400	first	r.c.=-0.05
180	2800	second	r.c.=+0.05
190	3000		
200	3000	third	Figure 2.10
500	3000		

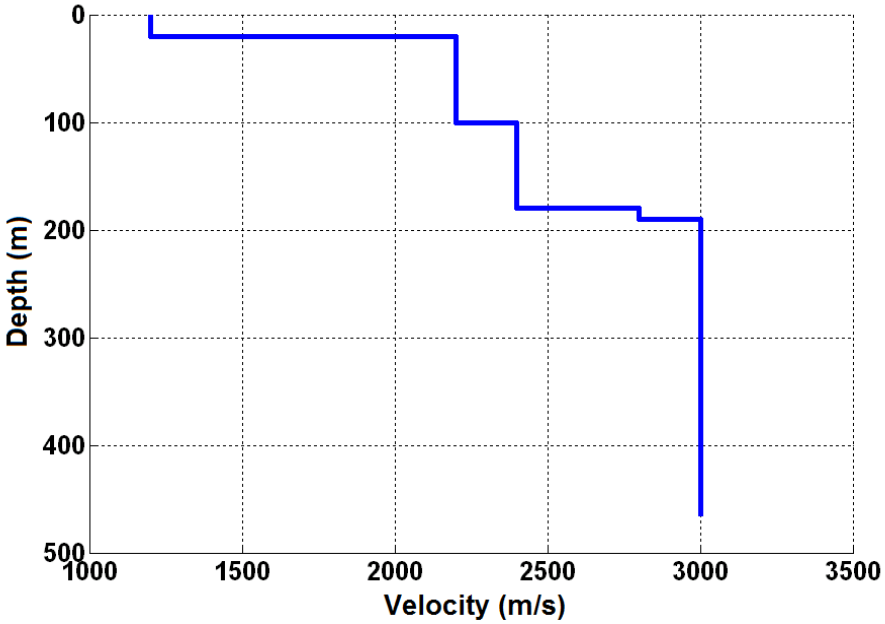


Figure 2.9: The velocity profile chosen for the 3D model.

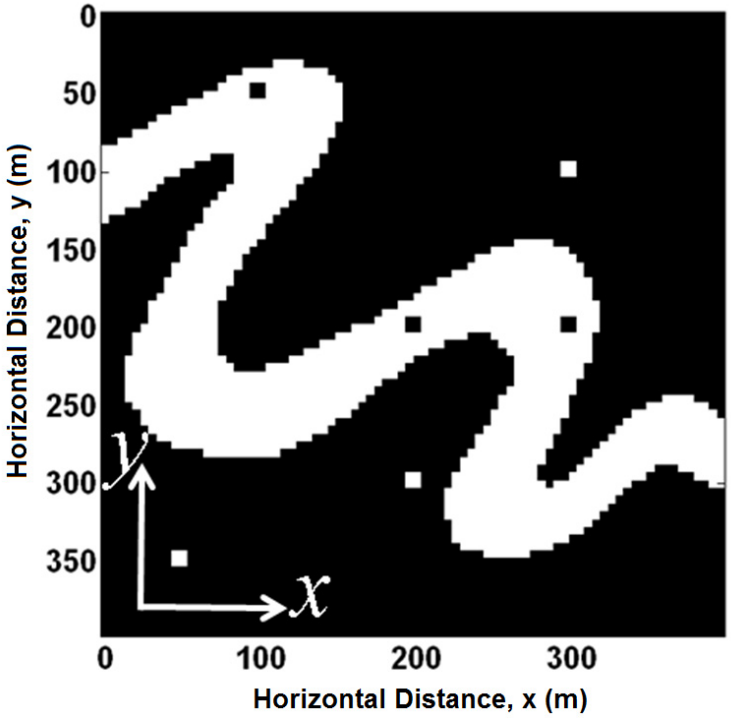


Figure 2.10: The third reflector, placed at a depth of 200m in the model. The black colour corresponds to a reflection coefficient of +0.1 whereas white is -0.1.

The spatial sampling interval of 10m was larger than that used in 2D, again in order to help reduce the computational load, while still trying to preserve the unaliased nature of the exhaustive dataset. As opposed to the simple calculation based on the lowest velocity in the model, it was chosen such that a ray with a reflection angle of 90º on the first reflector will just lie on the boundary of spatial aliasing at 110Hz. To appreciate this, it is instructive to calculate the critical frequency, that is the frequency at which spatial aliasing begins, for ray approaching 90º from each reflector assuming the 10m sample interval. Since such a ray propagates to the surface while conserving its horizontal slowness (Snell's law), a simple calculation shows that this critical frequency is given by $f_{crit} = v_+ / (2\Delta x)$, where v_+ is the velocity immediately above the reflector.

For the first, second, and third reflectors, v_+ is 2200m/s, 2400m/s, and 3000m/s and the resulting critical frequencies are 110Hz, 120Hz, and 150Hz. respectively. Thus only frequencies in the Ormsby taper will suffer any aliasing and, for the third reflector this is quite minimal, and will correspond only to very large scattering angles.

Again, as outlined in the description of the 2D modelling, the reflection point grid in the subsurface is twice as fine as the receiver grid on the surface. To accommodate this effect in 3D, the reflectors in the model were all specified on a 5m grid and the complete 3D Rayleigh-Sommerfeld response was computed on that finer grid. Thus the wavefields were actually computed on an 81x81 grid and every other trace was saved to simulate the receivers recording on a 41x41 grid.

As a first example of calculated responses, Figure 2.11 compares Rayleigh-Sommerfeld modelling and Kirchhoff modelling. Each panel is a time slice through the 3D response of a single shot. The complicated reflection response is due to the channel. The times beside each panel are representative CPU times. The $O\left(N^2\right)$ scaling for Kirchhoff is the reason for the huge change in run times when the grid spacing is halved. It seems that Kirchhoff modelling is slightly superior to Rayleigh-Sommerfeld at the same grid spacing; however, the difference in computation times is dramatic. It is obviously preferable to use Rayleigh-Sommerfeld on a fine grid whenever the limitations of the technique are acceptable. The Rayleigh-Sommerfeld technique was used in this study for all subsequent 3D modelling results.

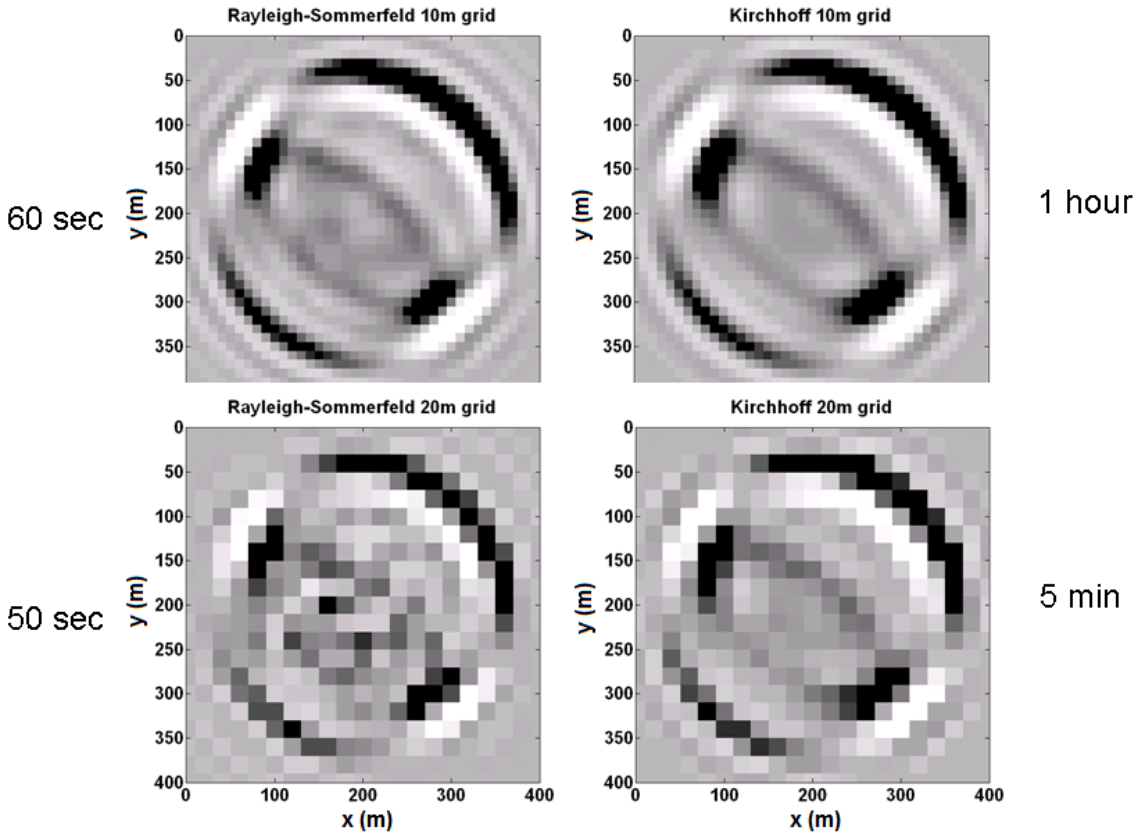


Figure 2.11: Rayleigh-Sommerfeld modelling compared to Kirchhoff at two different grid spacings. Each panel is a constant-time slice through a 3D response.

Figure 2.12 displays an entire 3D source record for a source in the geometric center of the survey (x=y=200m on Figure 2.10). The record is displayed as a 2D array in which each y-line is identifiable by the hyperbolic reflection signatures of the three reflectors. The featureless first reflector manifests as a sequence of white hyperbolae occurring at delays which are minimal in the center of the figure. The featureless second reflector is similarly structured but is at overall greater delays corresponding to its greater depth. The two reflectors also have opposite sign reflection coefficients. The third reflector is much more complicated and shows an intricate mix of reflection and diffraction effects. Figure 2.13 and Figure 2.14 show an x-line and a y-line sorted from

the data of Figure 2.12, and the two lines cross at the source location. Comparison with Figure 2.10 allows identification of channel edge diffractions, channel reflections, and off-channel reflections. In general the diffraction events are quite complicated, possibly because there are strong out-of-the-plane effects from the sinuous channel. Figure 2.15 is a time slice through the 3D source record, demonstrating a nice circular (non-dispersive) wavefront, and Figure 2.16 shows a 3D perspective view of the source record.

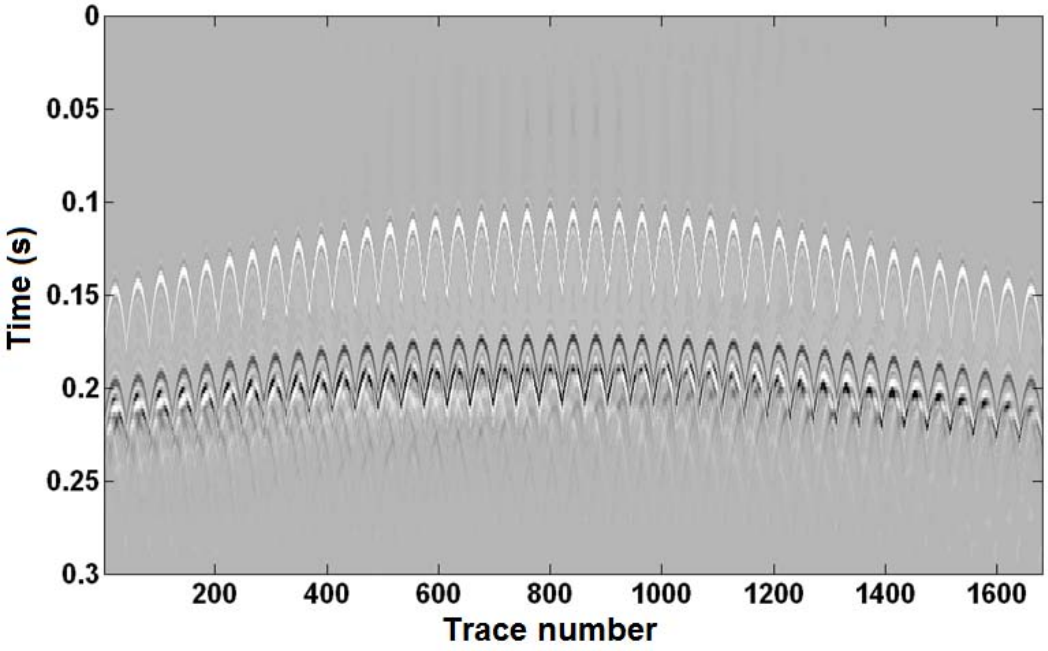


Figure 2.12: An entire 3D shot record for a source location at the center of Figure 2.10. Each small hyperbolic event is a reflection as recorded on a line y=constant. The more complicated nature of the third reflector, compared to the first two, is readily apparent.

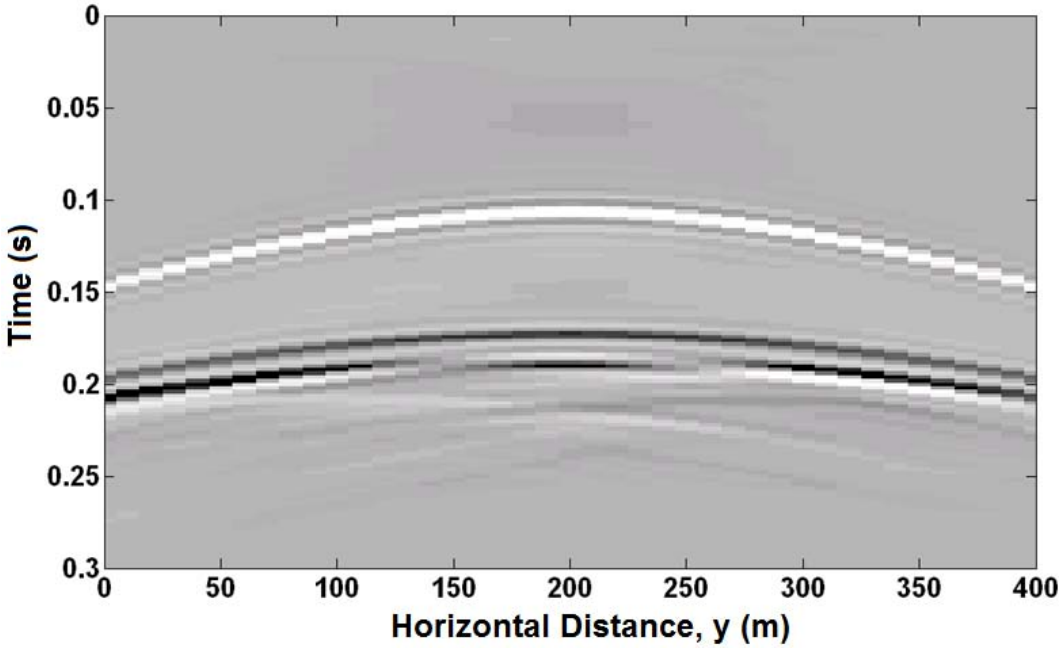


Figure 2.13: The 3D response of Figure 2.12 is shown isolated along a single 2D receiver line at x=200m.

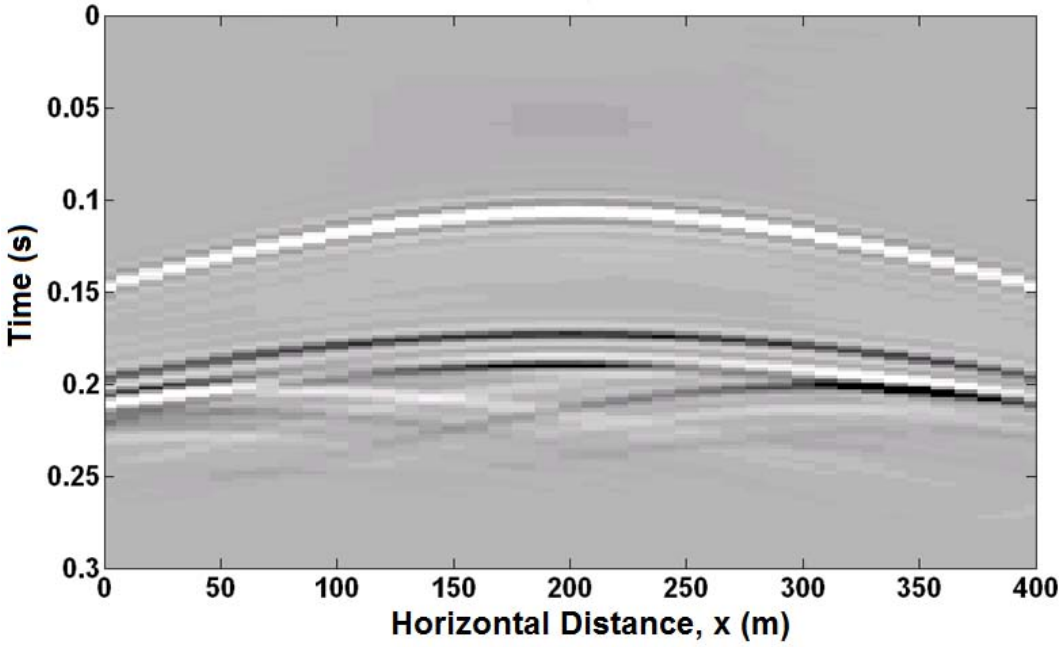


Figure 2.14: The 3D response of Figure 2.12 is shown isolated along a single 2D line at y=200m.

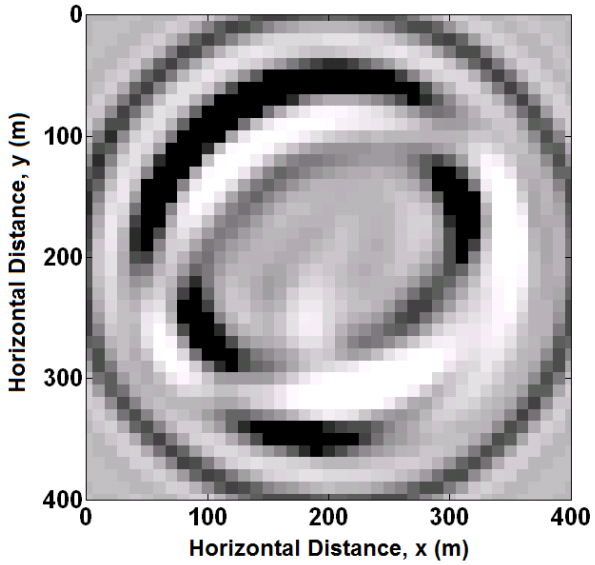


Figure 2.15: A time slice at t=0.2 seconds through the 3D source record of Figure 2.12.

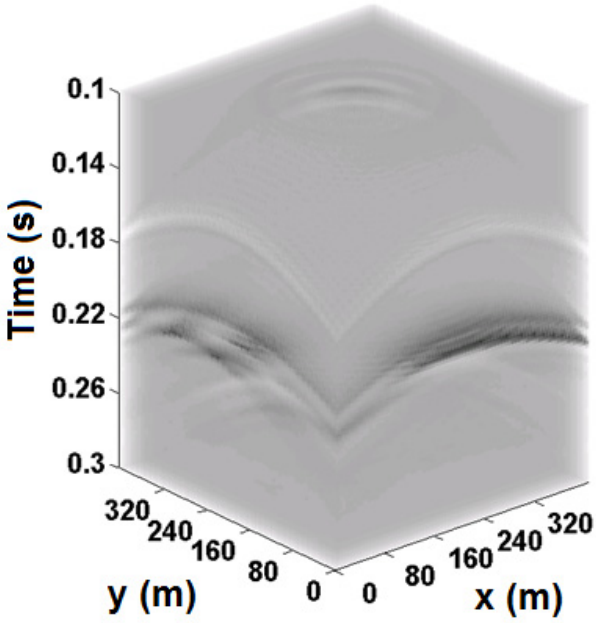


Figure 2.16: The 3D source record of Figure 2.12 is shown in a true 3D perspective.

The 3D source records were migrated with a 3D Kirchhoff algorithm, described later in Chapter 3. Figure 2.17, Figure 2.18, and Figure 2.19 show depth slices

corresponding to each of the three reflectors from the 3D migration of the source record of Figure 2.12. While the source record was sampled at 10m, these migrations are sampled at 5m. As mentioned previously, the modelling was actually done on a 5m grid and then down-sampled, without antialias filtering, to the 10m receiver grid. Thus there is every reason to expect to see 5m detail in these migrated images. The 100m reflector has produced an appropriately featureless image with significant values largely confined to the areal extent of the CMP coverage (Figure 2.17). The 180m reflector, although it is featureless, has imaged with a very significant imprint from the nearby 200m reflector (Figure 2.18). As seen in Figure 2.19, the 200m reflector has produced a very good channel image, showing significant channel detail well outside the CMP coverage box.

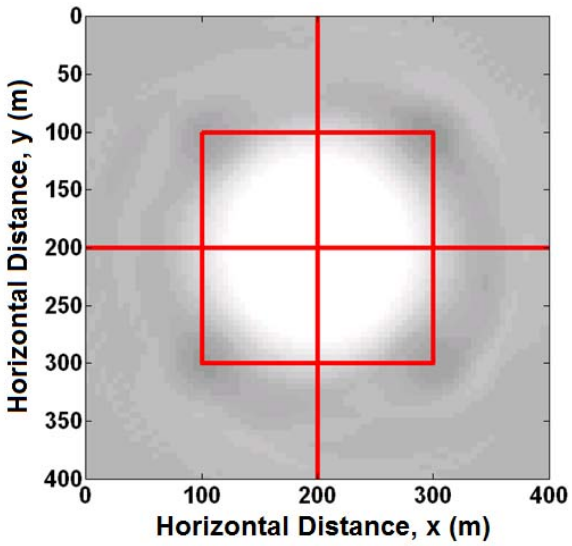


Figure 2.17: A single depth slice at 100m from a 3D migration of the data of Figure 2.12. The crossing red lines locate the source position and the red square denotes the boundary of the CMPs expected. This was modelled as a featureless reflector with a negative reflection coefficient.

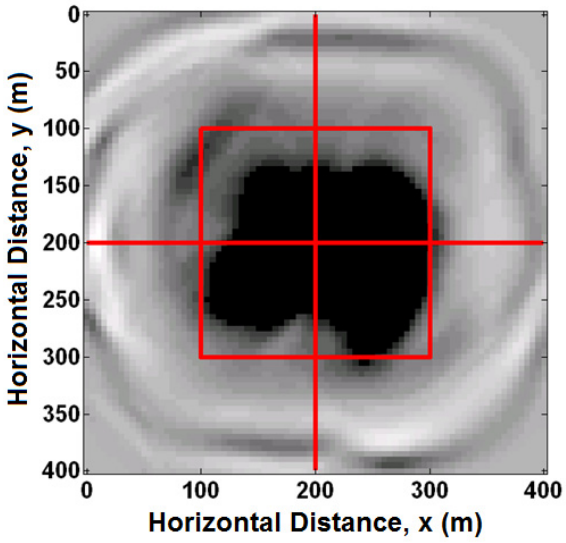


Figure 2.18: Similar to Figure 2.17 except that the depth slice is at 180m, where a featureless reflector with a positive reflection coefficient was modelled. The zero phase (non causal) wavelet has allowed the reflector at a depth of 200m (Figure 2.19) to influence this image.

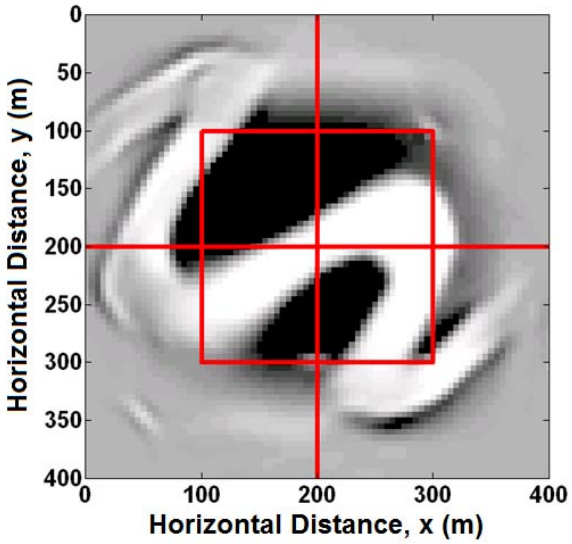


Figure 2.19: Similar to Figure 2.17 and Figure 2.18 except that the depth slice is at 200m, where the reflector of Figure 2.10 was modelled.

Figure 2.20 shows the 3D record for a source in the upper left-hand corner of the survey, that is at x=y=0m in Figure 2.10. Compared to Figure 2.12, the significantly

larger offsets and their one-sided nature are apparent. Figure 2.21 and Figure 2.22 show 2D receiver lines sorted from the 3D gather and should be compared both to the channel reflector of Figure 2.10 and to the corresponding figures for the previous source record (Figure 2.13 and Figure 2.14). Figure 2.23 is a time slice comparable to Figure 2.15. Finally depth slices from the 3D migration are shown for each reflector in Figure 2.24, Figure 2.25, and Figure 2.26. Compared to Figure 2.17, the 100m reflector has produced an image that has filled only about 50% of the CMP coverage box. The 180m reflector (Figure 2.25) has also not filled the CMP box but there is a false channel image far outside the box. The 200m reflector has more fully filled the CMP box and has, in fact, imaged well beyond it (Figure 2.26).

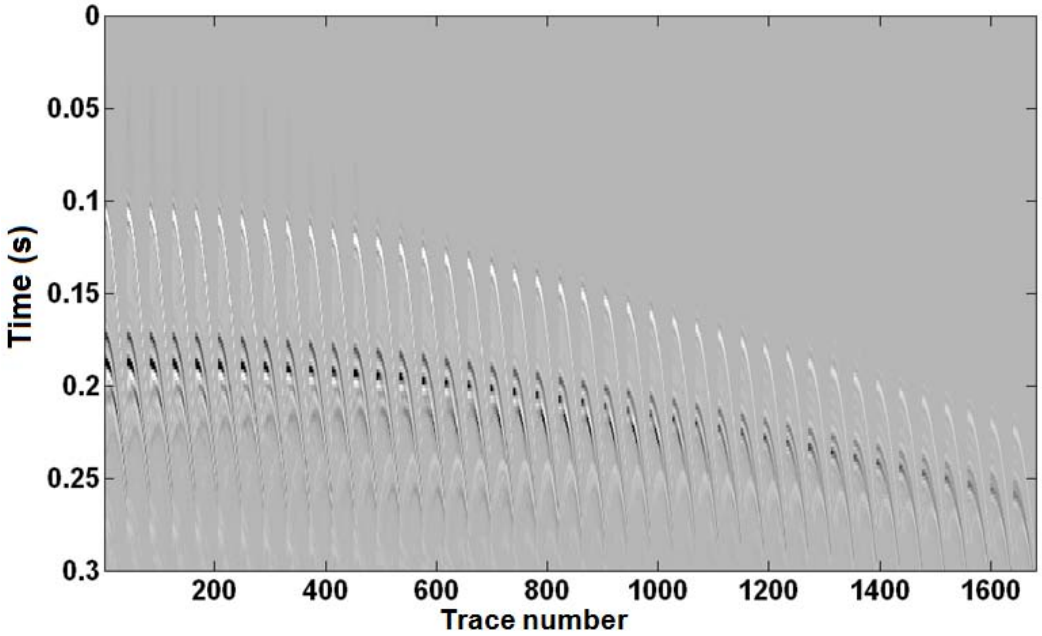


Figure 2.20: A 3D source record for a source located at x=y=0m (Figure 2.10). Compare with Figure 2.12.

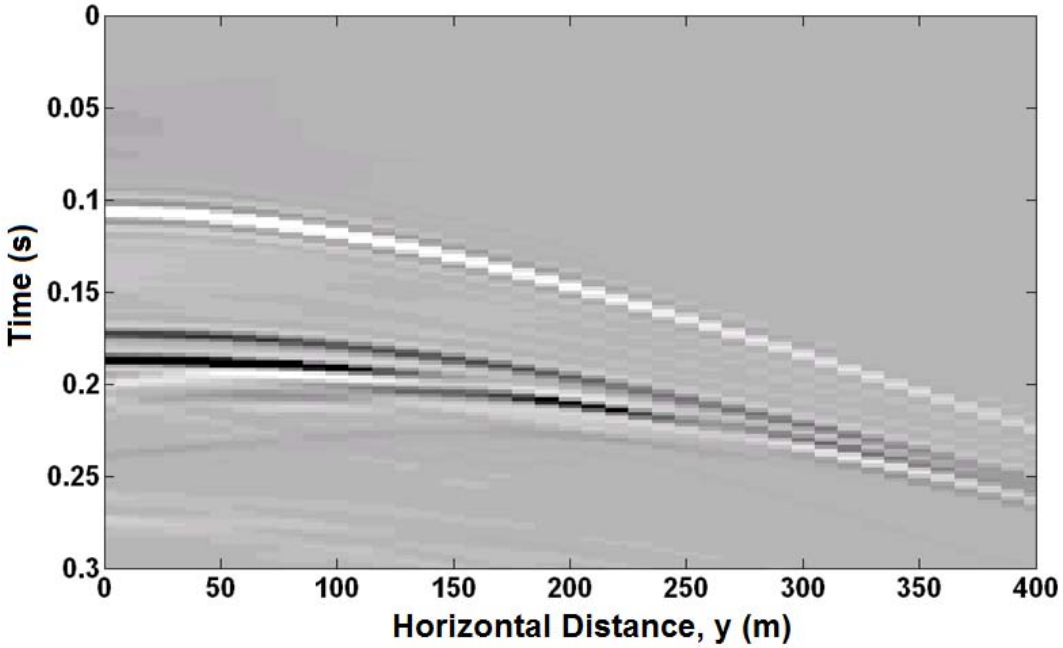


Figure 2.21: A 2D receiver line sorted from the data of Figure 2.20. The receivers were all at x=0m.

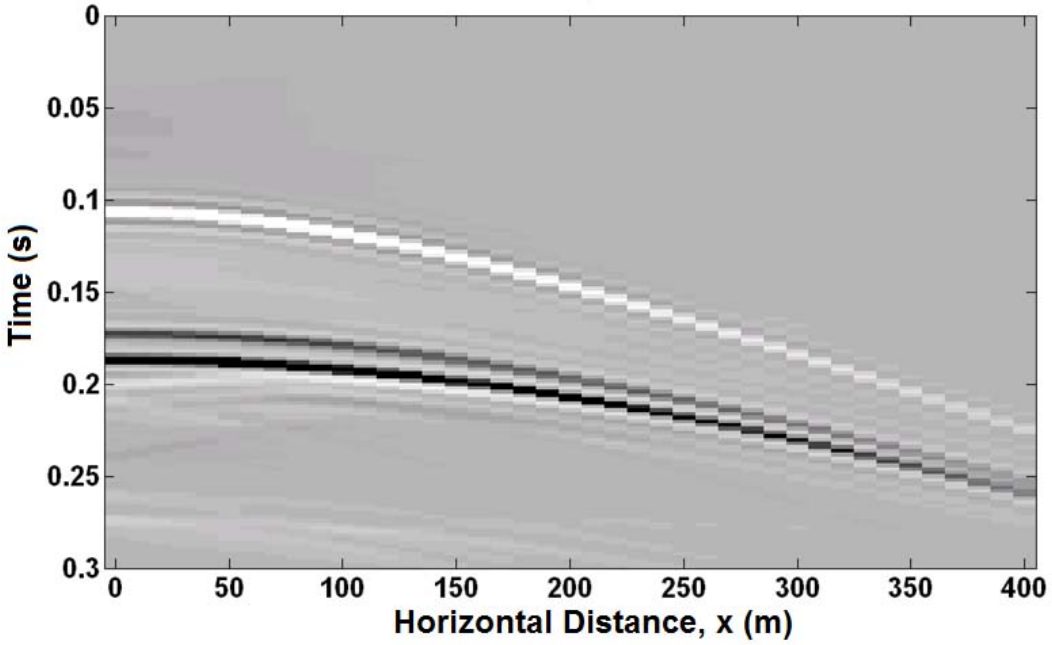


Figure 2.22: A 2D receiver line sorted from the data of Figure 2.20 for receivers at y=0m.

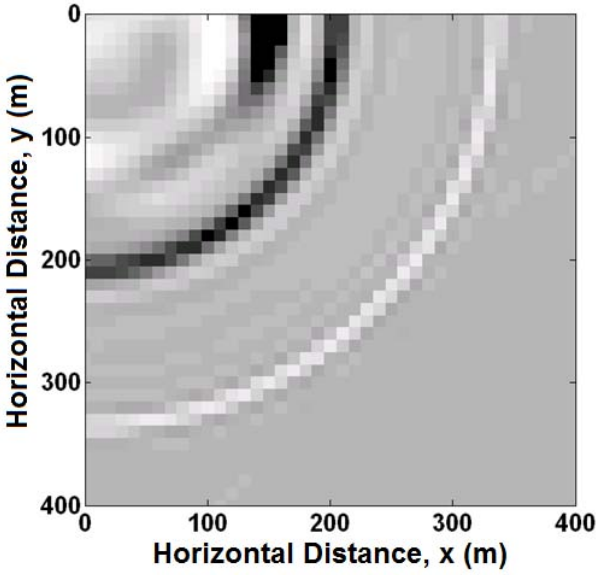


Figure 2.23: A time slice from the data of Figure 2.20, taken at t=0.2 seconds.

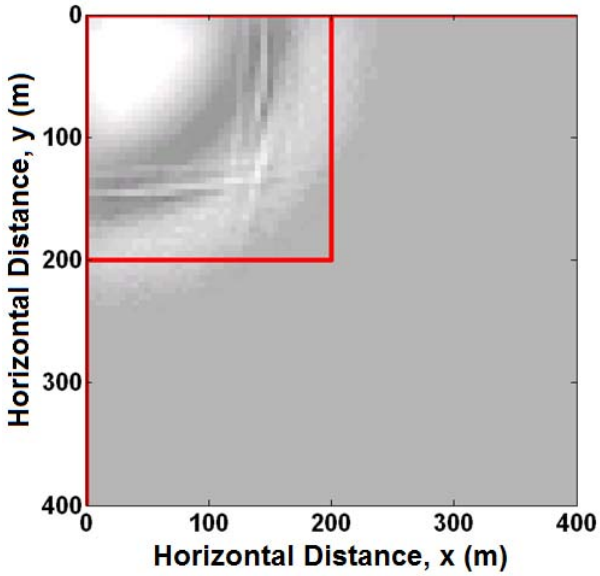


Figure 2.24: A depth slice at 100m after 3D migration of the data in Figure 2.20.

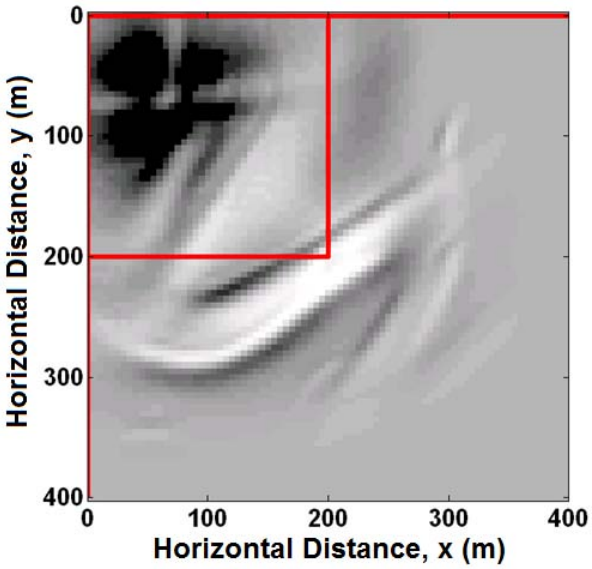


Figure 2.25: A depth slice at 180m after 3D migration of the data in Figure 2.20.

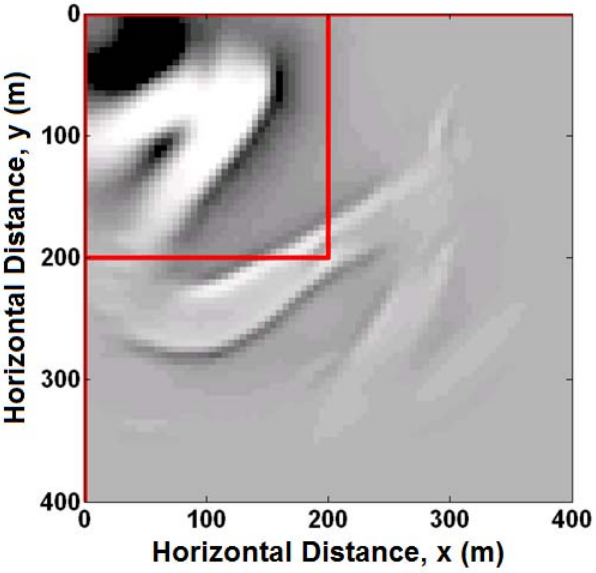


Figure 2.26: A depth slice at 200m after 3D migration of the data in Figure 2.20.

As described earlier, the exhaustive dataset was produced using shot, receiver, shot line, and receiver line spacings of 10m (Figure 2.27a). The survey involves 1681 shots, with 1681 receivers live per shot, which required three days to model. Figure

2.28a shows the f-k spectrum of a slice taken at x=240m through a shot record for a source position at (240m, 0m); the spectrum shows no aliasing, indicating that the choice of receiver interval was appropriate for the exhaustive dataset.

In order to produce datasets simulating more typical field acquisition geometries, several decimations of the exhaustive dataset were produced. One of these decimated datasets will be discussed here. As shown in Figure 2.27b, the decimated survey geometry is an orthogonal survey design typical of many land 3D surveys. The source lines run parallel to the y-axis and the receiver lines run parallel to the x-axis. The source line and receiver line spacings are 80m, though the source and receiver spacings along lines remain equal to the exhaustive sampling interval, namely 10m. This results in aliasing of shot wavenumbers in the x-direction and of receiver wavenumbers in the y-direction. Figure 2.28b shows the f-k spectrum for the x=240m slice through a shot record from the decimated survey in the same position as that shown in Figure 2.28a from the exhaustive survey. Figure 2.28b clearly illustrates the aliasing occurring in the x-direction, orthogonal to the shot line direction.

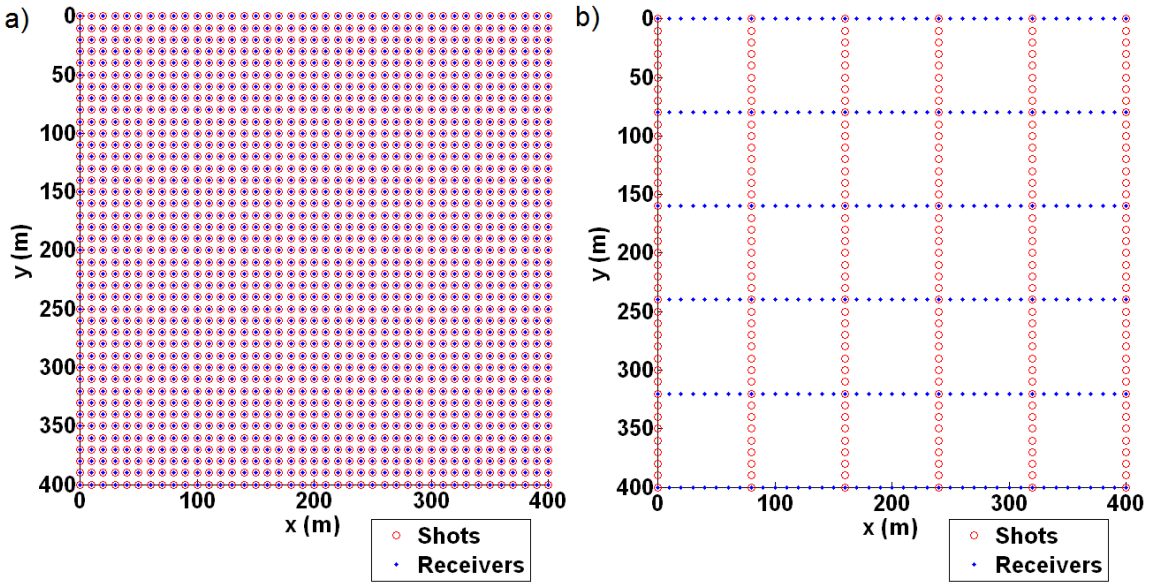


Figure 2.27: Geometry of a) the exhaustive survey and b) the decimated survey.

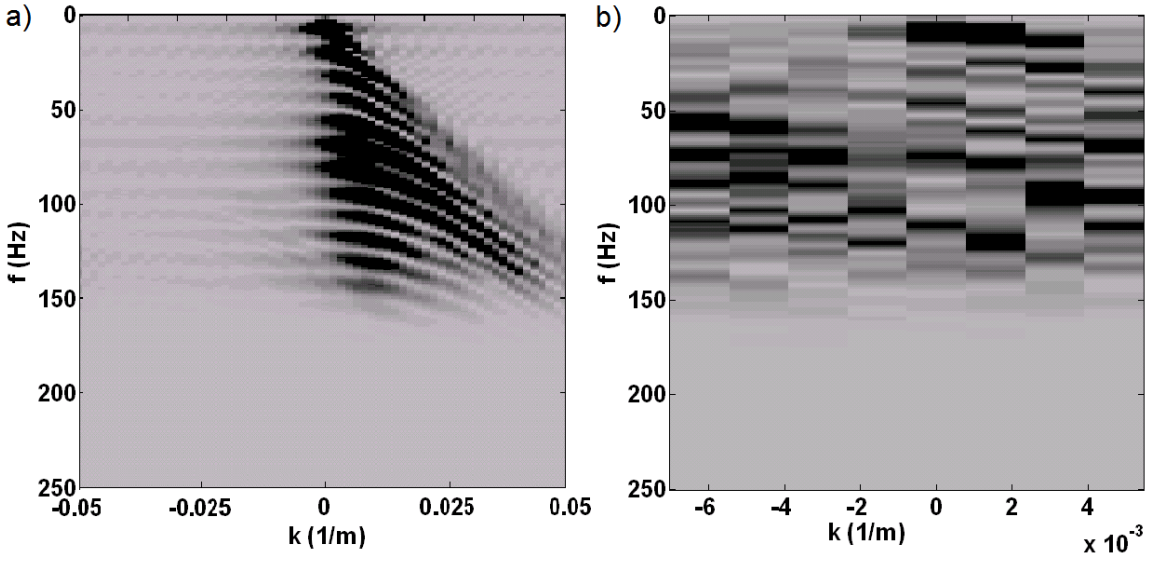


Figure 2.28: The f-k spectra for slices at x=240m through 3D shot records from a) the exhaustive dataset and b) the decimated dataset, produced by a source at (240m, 0m).

2.7 Summary

In this chapter, the two modelling methods used in this study were described. The methods, Kirchhoff modelling and Rayleigh-Sommerfeld modelling, are both based on diffraction theory. Their major difference in practice is computational efficiency of the Rayleigh-Sommerfeld method, which was exploited for the 3D modelling. The methods were used to create 2D and 3D exhaustive datasets. As described, an exhaustive dataset has no spatial aliasing in either source or receiver gathers, and as such involves dense source and receiver geometries. The production of the exhaustive datasets was performed in order to study seismic acquisition footprint, in particular the possible link between footprint and spatial aliasing. Decimated datasets were formed by sorting traces from the exhaustive dataset to simulate more realistic survey geometries. The Kirchhoff method was used in 2D to produce an exhaustive survey corresponding to a line 400m long with 5m source and receiver intervals. The geological model involved one horizontal reflector at 190m depth with a channel feature in the middle, embedded in a v(z) medium. The decimated datasets corresponded to source-reduced survey geometries, with source intervals of 10m, 25m, 50m, 100m, and 200m. The Rayleigh-Sommerfeld method was used in 3D to produce an exhaustive survey that was 400m by 400m on the surface, with 10m source and receiver intervals in both x and y directions. There were three horizontal reflectors, at 100m, 180m, and 200m depth. The upper two reflectors were featureless and the third incorporated a sinuous channel feature. The decimated geometry was an orthogonal survey design with 80m source line and receiver line intervals. The 2D and 3D exhaustive and decimated datasets were subsequently processed, and the resulting footprint was assessed, as described in Chapter 3.

Chapter Three: Processing of modelled data and observed footprint

3.1 Introduction

With 2D and 3D exhaustive and decimated datasets created via numerical modelling, the next step in the study was to process the datasets and then examine any footprint in the resulting images. Since the geological models are known exactly, the footprint artefacts could be isolated from the images. The objective was to characterize the footprint, including observations of when it occurred, how it manifested itself, and how severe it was. The processing methods used included common-midpoint stacking, poststack migration, and prestack migration. This allowed for a comparison of footprint produced using different processing algorithms. In 3D, a further comparison of different prestack migration algorithms was performed. This chapter begins with a general description of the different processing methods. The results of applying the methods to the 2D and 3D datasets are then shown.

3.2 Processing methods

The final product from the processing of seismic data is an image of the Earth's subsurface. Two main methods are used in seismic imaging; the first involves normal moveout (NMO) correction, common-midpoint (CMP) stacking, and poststack migration, while the second involves prestack migration. In the case of 2D surveys, both methods convert the 3D recorded seismic wavefield, which is a function of source location, receiver location, and time, to a 2D cross-section, which is a function of horizontal position and time (or depth). Similarly, in 3D surveys, the 5D recorded data are converted into a 3D image. Migrations are categorized as time or depth migrations; the

two classes differ in their ability to deal with laterally varying velocities. In constant velocity or flat-lying homogeneous layers, time and depth migrations are equivalent (Bancroft, 2006). There exists a great variety of migration techniques, operating in the space-time, space-frequency, and wavenumber-frequency domains. Kirchhoff migration, a space-time domain method, is one of the most commonly used migration algorithms (Gray, 1998). Other methods include f-k, finite-difference, phase-shift, and reverse-time migrations (Bancroft, 2006). In this study, only Kirchhoff time migration was used; since the models involved flat reflectors in v(z) media, time migration was appropriate. The scope of the study did not include comparisons to other migration methods. For the work described in this chapter, the focus was on comparing images produced using poststack and prestack migration, and as such did not involve attempts to fully optimize the parameters used in the migrations.

3.2.1 CMP stacking

The most conventional imaging process involves NMO correction, CMP stacking, and poststack migration. The first two steps attempt to convert the recorded data into a simulated zero-offset seismic survey, where each trace is the result of a collocated source and receiver at each point along the surface. First, traces are sorted into common-midpoint gathers, assembling all traces from source-receiver pairs with the same midpoint but different source-receiver offsets. For flat reflectors with no lateral variations in velocity, these gathers contain reflection energy coming from common reflection points in the subsurface. Then, reflection events in the CMP gather are approximately hyperbolic, with a minimum time at zero offset, obeying

$$t^2 = t_0^2 + x^2 / v_{RMS}^2 \tag{3.1}$$

where t is the recorded time at offset x, t_0 is the zero-offset traveltime, and v_{RMS} is the root-mean-square velocity (Bancroft, 2006). The difference between t and t_0 at each offset is the normal moveout (NMO). The NMO correction involves removing this time difference so that each trace in the gather mimics the zero-offset trace. Solving equation (3.1) for t and subtracting t_0 defines the magnitude of the NMO correction with offset:

$$\Delta t_{NMO} = t - t_0 = \sqrt{t_0^2 + x^2 / v_{RMS}^2} - t_0 \cong \frac{x^2}{2 v_{RMS}^2 t_0} \tag{3.2}$$

where the approximation in the final step is valid for $x << v_{RMS}\, t_0$ (Krebes, 2005). The NMO correction flattens the reflection hyperbolae in the CMP gather so that when the traces are summed together, the reflections add constructively, producing a single zero-offset trace. This summation applied to all CMP gathers is called CMP stacking, which produces a 2D seismic section (for a 2D survey) that is a function of lateral position and time. Poststack migration is then applied to this simulated zero-offset section.

3.2.2 Poststack migration

Poststack migration is based on the concept of the exploding reflector model developed by Loewenthal et al. (1976). The exploding reflector model allows the stacked section, containing traces from many simulated zero-offset experiments, to be considered as the result of one single experiment, wherein sources placed along the reflectors in the Earth simultaneously fire at time zero and a wavefield propagates to the surface at half the physical velocity (Gray, 1998). The migration process involves applying the wave equation to the wavefield recorded at the surface, $\phi(x, z = 0, t)$, to produce an image of

the reflectors at the time they exploded, $\phi(x, z, t = 0)$. In other words, migration moves the recorded energy to point in the subsurface at which it was generated. A common way of conceptualizing the process considers that energy recorded at time t by a collocated source-receiver pair could have come from any point on a surface of constant traveltime; in a constant velocity medium this surface is a semicircle (2D) or a hemisphere (3D). This makes 2D Kirchhoff poststack migration the process of spreading energy over semicircles, with the amplitude along the semicircle varying in a specific way; the constructive and destructive interference of the semicircles results in the migrated image (Bancroft, 2006). For more complicated velocity variations, the shape of the constant traveltime surface can be found by ray tracing.

Poststack migration is known to be inaccurate under certain conditions. Reflection point smearing occurs when the location of the true reflection point is not at the source-receiver midpoint, for example when there are dipping reflectors. In addition, poststack migration cannot account for lateral velocity changes, and it also breaks down under conditions where the hyperbolic moveout equation (3.2) does not apply, for example when anisotropy is present or when source-receiver offsets are large. To account for these more complex situations, prestack migration is generally used instead of stacking and poststack migration.

3.2.3 Prestack migration

Instead of applying migration after the seismic data have been stacked, prestack migration involves migrating all of the input raw traces, and then stacking the resulting images. This makes prestack migration more computationally intensive, and thus

historically less commonly used, than poststack migration. If the input data are considered one shot record at a time, migration methods based on the wave equation can be used, since a shot record consists of a single physical experiment. Instead of the exploding reflector model, prestack migration involves considering two wavefields: the incident wavefield, which results from forward propagating the source down to the reflector, and the reflected wavefield, which results from backward propagating the recorded wavefield down to the reflector. At the reflector, which is located where the two wavefields reach the same subsurface point at the same time, the ratio of the reflected field to the incident field is equal to the reflection coefficient (Gray, 1998). In this way, in a 2D survey each shot record produces a 2D image of reflection coefficients located in their true subsurface positions; the final seismic image is formed by stacking (summing) all the migrated shot records. In a geometric sense, prestack migration using the Kirchhoff method can be conceptualized by spreading energy over constant traveltime surfaces; these surfaces are now ellipses in the constant velocity case, with foci located at the source and receiver positions. Again, ray tracing can be performed to determine the shape of the surface in more complicated velocity models.

In this study, prestack migration was performed in accordance with Bleistein et al. (2001). The reader is referred to that source for the complete derivation. Bleistein et al. treat migration as an inversion problem involving an incident wavefield, produced by the shot at $\boldsymbol{x}_s$ and travelling into the earth, and a scattered wavefield, produced from the reflection of the incident wavefield as observed by the receivers at $\boldsymbol{x}_g$. In the temporal frequency domain, the scattered wavefield, u_S, in a 3D earth can be written as

$$u_S\left(\boldsymbol{x}_g,\boldsymbol{x}_s,\omega\right)=\omega^2\int_D\frac{\alpha\left(\boldsymbol{x}\right)}{c^2\left(\boldsymbol{x}\right)}u_I\left(\boldsymbol{x},\boldsymbol{x}_s,\omega\right)g\left(\boldsymbol{x}_g,\boldsymbol{x},\omega\right)d^3x\,, \tag{3.3}$$

where u_I is the incident wavefield, g is a Green's function, and $\boldsymbol{x}$ is a 3D vector describing a location in the earth. The integration is performed over the volume D, which is taken to be the half-space below the earth's surface. Equation (3.3) is produced by first using Green's theorem to solve a Helmholtz equation for a bandlimited impulsive source at $\boldsymbol{x}_s$, in a medium that can be described to have a wavespeed $v\left(\boldsymbol{x}\right)$ obeying

$$\frac{1}{v^2\left(\boldsymbol{x}\right)}=\frac{1}{c^2\left(\boldsymbol{x}\right)}\left(1+\alpha\left(\boldsymbol{x}\right)\right), \tag{3.4}$$

where $c\left(\boldsymbol{x}\right)$ is the background wavespeed and $\alpha\left(\boldsymbol{x}\right)$ is a perturbation with respect to the background wavespeed. Then, the Born approximation is applied, which amounts to arguing that the part of the already scattered wavefield interacting with the reflector is small compared to the incident wavefield interacting with the reflector, and can thus be neglected. This is the reason that u_S does not appear on both sides of equation (3.3), and thereby linearizes the inversion problem. After representing the incident wavefield as

$$u_I\left(\boldsymbol{x},\boldsymbol{x}_g,\omega\right)=F\left(\omega\right)g\left(\boldsymbol{x},\boldsymbol{x}_s,\omega\right), \tag{3.5}$$

where g is a Green's function and $F\left(\omega\right)$ amounts to a bandlimiting source wavelet, and then using a high-frequency approximation, which allows Green's functions to be represented in terms of a ray-theoretic amplitude A and a traveltime τ as

$$g\left(\boldsymbol{x},\boldsymbol{x}_0,\omega\right)\sim A\left(\boldsymbol{x},\boldsymbol{x}_0,\omega\right)e^{i\omega\tau\left(\boldsymbol{x},\boldsymbol{x}_0\right)}, \tag{3.6}$$

the scattered wavefield can be written as

$$u_S\left(\boldsymbol{x}_g,\boldsymbol{x}_s,\omega\right)\approx\omega^2F\left(\omega\right)\int d^3x\frac{\alpha\left(\boldsymbol{x}\right)}{c^2\left(\boldsymbol{x}\right)}a\left(\boldsymbol{x},\boldsymbol{\xi}\right)e^{i\omega\phi\left(x,\xi\right)}, \tag{3.7}$$

where now the source and receiver coordinates have been parameterized in terms of a single 2D surface coordinate vector $\boldsymbol{\xi}$, and

$$\phi\left(\boldsymbol{x},\boldsymbol{\xi}\right)=\tau\left(\boldsymbol{x},\boldsymbol{x}_s\left(\boldsymbol{\xi}\right)\right)+\tau\left(\boldsymbol{x}_g\left(\boldsymbol{\xi}\right),\boldsymbol{x}\right), \tag{3.8}$$

the sum of the traveltime between the source and the image point and between the image point and the receiver, and

$$a\left(\boldsymbol{x},\boldsymbol{\xi}\right)=A\left(\boldsymbol{x},\boldsymbol{x}_s\left(\boldsymbol{\xi}\right)\right)A\left(\boldsymbol{x}_g\left(\boldsymbol{\xi}\right),\boldsymbol{x}\right), \tag{3.9}$$

the product of the spreading factors for the raypath between the source and the image point and between the image point and receiver. Bleistein et al. (2001) design an inversion operator for the wavespeed perturbation of the form

$$\alpha\left(\boldsymbol{y}\right)=\int d\omega\int d^2\xi\;B\left(\boldsymbol{y},\boldsymbol{\xi}\right)e^{-i\omega\phi\left(\boldsymbol{y},\boldsymbol{\xi}\right)}u_S\left(\boldsymbol{x}_g,\boldsymbol{x}_s,\omega\right), \tag{3.10}$$

where $\boldsymbol{y}$ is a 3D vector representing positions in the earth, but in the output space, unlike $\boldsymbol{x}$ which represents the input space. B is an unknown factor which is then determined by substituting the representation of the scattered field from equation (3.7) into equation (3.10) to produce

$$\alpha\left(\boldsymbol{y}\right)=\int\omega^2F\left(\omega\right)d\omega\int d^2\xi\;B\left(\boldsymbol{y},\boldsymbol{\xi}\right)\int d^3x\,e^{i\omega\left[\phi\left(x,\xi\right)-\phi\left(y,\xi\right)\right]}\frac{a\left(\boldsymbol{x},\boldsymbol{\xi}\right)}{c^2\left(\boldsymbol{x}\right)}\alpha\left(\boldsymbol{x}\right) \tag{3.11}$$

and then recognizing that this equation will be true if it is equivalent to

$$\alpha\left(\boldsymbol{y}\right)\sim\int d^3x\,\delta\left(\boldsymbol{x}-\boldsymbol{y}\right)\alpha\left(\boldsymbol{x}\right), \tag{3.12}$$

where $\delta(\boldsymbol{x}-\boldsymbol{y})$ is a Dirac delta function. This approach allows the B factor to be determined by comparing equations (3.11) and (3.12) to yield

$$\delta(\boldsymbol{x}-\boldsymbol{y}) \sim \int \omega^2 F(\omega) d\omega \int d^2\xi \, B(\boldsymbol{y},\boldsymbol{\xi}) e^{i\omega[\phi(\boldsymbol{x},\boldsymbol{\xi})-\phi(\boldsymbol{y},\boldsymbol{\xi})]} \frac{a(\boldsymbol{x},\boldsymbol{\xi})}{c^2(\boldsymbol{x})}. \tag{3.13}$$

The reader is referred to Bleistein et al. (2001) for the details of how B is then found, which allows equation (3.10) to be rewritten as

$$\alpha(\boldsymbol{y}) = \frac{1}{8\pi^3} \int d^2\xi \frac{|h(\boldsymbol{y},\boldsymbol{\xi})| \, c^2(\boldsymbol{y})}{a(\boldsymbol{y},\boldsymbol{\xi})} \int d\omega \, e^{-i\omega\phi(\boldsymbol{y},\boldsymbol{\xi})} u_S(\boldsymbol{x}_g, \boldsymbol{x}_s, \omega). \tag{3.14}$$

The equivalent inversion formula for the velocity reflectivity, instead of the velocity perturbation itself is then

$$\beta(\boldsymbol{y}) = \frac{1}{8\pi^3} \int d^2\xi \frac{|h(\boldsymbol{y},\boldsymbol{\xi})|}{a(\boldsymbol{y},\boldsymbol{\xi}) |\nabla_y \phi(\boldsymbol{y},\boldsymbol{\xi})|} \int i\omega \, d\omega \, e^{-i\omega\phi(\boldsymbol{y},\boldsymbol{\xi})} u_S(\boldsymbol{x}_g, \boldsymbol{x}_s, \omega). \tag{3.15}$$

In equations (3.14) and (3.15), $h(\boldsymbol{y},\boldsymbol{\xi})$ is the Beylkin determinant (Beylkin, 1985), which arises because of a change of variables during the derivation of the inversion operator from ω and the surface coordinates $\boldsymbol{\xi}$ to the 3D wavenumber vector $\boldsymbol{k}$, which represents image point coordinates.

For the particular case of a shot record migration in a constant velocity medium, the result in equation (3.15) simplifies to

$$\beta(\boldsymbol{y}) = \frac{2y_3}{\pi c^2} \int d^2\xi \frac{r_s}{r_g^2} \cos\theta \int i\omega \, d\omega \, e^{-i\omega[r_s+r_g]/c} u_S(\boldsymbol{x}_g, \boldsymbol{x}_s, \omega), \tag{3.16}$$

where y_3 is just the third component of $\boldsymbol{y}$ (i.e. depth), r_s and r_g are the lengths of the vectors from the source to the image point and from the image point to the receiver,

respectively, and θ is half the opening angle between the source-to-image-point and receiver-to-image-point rays, as illustrated in Figure 3.1. Again, the reader is referred to Bleistein et al. (2001) for the complete derivation.

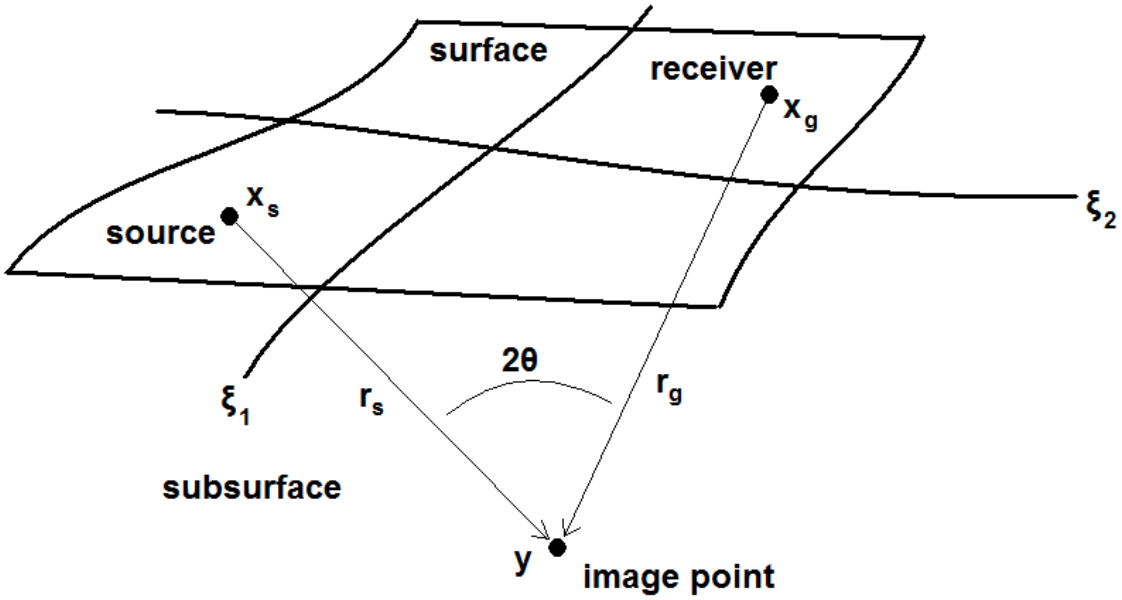


Figure 3.1: Illustration of source, receiver, and image point geometry in prestack migration, after Bleistein et al. (2001).

The prestack migrations performed on the exhaustive and decimated datasets in this study were accomplished by implementing equation (3.16) in MATLAB to produce a shot record migration algorithm. The equation was first converted to a discrete form and generalized to the case of a v(z) medium by replacing the constant velocity c in equation (3.16) with an average velocity, producing

$$\beta(\boldsymbol{y}) = \sum_{traces} \frac{2y_3}{\pi v_{avg}^{\ 2}} \frac{r_s}{r_g^2} \cos\theta \sum_{\omega} i\omega\, e^{-i\omega(t_s+t_r)} u_S\left(\boldsymbol{x}_g, \boldsymbol{x}_s, \omega\right), \tag{3.17}$$

where the outer sum is a sum over traces in the shot record, and the inner sum is over frequencies. In the exponential we now have traveltimes found by ray tracing through the velocity field instead of raypath lengths and a constant velocity. Equation (3.17) shows that the Bleistein et al. (2001) approach is just a particular way of performing conventional prestack Kirchhoff migration, where the image is formed when the input data are summed along a particular traveltime path while being multiplied by weights that are designed to produce the correct amplitude of the summation, including factors that correct for raypath length and obliquity.

3.3 2D results

To process the modelled 2D shot records, pre-existing functions in the CREWES MATLAB toolbox were used. Normal moveout correction was accomplished using the ***nmor*** function and the ***kirk_mig*** function was used to perform Kirchhoff poststack time migration. Kirchhoff prestack shot record migration was performed using the ***kirk_shot*** function. The default parameters were used for the migrations and the RMS velocities used were calculated with the ***vint2vrms*** function, using the true interval velocities from the geological model.

Figure 3.2 shows the sections produced using the processes of NMO correction followed by CMP stacking, for the six 2D datasets (shot spacings of 5m, 10m, 25m, 50m, 100m, and 200m). In addition to showing a reflection from the horizontal reflector and diffractions from the channel edges, regular artefacts occur in the images created from shot spacings of 25m and greater; the exhaustive dataset and the dataset with a 10m shot spacing produce essentially identical stacks. The spacing of the artefacts increases

correspondingly as the shot spacing from the original geometry increases, showing the link between the artefacts and the acquisition geometry. The artefacts appear to be confined to the region below the reflector. Amplitudes extracted along a constant depth slice that crossed the artefacts would display periodic amplitude variations that correlate to the acquisition geometry, which is the definition of footprint.

Figure 3.3 shows the sections produced by applying poststack migration to the CMP stacks from Figure 3.2. Unlike the stacks, in all six datasets the poststack migrations do not show a strong footprint. However, they do show a small amount of noise for large shot intervals, suggesting that the inclusion of aliased shot wavenumbers does produce a degradation in the image, though this degradation does not manifest as a coherent footprint as in the unmigrated case. The most obvious difference between the results from the six datasets is the degradation of the image of the channel as decimation increases. The channel edges are resolved much better in the less decimated datasets. The artefacts that were present in the unmigrated stacks have likely been reduced during the poststack migration because of the process of spreading energy over semicircles (for constant velocity, or equivalent constant traveltime surfaces for variable velocity), which would destroy the coherence of the artefacts, turning them into a more random noise-like manifestation. This observation that the footprint artefacts are not very prominent in the poststack migrated data is somewhat contrary to field data experience; this discrepancy may result from the extreme simplicity of the geological model, or from the lack of surface waves in the model data.

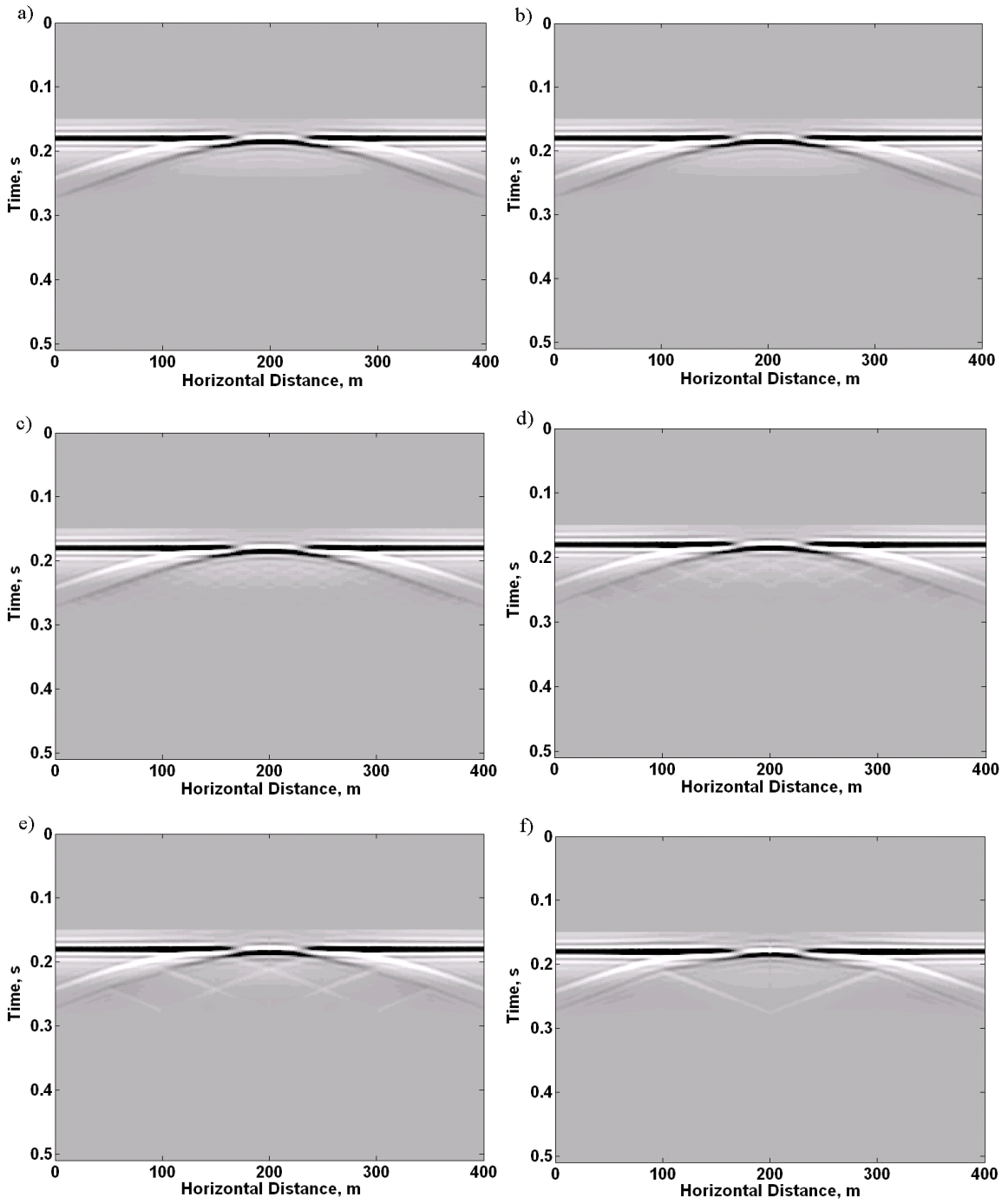


Figure 3.2: Common-midpoint stacks created using shot spacings of a) 5m, b) 10m, c) 25m, d) 50m, e) 100m, and f) 200m. Mean scaling applied.

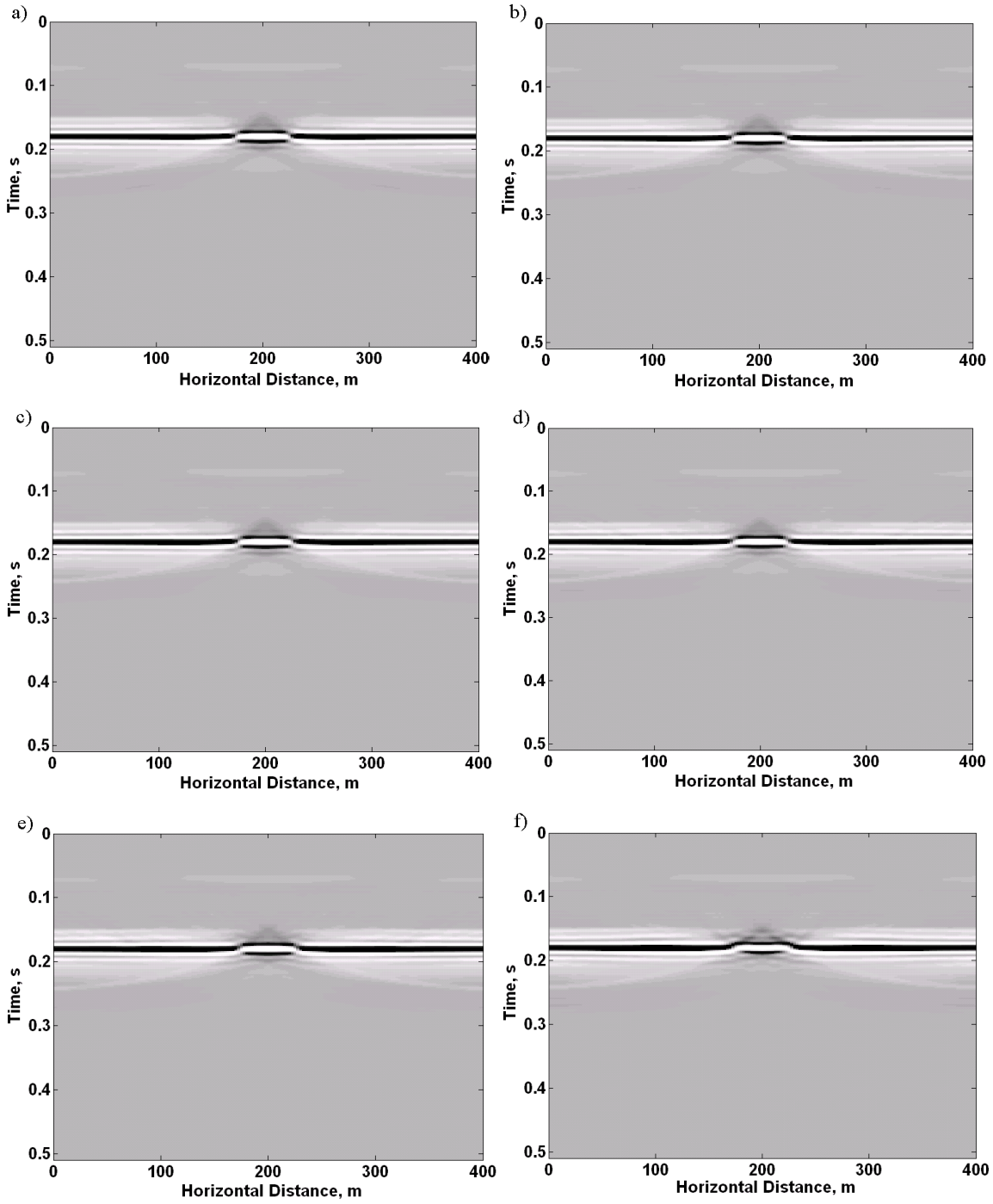


Figure 3.3: Poststack migrations applied to stacks created using shot spacings of a) 5m, b) 10m, c) 25m, d) 50m, e) 100m, and f) 200m. Mean scaling applied.

Figure 3.4 shows the sections produced using prestack migration for the six datasets. The sections produced using shot spacings of 5m and 10m are essentially identical; the sections produced using spacings of 50m, 100m, and 200m contain artefacts; the section produced using a spacing of 25m appears to also contain some faint artefacts. The artefacts seem to consist of residual "migration wavefronts", which is consistent with observations by Cary (2007). These artefacts would cause amplitude variations in reflection events occurring above the modelled reflector, resulting in acquisition footprint. At constant depth, the wavefronts are regularly spaced and if amplitudes were extracted along a depth slice that crossed those wavefronts, periodic amplitude variations (i.e. footprint) would be observed, in a manner similar to the unmigrated stacks.

Because the receiver spacing was constant in the six datasets, the sampling in any given shot record (common-shot gather) is identical for all datasets, despite the different shot spacings. However, the common-receiver gathers are different for the different shot spacings, with successively fewer traces as the shot interval increases. Figure 3.5 shows the common-receiver gathers for the receiver located at x=200m, and Figure 3.6 shows the f-k spectra for the gathers. Because these are common-receiver gathers, the wavenumber axis is k_S, the shot wavenumber. The f-k spectra show that for shot spacings of 5m, 10m, and 25m, the common-receiver gathers are unaliased. The 25m spacing produces a saturated spectrum, on the verge of aliasing. The shot spacings of 50m, 100m, and 200m produce aliasing of the shot wavenumbers. The observation can be made that (1) when aliasing is not present, footprint artefacts in the stacks and residual migration wavefronts in the prestack migrated sections do not appear, (2) when the

sampling is at the threshold of aliasing (25m shot spacing), artefacts begin to appear in the stacked section and prestack migrated section, and (3) when aliasing is present, footprint artefacts are also present. The onset of footprint artefacts in the images coinciding with the onset of aliasing in the common-receiver gathers is consistent with the hypothesis that the aliased source wavenumbers are causing the artefacts, though these results do not provide definitive proof of this idea. Since the wavenumber content of the stack is produced by a combination of the source and receiver wavenumbers, as $k_M = k_S + k_R$ (equation 1.4), these aliased source wavenumbers could manifest as the noise observed in the stacks. If the source interval was kept constant and the receiver spacing increased, it is likely that the same results would be produced. Increasing both the source and receiver sampling intervals would likely result in more prominent artefacts. These simulations were not performed as part of this study.

The results of these tests show that for the particular reflection modelled, the exhaustive sampling interval of 5m was excessively small. This is because the exhaustive sampling interval was calculated from v_{MIN} in the geological model, but only the reflection from the interface at the channel level was modelled. As a result, the datasets produced that simulated shot spacings of 5m and 10m were both adequate to prevent aliasing. However, if the shallower reflections or direct arrivals were included in the model the 5m spacing would be required to prevent aliasing.

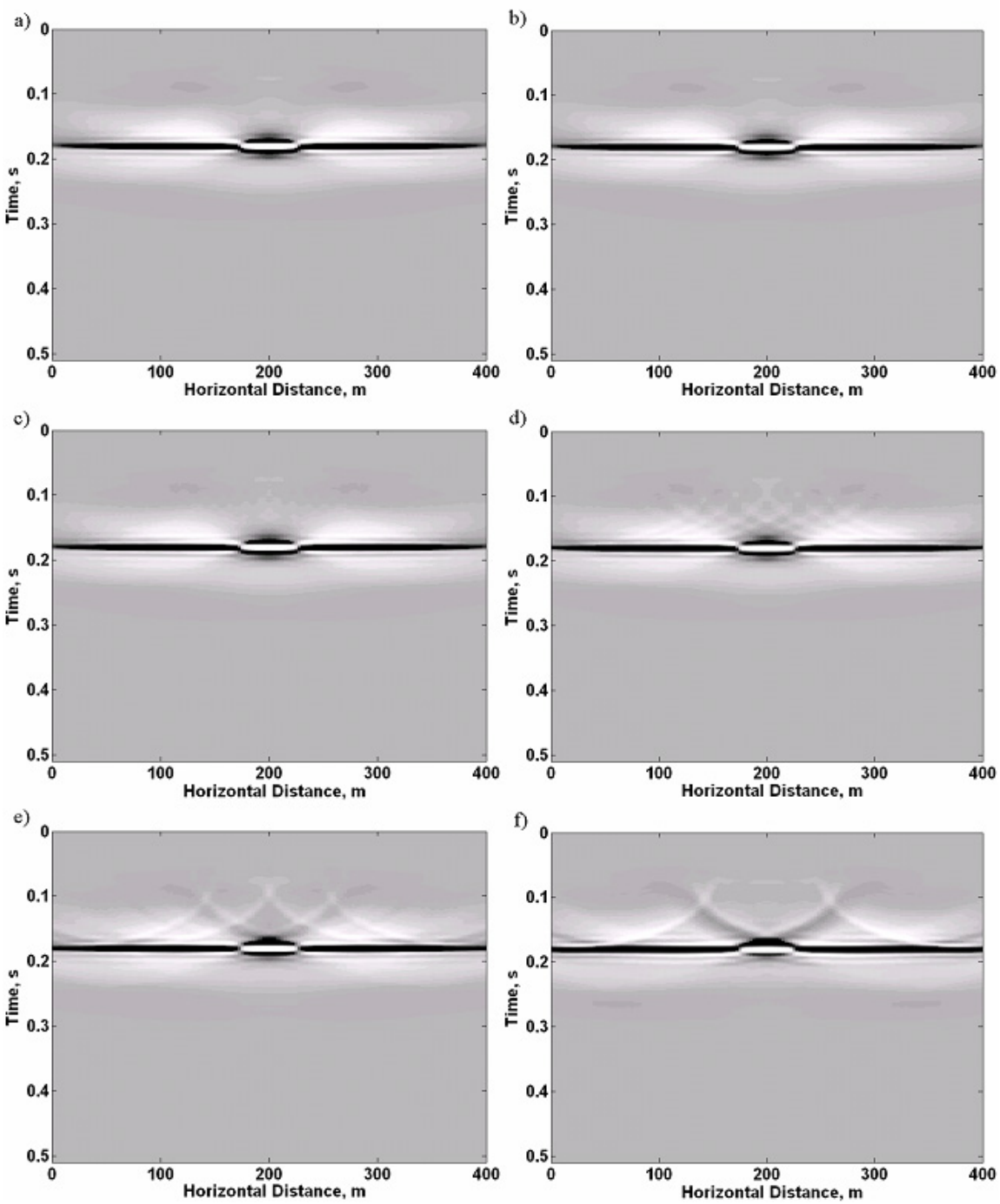


Figure 3.4: Prestack-migrated sections created using a) 5m, b) 10m, c) 25m, d) 50m, e) 100m, and f) 200m shot intervals.

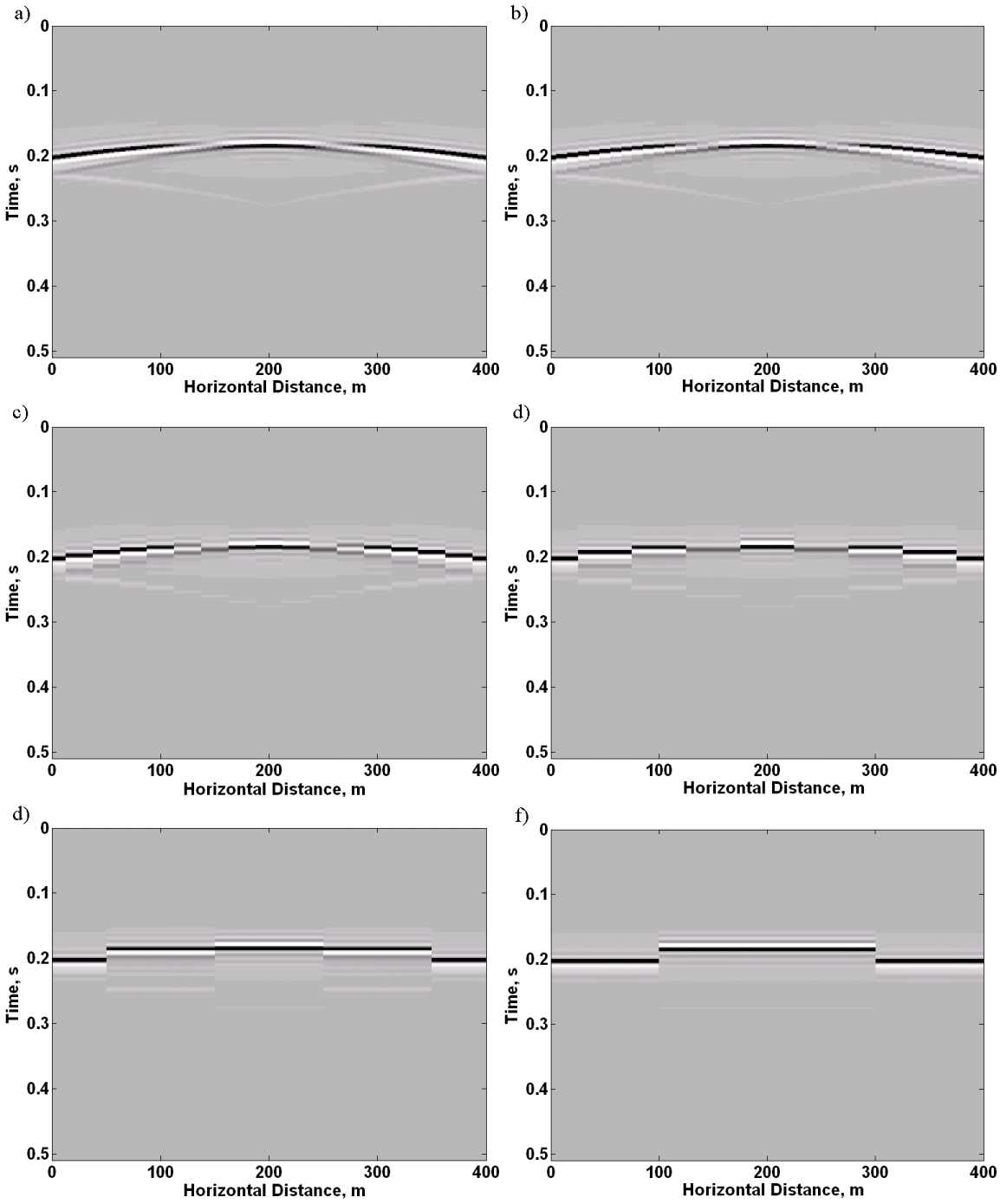


Figure 3.5: Common-receiver gathers created using a) 5m, b) 10m, c) 25m, d) 50m, e) 100m, and f) 200m shot intervals.

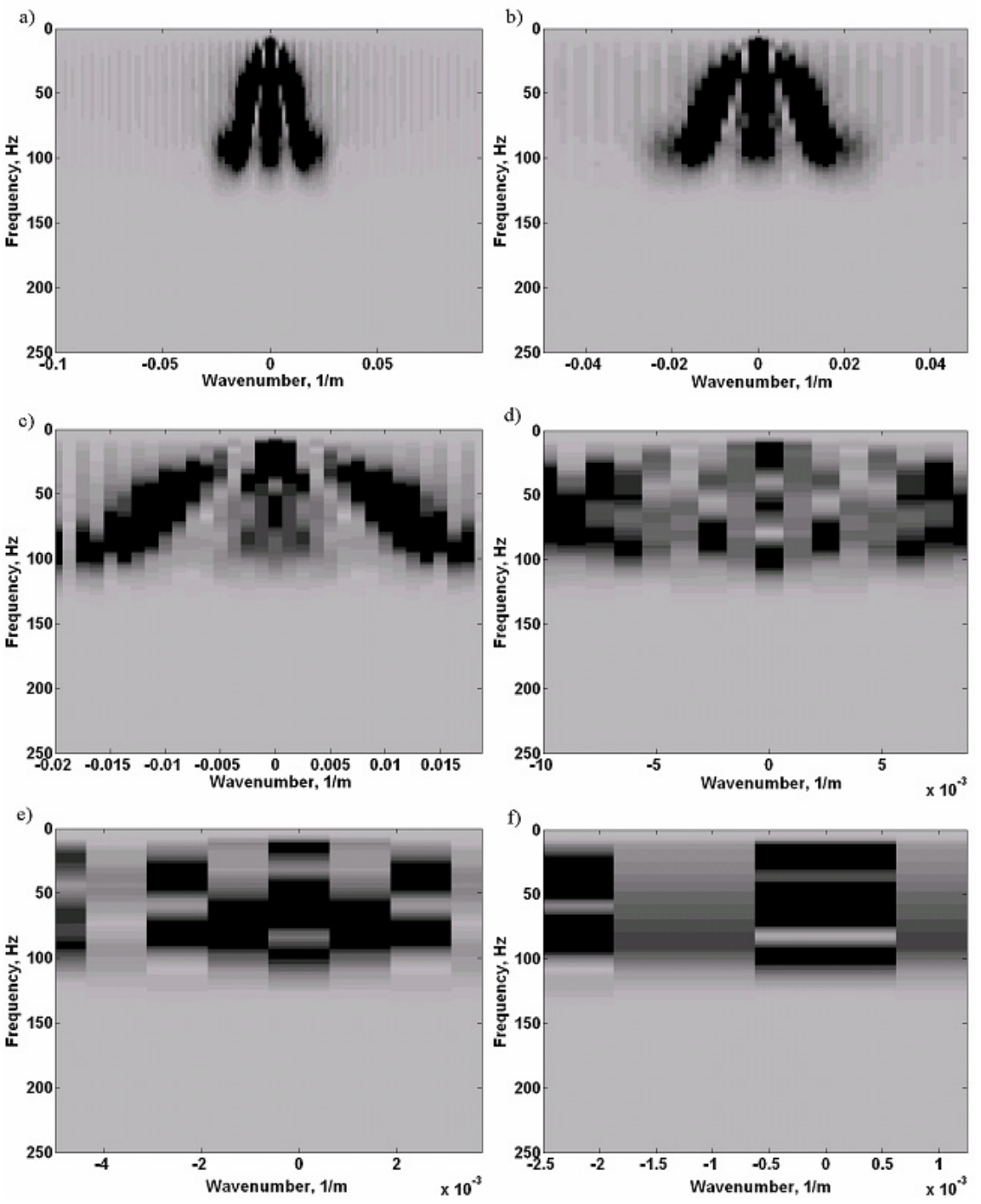


Figure 3.6: The f-k spectra of common-receiver gathers created using a) 5m, b) 10m, c) 25m, d) 50m, e) 100m, and f) 200m shot intervals.

Cary (2007) described a similar 2D footprint simulation to the one performed here, which produced residual migration wavefronts after shot-record migrations. Using a common-offset migration algorithm also produced the same results; incomplete cancellation of migration wavefronts occurred when the shot spacing was not fine enough. However, applying partial NMO before migration to correct the offset of each trace to that of the centre of the offset bin was successful in reducing the presence of the footprint. In a different study, Cary (1999a) showed the ability of partial stacking of common-offset gathers before migration to help overcome spatial aliasing associated with sparse sampling. In that paper, he commented on the ability of the technique to increase the fidelity of reflection waveforms of shallowly dipping events in the final migrated images, though the quality of steeply dipping events suffered when aliasing was severe. These studies suggest that regularization in the offset dimension is helpful in increasing the accuracy of reflection amplitudes and, perhaps in a related way, in reducing footprint artefacts. The work is also consistent with ideas about the role of spatial aliasing in footprint; the reduction in the severity of spatial aliasing being achieved, in this case by imposing a model (i.e. horizontal reflectors) during partial NMO correction, is associated with the footprint reduction.

The notion that partial stacking before migration helps reduce footprint is consistent with the observation in this study that full stacking before migration (i.e. CMP stacking followed by poststack migration) also does not seem to result in strong footprint artefacts. This might suggest that poststack migration is the optimal processing method to avoid footprint. However, this is contradicted by the fact that, as mentioned previously, poststack migrations of field data are known to contain significant footprint

artefacts. Also, the process of poststack migration is not theoretically sufficient for most geological situations. Though it produces good images in this model, it is inferior compared to prestack migration when more complicated velocity and reflectivity structures are present.

3.4 3D results

The same approach used in 2D was followed for the 3D datasets. Both the exhaustive and decimated datasets were subjected to several processing techniques, in order to examine the interaction between sampling and various imaging algorithms. In all cases, exact model velocities were used and deconvolution was not applied. However, in 3D more than one prestack migration algorithm was used. Table 1 summarizes the different flows. Processing flows labelled "University of Calgary" were performed in MATLAB, producing a CMP stack, a Kirchhoff poststack migration of that stack, and also a Kirchhoff prestack migration. Both "University of Calgary" migration codes were written as part of this study. The prestack migration algorithm (***kirk_shot3Dfz*** in the CREWES MATLAB toolbox) is a Kirchhoff shot record migration incorporating Bleistein shot weights (Bleistein, et al., 2001), as described in a previous section. The algorithm is a prestack time migration that produces images at depth levels specified by the user. Time shifts involved in the summation over traveltime paths are performed by frequency-domain phase shifts applied to slices of data around each event. For this study, a 60° scattering angle limit was used. The poststack migration algorithm (***kirk_stack3D*** in the CREWES MATLAB toolbox) is an extension of the shot record migration algorithm to the case of coincident source and receiver positions.

Two additional prestack migration algorithms were applied to the data by industrial partners in this study. Algorithm A is a Kirchhoff common-offset-vector migration (Cary, 1999b) which involves the formation of common-offset-vector (COV) volumes, each containing traces with a limited range of inline and crossline offsets. Partial stacking may be involved in forming these COV volumes. Each COV volume is migrated separately; the final image is formed by stacking the migrated COV volumes. Algorithm B is a Kirchhoff common-offset migration, which involves the formation of common-offset (CO) volumes, each containing traces with a limited range of absolute source-receiver offsets. These CO volumes are migrated separately using empirical weights inspired by Kirchhoff poststack migration theory. Bleistein et al. (2001) weights can also be implemented in this algorithm; however, for this dataset the difference in the stacked images produced using Bleistein weights and these empirical weights was negligible. Within a single CO volume migration, the offset-range limited fold is computed for each input trace, and the trace is weighted by the inverse of this fold prior to migration. As in the COV migration case, the final image is formed by stacking the migrated CO volumes.

Table 3.1: Summary of processing methods applied to the model data.

Method	Description
UofC Stack	Deterministic gain, NMO correction, mute, stacking
UofC Poststack Migration	Kirchhoff poststack migration of UofC Stack, using Bleistein shot weights for zero offset
UofC Prestack Migration	Kirchhoff shot record migration using Bleistein shot weights, mute, stacking of migrated shots
Prestack Migration A	Formation of common-offset-vector volumes, Kirchhoff migration, stacking of migrated COV volumes
Prestack Migration B	Formation of common-offset volumes, weighting by offset-range limited fold, Kirchhoff migration, stacking of migrated CO volumes

Figure 3.7 through Figure 3.11 show time and depth slices from processed volumes produced by applying the five processing methods. Each figure contains the slices corresponding to the appropriate time or depth of the three reflectors in the model from both the exhaustive and decimated datasets. All slices are scaled individually to their maximum and minimum amplitudes and are plotted using a linear colour scale.

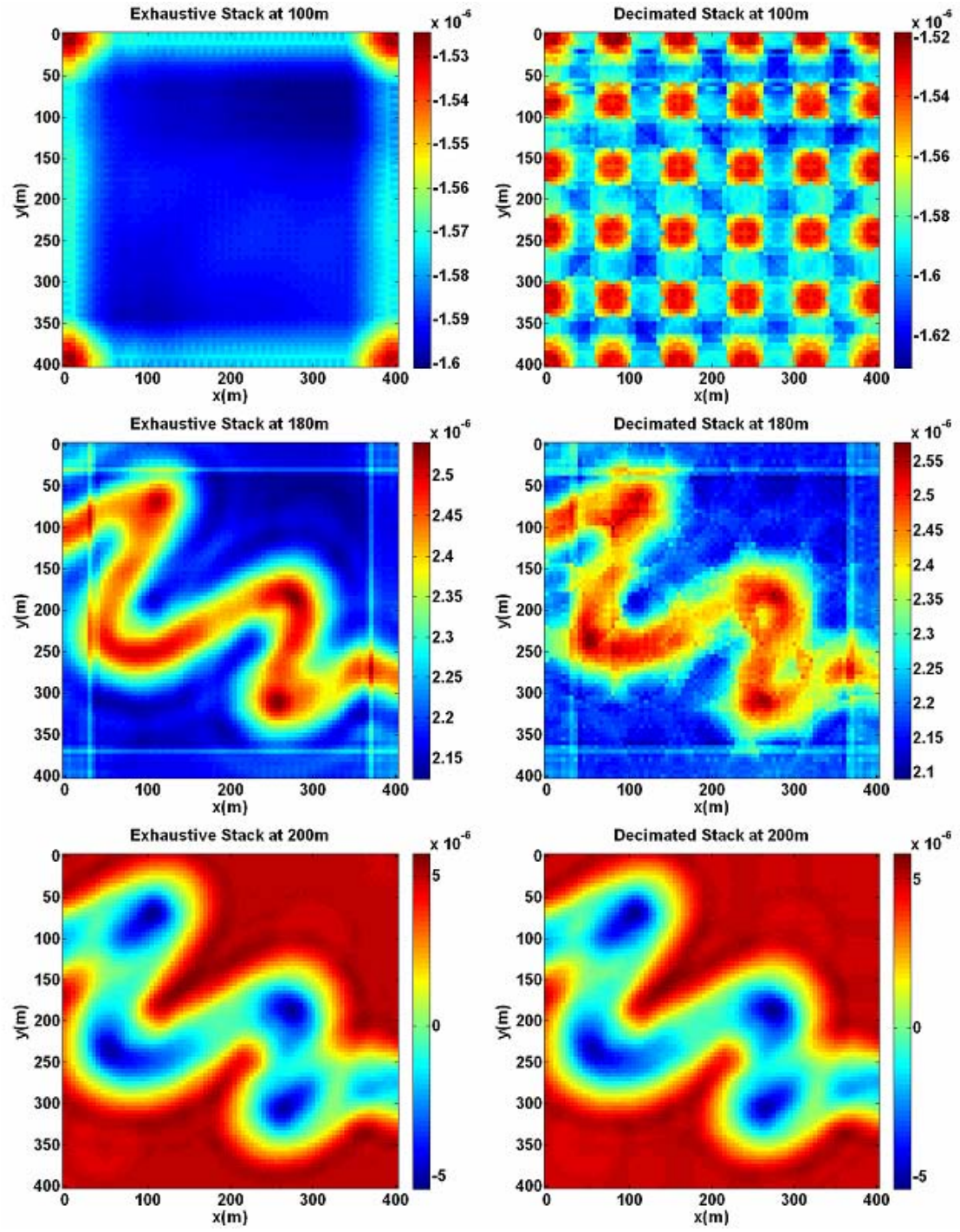


Figure 3.7: Time slices from UofC stacks for the exhaustive and decimated datasets.

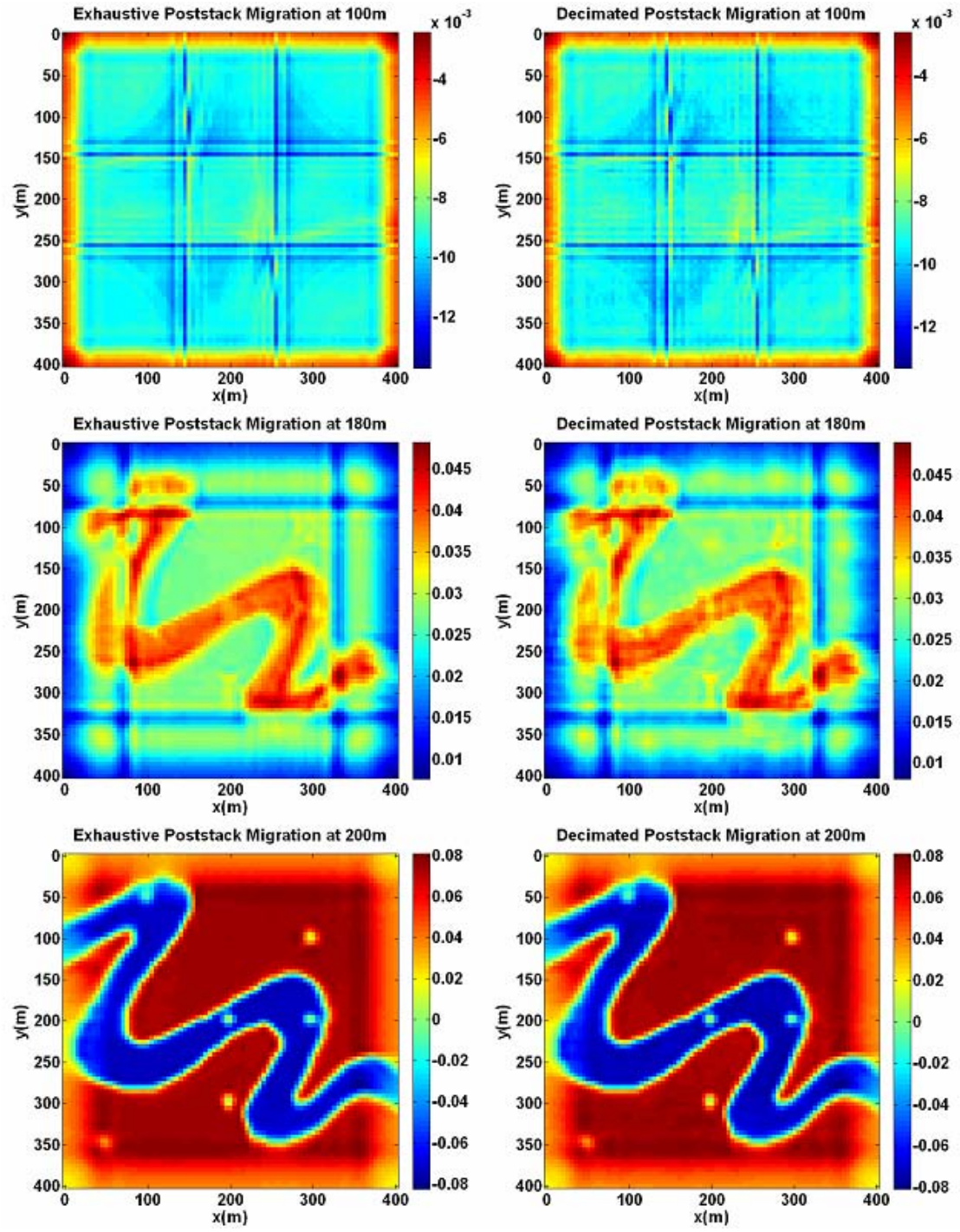


Figure 3.8: Depth slices from UofC poststack migrations for the exhaustive and decimated datasets.

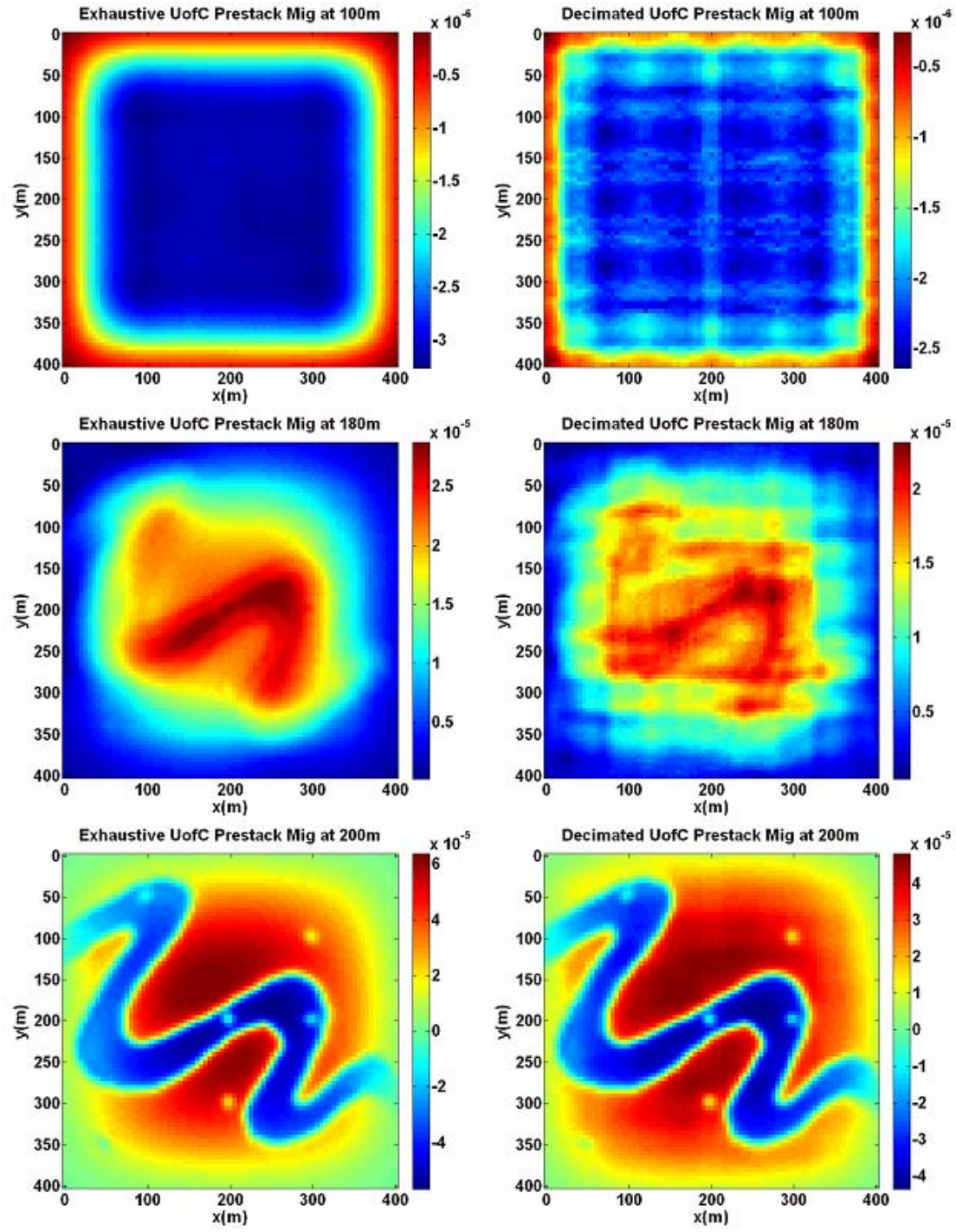


Figure 3.9: Depth slices from UofC prestack migrations for the exhaustive and decimated datasets.

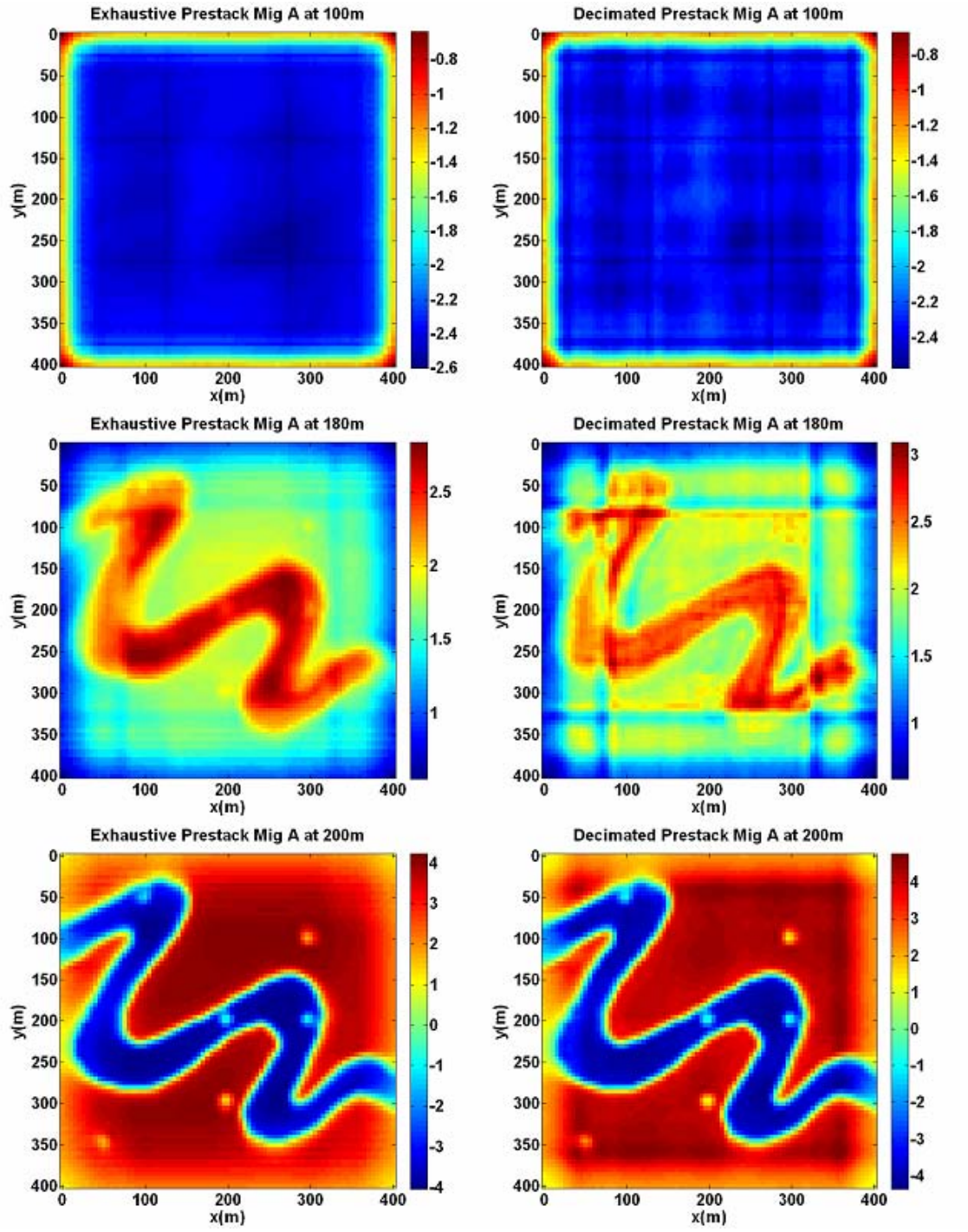


Figure 3.10: Time slices from Algorithm A prestack migrations for the exhaustive and decimated datasets.

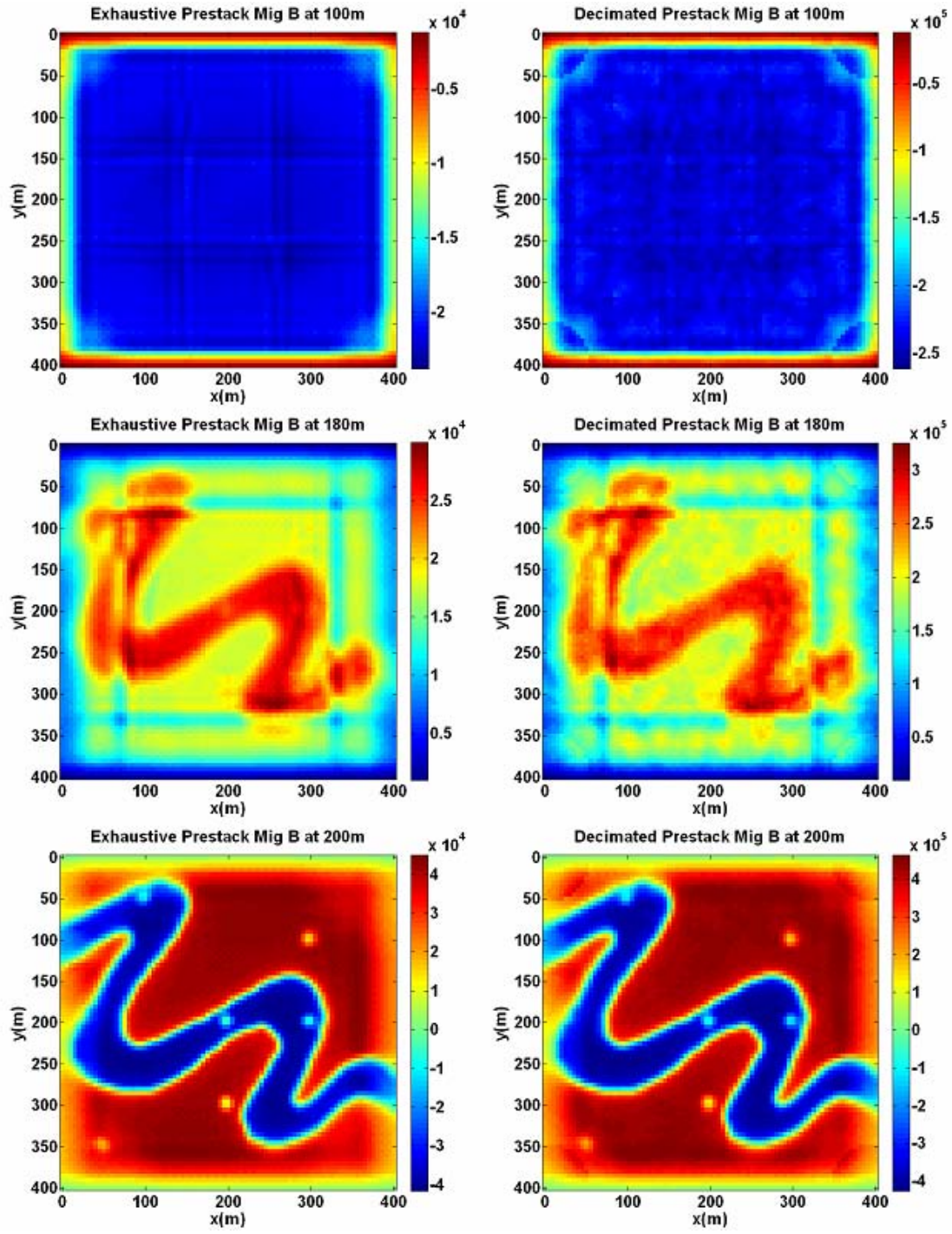


Figure 3.11: Time slices from Algorithm B prestack migrations for the exhaustive and decimated datasets.

The processed results from the exhaustive dataset show high-quality images of the reflectivity structure of the geological model. Except for the edges of the survey, images of the shallow featureless reflector generally contain very uniform amplitudes. The migrated images of the channel show well-defined boundaries and crisp point scatterers. The images of the reflector at 180m contain an imprint of the channel, even though the reflection coefficient was constant at that level. This is due to wavelet sidelobes from the nearby channel reflection event, caused by the non-causality of the wavelet used in modelling. The noticeable artefacts in the processed exhaustive dataset are edge artefacts on shallow reflectors, especially on the UofC poststack migration (Figure 3.8), caused by a lack of absorbing boundaries or edge tapering in the migration. In Figure 3.11, edge artefacts on the 180m reflector are also evident; again, their presence is due to a lack of edge tapering in the migration (in this case, to save run time). The UofC prestack migration (Figure 3.9) exhibits a strong aperture imprint. The industrial weighting schemes appear to result in images without strong aperture imprints, as well as reduced internal footprint artefacts.

We define footprint as any features present in an image of the featureless reflector; by this definition there is footprint in the exhaustive dataset from finite source-receiver coverage on the surface and from inadequacies in the processing algorithms. However, the more typical footprint observed in field data is observed in images from the decimated dataset. This footprint consists of periodic amplitude variations in the interior of the survey; these artefacts are also algorithm-dependent. The artefacts are especially apparent on the two featureless reflectors. Since those two reflectors are above the channel reflector, any residual migration wavefronts associated with the channel reflector

would be crosscut by the slices at the two featureless reflectors, resulting in the observed footprint. This observation suggests that footprint artefacts are a function of not only the acquisition geometry, but also the subsurface reflectivity structure, especially those reflectors occurring below the zone where footprint is observed.

With each depth slice scaled independently it is somewhat difficult to visually assess the severity of the footprint artefacts. This prompted an attempt to quantify the footprint as a percent variation in amplitude between the decimated slice and exhaustive slice. The percent variations were calculated by first scaling the decimated slice by a constant. The constant, c, is calculated by least-squares; the sum of the squared point-by-point differences between the exhaustive slice and (c*decimated slice) is minimized. Then the result of the point-by-point difference (exhaustive slice – c*decimated slice) is divided by the maximum absolute amplitude of the exhaustive slice. Multiplication by 100% produces a measure of percent variation. The results of this measure are shown in Figure 3.12 through Figure 3.14 for the shallow featureless reflector and the channel reflector.

Since a stack is essentially an average of traces over offset in a common-midpoint gather, trivially there will be no footprint if all traces are the same. However, even in the case of a horizontal featureless reflector, NMO-corrected traces will exhibit variations due to NMO stretch; in field data, additional differences will occur because of coherent noise, multiples, velocity errors, AVO, and imperfect gain, among other factors. Still, if a survey involves homogeneous offset and fold distributions in all bins, footprint will not be observed since the same traces are being averaged; this case is represented by the exhaustive dataset. However, if traces show variation with offset and the survey involves

large changes in the distributions of offset and fold then footprint is likely to occur; this case is represented by the decimated dataset. As shown in Figure 3.12, variations in amplitude of up to 4% on the featureless reflector and up to 6% at the channel were produced. The amplitude variations are highly regular on the featureless reflector.

In the case of poststack migration, the data have already undergone a regularization process during stacking. Since poststack migration can be thought of as a process of spreading amplitudes over constant-traveltime surfaces (hemispheres in the constant velocity case), then it could potentially smooth small-scale footprint that would be observed in a stack. However, if a strong footprint existed in the stack before migration, the amplitude variations would prevent the proper cancellation of migration wavefronts, resulting in footprint after poststack migration as well. Figure 3.13 shows that, compared to the stack differences from Figure 3.12, the footprint observed after poststack migration is somewhat less coherent; still, recognizable periodic amplitude variations remain, producing percent variations of up to 6% on the featureless reflector and up to 5% at the channel level.

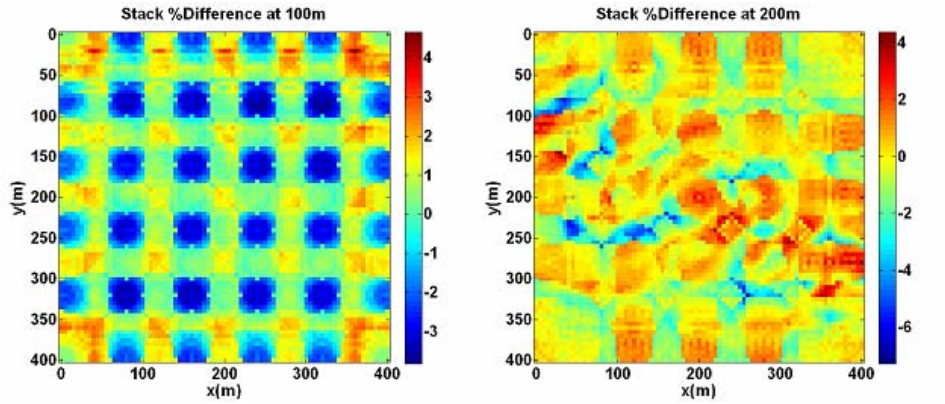


Figure 3.12: Percent difference plots for stacks.

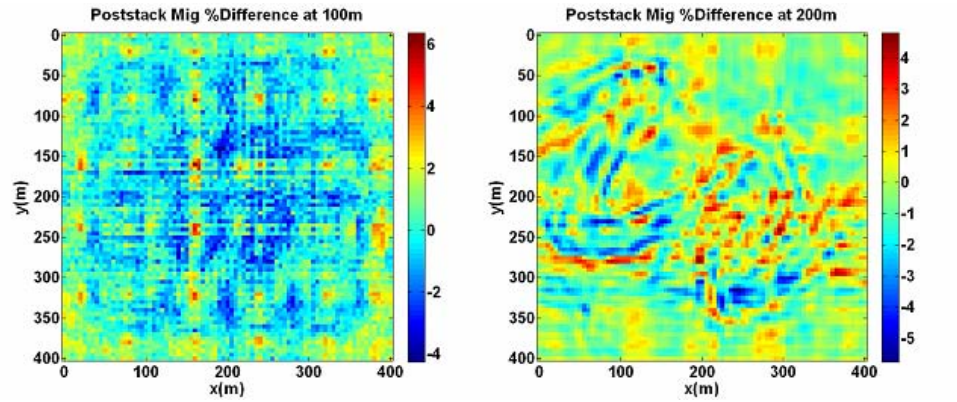


Figure 3.13: Percent difference plots for poststack migrations.

In the prestack migration case, footprint may consist of residual migration wavefronts similar to those shown in the previous 2D simulations. The three algorithms used in this study show large differences in observable footprint, suggesting that migration weights and regularization methods are likely key to reducing the impact of poor sampling. The UofC algorithm, which does not involve any fold compensation methods, shows the largest percent amplitude variations: up to 24% on the featureless reflector and up to 17% at the channel (Figure 3.14). However, some of these differences are clearly not periodic; rather they are related to differences in the aperture effect of the exhaustive and decimated surveys. The current measure used to quantify footprint is unable to separate the two types of variations. The prestack migrations performed using industry-standard algorithms show somewhat smaller amplitude variations: 7% variation on the featureless reflector and 8-14% variation on the channel reflector.

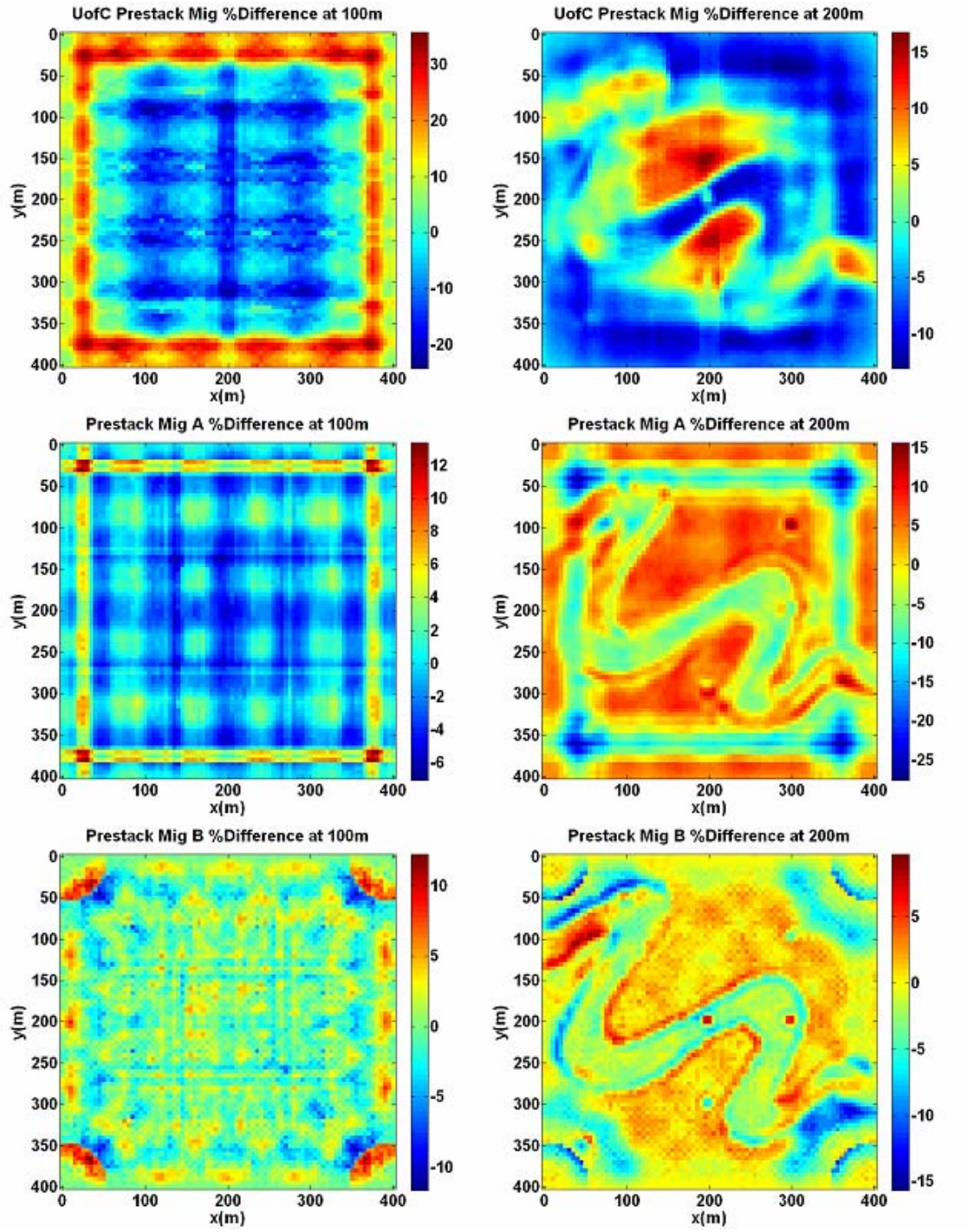


Figure 3.14: Percent difference plots for prestack migrations at the shallow featureless reflector (left-hand column) and at the channel (right-hand column). Each row compares a particular migration algorithm run on the decimated dataset with the same algorithm run on the exhaustive dataset.

3.5 Summary

The exhaustive and decimated datasets produced in Chapter 2 were processed using several methods to observe the resulting footprint artefacts. The purpose of using more than one processing algorithm was to allow for observations to be made about the differences in footprint resulting from different algorithms. The methods used were conventional common-midpoint stacking following normal-moveout correction, poststack Kirchhoff migration of the stacked data, and prestack Kirchhoff migration. In 2D, a single Kirchhoff shot-record migration was used, based on the theory of Bleistein et al. (2001). In 3D, three different Kirchhoff migration algorithms were used; the same Bleistein shot-record migration as was used in 2D (except modified for 3D data), a common-offset-vector migration, and a common-offset-weighted migration. The results of the data processing in this study reinforce the concept that although generally referred to as “acquisition” footprint, footprint artefacts are truly a result of an interaction between the acquisition geometry and the processing flow applied to the data.

In 2D, significant footprint artefacts were observed in unmigrated stacks and in prestack migrated sections. The artefacts in the prestack migrations manifested as residual migration wavefronts. The spacing of the artefacts increased as the decimated shot interval increased, showing the link between the artefacts and the acquisition geometry. However, the footprint results were very different with the three different processing methods, showing that the processing itself is important in the production of footprint. The footprint artefacts appeared when the decimated shot interval was 25m or greater; when common-receiver gathers of the datasets were examined, the shot interval of 25m was found to correspond to the onset of spatial aliasing in the data. This supports

a connection between spatial aliasing and footprint, though the mechanism has not been determined.

By defining footprint as any features observed on an image of a featureless reflector, there were two broad classes of footprint produced in 3D. The first consisted of amplitude variations related to the edges of the survey, including edge artefacts and aperture effects; this type of footprint was observed in both the exhaustive and decimated datasets, and was observed to vary between processing algorithms. The second class of footprint consisted of amplitude variations in the interior of the survey; these variations are likely a product of inadequate spatial sampling that aliases the prestack wavefield. This premise is supported by the more prevalent occurrence of these artefacts in the decimated dataset. Observations of footprint in the decimated datasets are generally consistent with typical field data. In these simulations, observed footprint was (1) most severe after prestack migration, though highly variable using different prestack migration algorithms, (2) most organized in the unmigrated stack, and (3) somewhat randomized after poststack migration. Percent amplitude variations of up to 6% in stacked data, up to 6% in poststack migrated data, and up to 24% in prestack migrated data were observed. Both offset-domain industrial weighting schemes produced better images than the shot record migration, suggesting that modifying the way traces are weighted in prestack migration could be an effective means to achieve reduction in footprint. The reduced footprint in stacked and poststack migrated data suggests that improvement in prestack migrated data could also result from regularization, accomplished perhaps by interpolation or partial stacking.

Chapter Four: Delta weighting method and results

4.1 Introduction

The previous chapter demonstrated how footprint expresses itself in prestack migrations in 2D and 3D. In the 2D simulations, footprint was observed as residual migration wavefronts. The 3D simulations demonstrated that the choice of prestack migration algorithm has an effect on the observed footprint. Different types of weighting in Kirchhoff prestack migrations produce many of the differences between algorithms. Weights can be applied to traces before migration, during migration, and after migration. The observation in 3D footprint simulations that different migration algorithms produced such different results motivated an attempt to improve the weighting in the Kirchhoff shot-record migration used in Chapter 3. The choice was made to stay with a shot-record migration, instead of moving to migrating other types of gathers such as common-offset gathers, because in the absence of partial stacking before migration, the domain in which migration is implemented should not matter. With the Kirchhoff method, each trace could be migrated independently; it is only the weights that are applied to each trace that give rise to differences in the final image. This suggested that weights could be used specifically to target footprint. In this chapter, the development of a migration weighting method is described. The method is based on the concept of compensating for irregular illumination of each image point. Incomplete sampling of the wavefield in surface coordinates (shot and receiver x and y), such as is produced in decimated datasets, correspondingly produces irregular sampling on the unit sphere surrounding the image point. Here the theory of the method is presented, as well as the results of applying the

method to the 2D and 3D datasets. In addition, the method is compared to a more conventional migration method, the common-offset weighting scheme.

4.2 Delta weighting

4.2.1 Illumination compensation

As discussed in Section 3.2.3, the shot-record migration algorithm that was used for the 2D and 3D simulations incorporated weights prescribed by Bleistein et al. (2001). The formulation used by Bleistein et al. (2001) incorporates a term known as the Beylkin determinant (Beylkin, 1985) that describes the influence of the source-receiver geometry at a given image point. The Beylkin determinant arises from the transformation from surface coordinates to subsurface coordinates. Consider a raypath connecting a source or a receiver and an image point; each raypath intersects a point on the unit sphere surrounding the image point. The ensemble of raypaths from regularly spaced sources and receivers on the surface does not produce uniform sampling on the unit sphere at an image point. The Beylkin determinant accounts for this effect by taking the ratio of a differential area element mapped out by a ray on the unit sphere and the differential area element mapped out by the same ray emergent on the recording surface (Bleistein, 1987). In essence, inclusion of the Beylkin determinant converts from an integration over uniform, continuous sources and receivers on a surface of infinite extent to an integration over uniform, continuous raypath coverage on the unit sphere. In the context of this study, with surface recording in a v(z) medium, even infinite sources and receivers on the surface will only illuminate the upper half of the unit sphere; as a result, we will refer to the “imaging hemisphere”.

However, despite the illumination compensation incorporated within the Beylkin determinant, the Bleistein migration formula is still an integral expression, corresponding to continuous sampling and no aperture limitations (i.e. sources and receivers at infinity). When sampling is irregular and discrete, the integral is approximated by a sum and irregular illumination of the imaging hemisphere results. This process is analogous to calculating the integral of a function, $\int f(x)dx$, numerically by converting it to a sum, $\sum_j f(x_j)\Delta x_j$. The result of the sum will only approximate the true integral. A first-order attempt is to sample the function and add up the samples, such as $\sum_j f(x_j)$. If the samples were dense and regularly spaced (small, constant Δx), then the result of the sum will only be inaccurate by a scale factor, since Δx can be factored out of the sum. Sampling with a small, constant Δx is similar to the exhaustive dataset, with infinite aperture. However, if Δx is not constant, when samples are sparse and irregularly spaced in the case of a decimated dataset, $\sum_j f(x_j)$ will not be a good approximation of the integral. Weighting each sample in the sum appropriately, such as in $\sum_j f(x_j)\Delta x_j$, is required.

With this analogy in mind, the approach taken was that additional weighting factors were required in the summation or stacking process after migration, to be used in conjunction with the Bleistein weights applied during migration. The combination of the weighting schemes attempts to convert from discrete, irregular sampling to continuous, regular sampling. In the spirit of the Beylkin determinant, the weights should achieve

uniform illumination of the imaging hemisphere. If we consider that the exhaustive survey represents ideal sampling, at least over a limited aperture, and that the Bleistein weights should convert that regular sampling on the surface to regular sampling on the imaging hemisphere, then our goal for a decimated survey should be to weight traces to mimic the exhaustive survey. In particular, we can keep track of hit counts on the imaging hemisphere and normalize by those hit counts. Industrial migration algorithms that are based on fold weights compensate for discrete, irregular sampling to some degree by performing a type of normalization, but in midpoint-offset coordinates. While angular illumination compensation is related to midpoint-offset weights, the two concepts are not the same, and moving from weighting in the surface acquisition domain to weighting in the image point domain may make the latter a more direct method for achieving normalization.

4.2.2 Delta angles

To accomplish the imaging hemisphere illumination compensation, weights are determined that are based on the angle delta. Delta describes the direction, which has both azimuth and dip components, of the vector that bisects the opening angle between the source-to-image-point ray and the receiver-to-image-point ray. For a given image point, each prestack trace (each source-receiver pair) defines a single delta. Figure 4.1 shows the delta vectors for an image point and a source-receiver pair in 2D and 3D. In 2D, the source, receiver, and image point are all in a single vertical plane, so the concept of azimuth is not required, other than keeping track of the sign of the delta dip angle. For a flat reflector, the common-midpoint or Snell's Law reflections all have delta dips of

zero; therefore, a map of zero delta dip hit counts is the same as a common-midpoint fold map. Like fold, zero delta dip hit counts are depth-independent (discounting top-mute effects), but in general the non-zero delta dip distributions change with image point depth. The non-zero delta dips extend the idea of fold to prestack data with non-Snell's Law raypaths, corresponding to diffractions. Even in the case of zero reflector dip, where the Snell's Law or zero delta dip reflections are most important, contributions from non-zero delta dips are necessary in order to image lateral reflectivity contrasts.

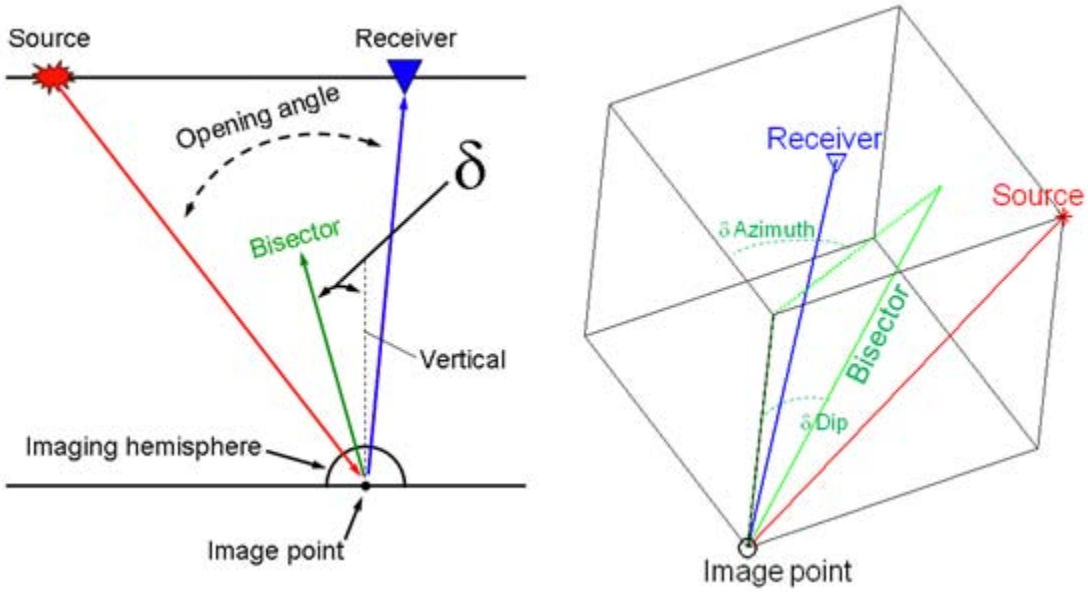


Figure 4.1: Delta angles in 2D and 3D, defining the orientation of the vector bisecting the opening angle between source and receiver rays. The positions of sources and receivers on the surface determine the distribution of delta angles on the imaging hemisphere.

When moving from the exhaustive survey to a decimated survey, the common-midpoint fold decreases in a way related to the geometry of the decimation (Figure 4.2). This is not surprising, and neither is the idea that this change should be compensated for

in prestack migration. The fold for non-zero delta dips changes as well, but not in the same exact way as the zero delta dips. The entire distribution of deltas changes in response to the removal of sources and receivers. It is likely that some footprint artefacts are a result of this delta angle imbalance, and that by weighting traces such that the ideal delta angle sampling is re-established, the footprint artefacts could be reduced. In order to achieve the same image point illumination with a decimated survey as was present with the exhaustive survey, the contributions of different deltas need to be weighted. Two types of weighting schemes can be considered: fold weights that involve dividing by decimated dataset delta hit counts, and also ratio weights that involve the ratio of exhaustive to decimated delta hit counts. The concept of delta-dependent weights in prestack migration is not new; it has been used in the context of true-amplitude migration to compensate for irregular illumination of image points (e.g. Albertin et al., 1999, Audebert et al., 2003). In those cases, the approach consisted of a replacement of the Beylkin determinant in the prestack migration weights by delta hit count weights, similar to those called delta-fold weights below. Here the attempt is to apply a similar concept to the case of footprint produced during prestack migration. However, the Bleistein weights, including the Beylkin determinant therein, are retained unchanged in the migration and the additional delta hit count weights are applied by multiplication during stacking of imaged shot records after migration.

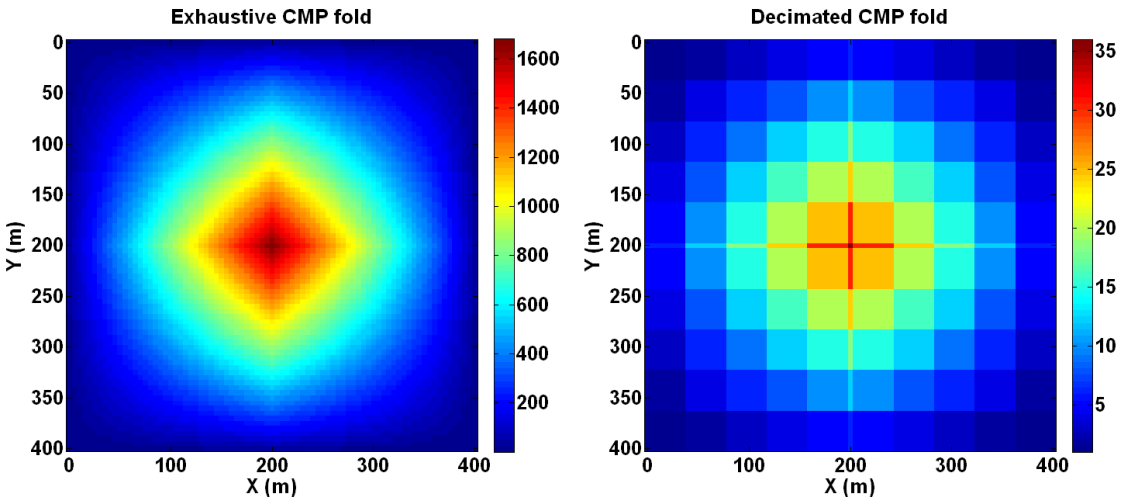


Figure 4.2: Common-midpoint fold for the exhaustive (left) and decimated (right) surveys from the 3D footprint simulation, as an example of delta hit count maps changing between exhaustive and decimated surveys, in this case for delta dip=0.

In a prestack migration, delta is directly related to the dip of the migration impulse response; the delta vector is the normal to the migration impulse response (Figure 4.3). Delta is a function of source, receiver, and image point position, so every point on the impulse response for a given trace corresponds to a different delta, since the position of the image point is changing. Figure 4.3 shows a 2D impulse response divided into delta-limited bins. In the simulations of 2D footprint from Chapter 3, the steep dips of migration wavefronts did not cancel in the case of highly decimated datasets. This suggests a mechanism by which weighting the different deltas on those migration wavefronts could have an impact on the footprint. In particular, down-weighting the large deltas could possibly reduce the presence of the artefacts.

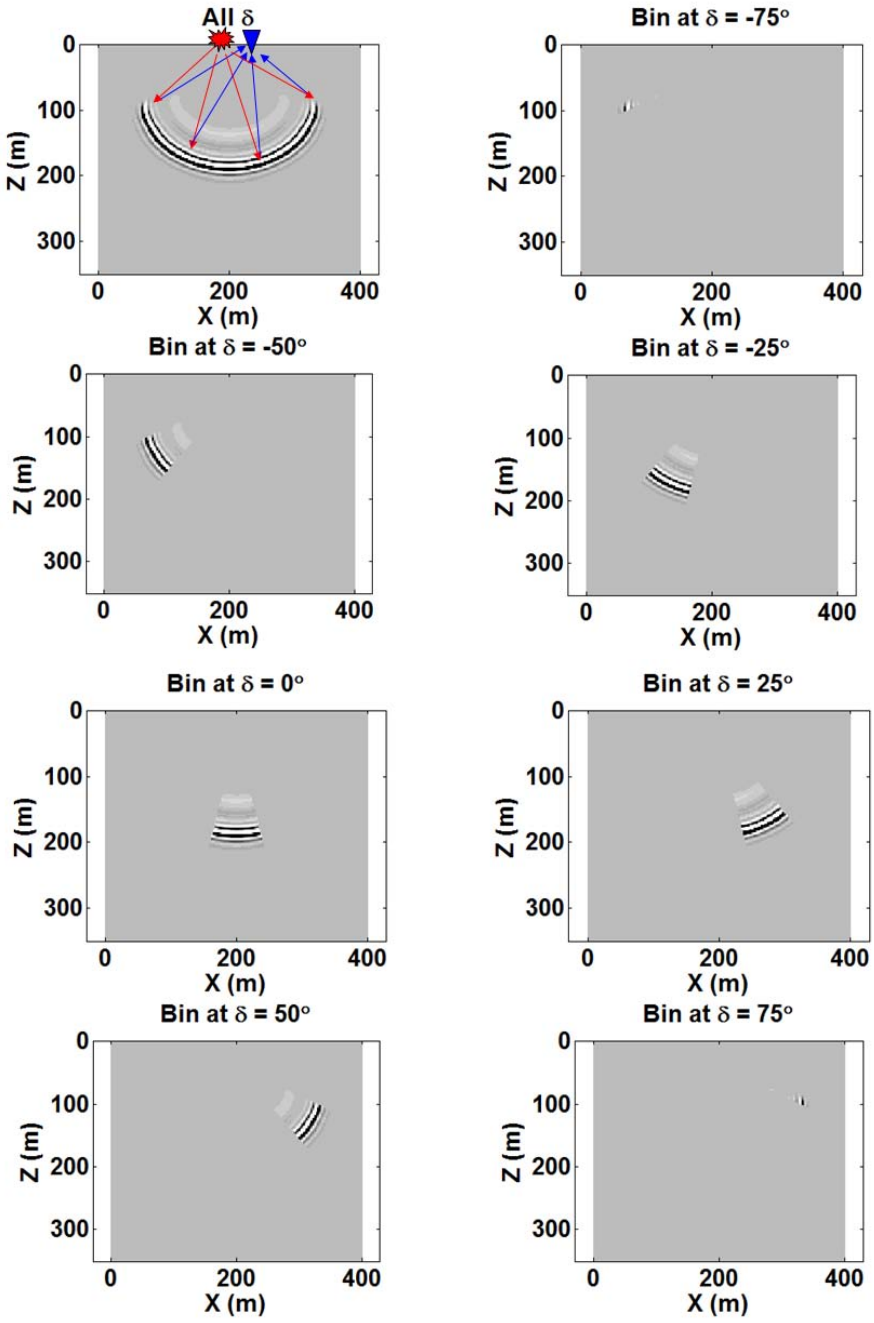


Figure 4.3: 2D migration impulse response divided into individual delta angle contributions. Each delta bin has a width of 25°. Delta angles above 60° were attenuated by the dip limit parameter in the migration. Delta is determined by the opening angle bisector vector (refer to Figure 4.1), which is also the normal to the impulse response.

4.2.3 Delta distributions and weights

To implement the method, the delta distribution for each image point is computed, for a set of predetermined delta bins. Computing these distributions requires ray tracing from all sources to all image points and from all receivers to all image points to find the bisector vector for each ray pair. Figure 4.4 shows the distributions for two image points from the 2D model, one in the middle of the model and one near the edge of the model, for the exhaustive survey and all five decimated surveys. Bins with a width of five degrees were used. Since the angles are determined by ray methods, binning of the delta angles appears to be necessary, otherwise the delta distributions of very closely spaced image points can be unrealistically different. However, the method for optimal binning has not yet been determined. Ray tracing to calculate the delta distributions does not constitute much of an additional computational burden, since the ray tracing step is already required in migration to compute traveltimes. In this example straight rays were used to compute the distributions. In practice, the delta computation step could be combined with the ray tracing step already being performed. As expected, Figure 4.4 shows that the image point in the middle of the survey displays a symmetric distribution of deltas, while the image point at the edge of the survey is dominated by deltas of only one sign. Figure 4.4 shows not only how the decimated surveys have fewer hits in each delta bin compared to the exhaustive survey, but also how the shape of the distribution changes as the decimation gets more extreme. The delta weighting schemes attempt to compensate for this.

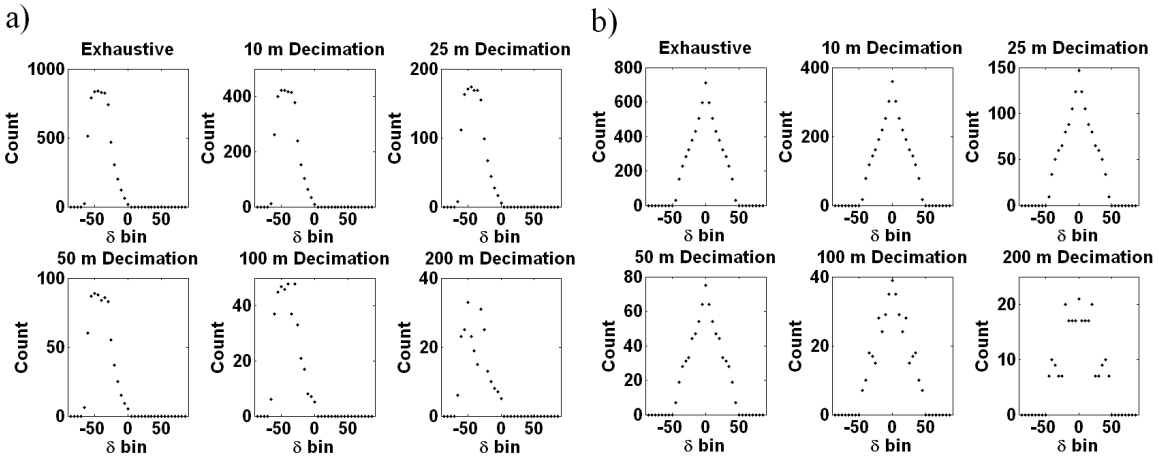


Figure 4.4: Delta bin hit count distributions for two image points from the 2D model. Left (a): image point at x=2.5m, z=200m, at the edge of the model. Right (b): x=200m, z=200m, in the middle of the model. The six panels for each image point are the exhaustive dataset, and the 10m, 25m, 50m, 100m, and 200m decimations.

The computation of delta distributions allows the weights for each delta-limited migrated trace contributing to that image point to be computed. Two possible weighting schemes can be considered: ratio weights and fold weights. For ratio weights the weight for a trace with a given delta is just the delta bin hit count in the exhaustive survey divided by the delta bin hit count in the decimated survey. Ratio weights attempt to convert the illumination of the decimated survey into that of the exhaustive survey, operating under the assumption that the Bleistein weights are designed (hence optimal) for exhaustive data with infinite aperture. For fold weights the weight is just one divided by the delta bin hit count in the decimated survey. Fold weights for the zero delta bin amount to just the familiar division by common-midpoint fold. Computation of fold weights only requires ray tracing for the shots and receivers in the decimated survey, while ratio weights involve ray tracing for the whole exhaustive survey, making them

more computationally intensive. Figure 4.5 shows both types of weights for the same two image points considered in Figure 4.4, again for the exhaustive survey and the decimated surveys. The ratio weights involve the exhaustive survey distribution in Figure 4.4 and dividing in turn by each decimated survey distribution. As expected, the ratio weights for the exhaustive survey are one for every bin, since in that case the weights are equal to the exhaustive hit count divided by itself. The weights for the decimated surveys change in response to the decimated hit counts changing, in a manner that attempts to compensate for the changing illumination. In general, the fold weights are larger at higher delta angles, while the ratio weights decrease as delta increases. This suggests that the ratio weights may be more effective in reducing the presence of the steep limbs of the residual migration wavefronts associated with footprint.

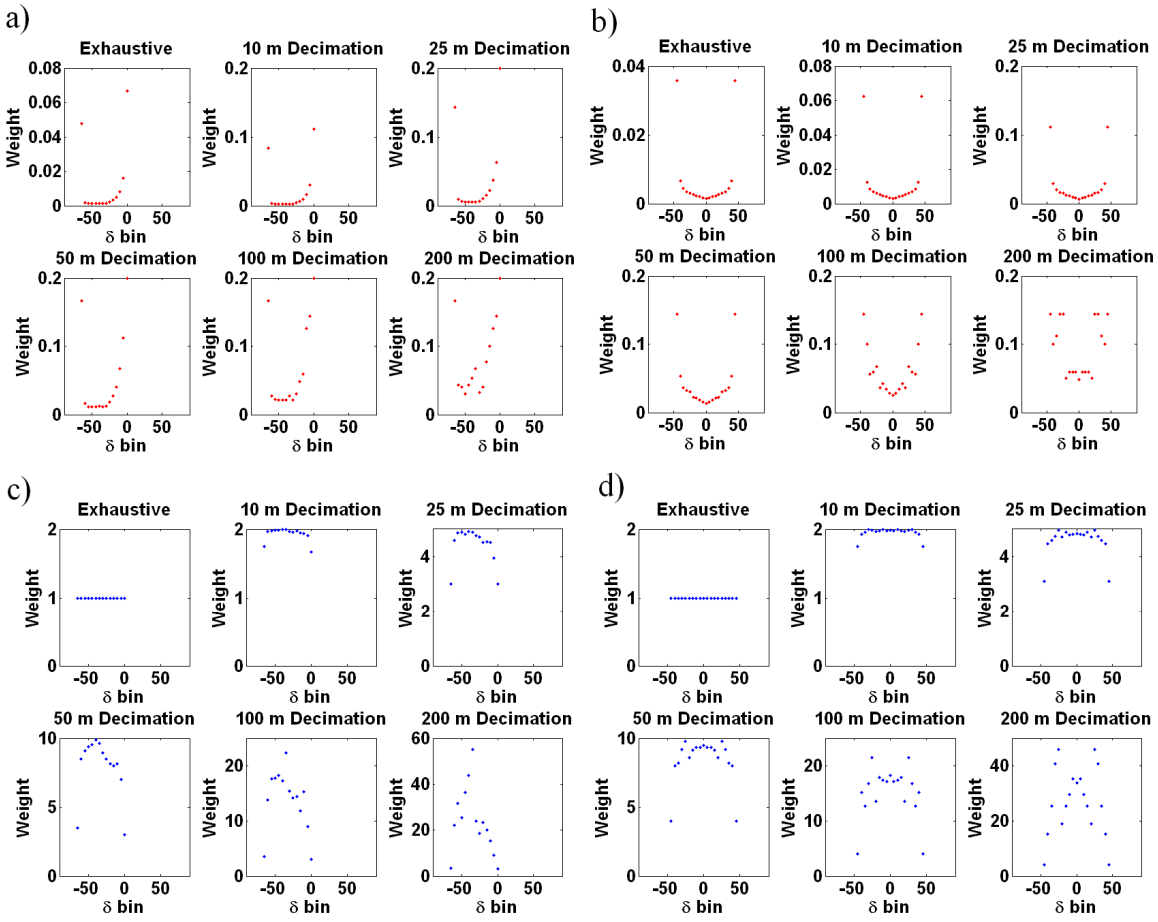


Figure 4.5: Fold weights (a, b) and ratio weights (c, d) for the two image points from Figure 4.4 for the exhaustive and decimated surveys. Left (a, c): image point at x=2.5m, z=200m, at the edge of the model. Right (b, d): x=200m, z=200m, in the middle of the model. Fold weights appear to emphasize large deltas in the middle of the model, while ratio weights down-weight the large deltas. Ratio weights do nothing to the exhaustive survey.

As an illustration of how the weighting scheme works in 3D, Figure 4.6 and Figure 4.7 illustrate delta fold maps for a single shot from the exhaustive and decimated surveys, located at x=240m, y=400m. The delta dip bins used were [0, 0.01), [0.01, 10), [10, 20), [20, 30), [30, 40), [40, 60), and [60, 90] degrees. The first bin is one that is close to only containing zero delta dip to demonstrate that the zero delta dip hit count is

the same as the common-midpoint fold in the case of a flat reflector; this is shown in Figure 4.6. Azimuth was not considered in this binning example.

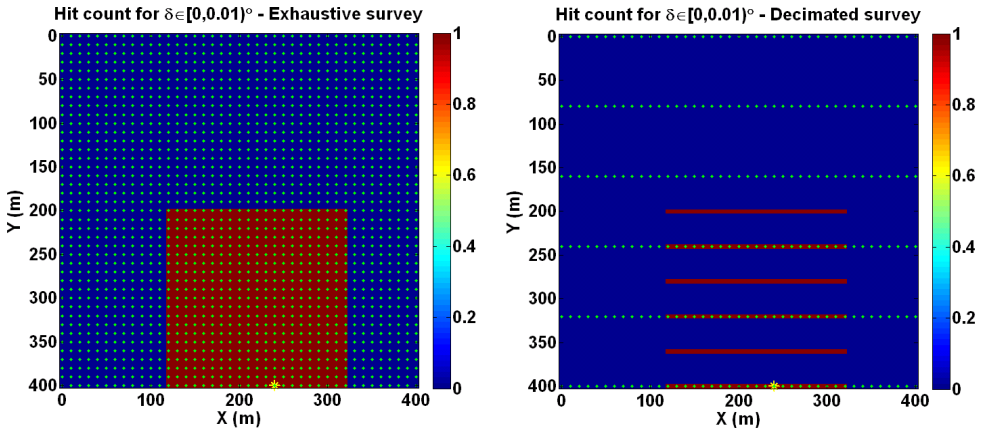


Figure 4.6: Hit count maps for delta dip angles between 0 and 0.01 degrees for a shot located at x=240m, y=400m (position indicated by the yellow star), from the exhaustive dataset (left) and from the decimated dataset (right). Receiver locations for both datasets are indicated by green dots. These essentially zero delta dip hit count maps are identical to common-midpoint fold maps for the shots.

Figure 4.7 shows the hit count maps for the other six delta bins, for the same shot from the exhaustive and decimated surveys. The delta weights used in prestack migration would come from the combination of similar hit count maps for all the shots in each survey. The delta hit count maps in Figure 4.7 are reminiscent of work done on illumination by Margrave (2005) in a study that attempted to reduce footprint by means of illumination compensation in phase-shift migration. This observation suggests that these delta weights are a type of illumination compensation applied to Kirchhoff shot-record migration. The delta hit count maps in Figure 4.6 and Figure 4.7 show a lack of small delta angles for image points between shot-receiver line midpoints in the decimated case. The delta-ratio weights would attempt to compensate for this.

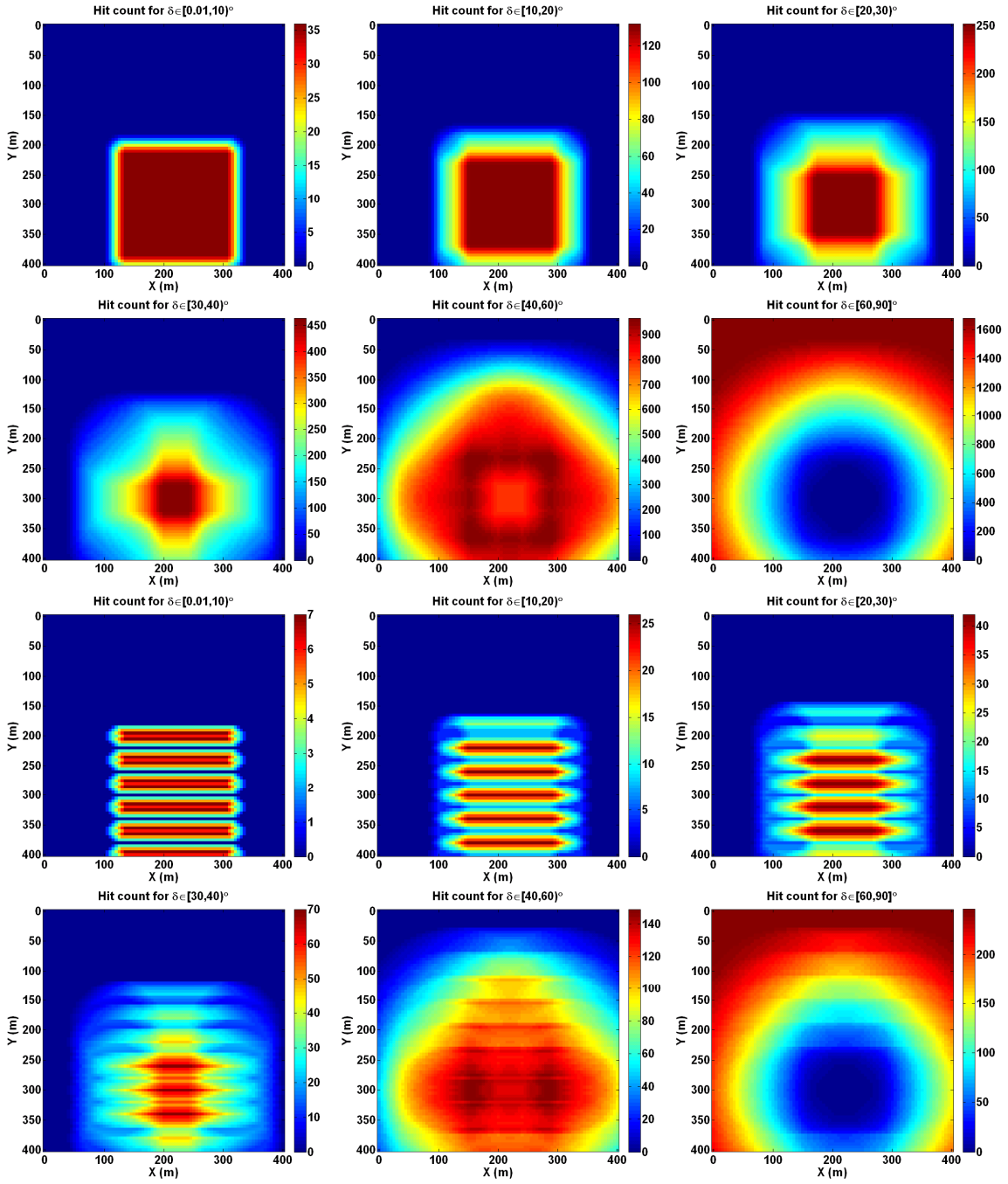


Figure 4.7: Hit count maps for non-zero delta dip angles for a shot located at x=240m, y=400m, from the exhaustive dataset (top six panels) and from the decimated dataset (bottom six panels). The six delta dip bins were [0.01, 10), [10, 20), [20, 30), [30, 40), [40, 60), and [60, 90] degrees.

4.2.4 Implementation of weights

Previously introduced in Chapter 3, prestack Kirchhoff migration is simply a weighted sum of traveltime-corrected data at each image point. The shot-record migration weights prescribed by Bleistein et al. (2001) were included in the Kirchhoff migration algorithm used in this study, as described in Section 3.2.3. However, to compensate for the delta angle sampling irregularities, an additional weight is introduced to be applied to each trace as it is summed at the image point. The weights are pre-calculated by determining the hit counts in defined delta angle bins on the imaging hemisphere. The weights may be pre-calculated since they are just based on the collection of source and receiver coordinates in the survey. As mentioned above, two types of weights are considered: delta-fold weights and delta-ratio weights. The delta-fold weight for a given trace can be written as

$$W_k\left(\underline{x}\right) = 1/n\left(\underline{x}, \delta_k\right), \tag{3.18}$$

where $n\left(\underline{x}, \delta_k\right)$ is the hit count in bin δ_k for the image point at position $\left(\underline{x}\right)$. In this way, delta-fold weights cause all delta bins to contribute equally to the sum at the image point. The delta-fold weights are only a function of the decimated survey geometry. In contrast, delta-ratio weights involve hit counts from both the decimated and exhaustive surveys. The delta-ratio weight for a trace is

$$W_k\left(\underline{x}\right) = n_{exh}\left(\underline{x}, \delta_k\right)/n\left(\underline{x}, \delta_k\right), \tag{3.19}$$

where $n\left(\underline{x}, \delta_k\right)$ is the hit count in bin δ_k for the image point at $\left(\underline{x}\right)$ in the decimated survey, and $n_{exh}\left(\underline{x}, \delta_k\right)$ is the same, but for the exhaustive survey. The delta-ratio weights, instead of making the contributions from all delta bins equal, makes the

contributions from each delta bin equal to what it would have been in the exhaustive survey. Once calculated, the delta-fold or ratio weights are implemented in the prestack shot-record migration sum according to

$$\mathrm{Im}\left(\underline{x}\right) = \sum\nolimits_{j\ shots}\left[\sum\nolimits_{k\ bins}\left(W_k\left(\underline{x}\right)*\varphi_j\left(\underline{x},\delta_k\right)\right)\right], \qquad (3.20)$$

where $\mathrm{Im}\left(\underline{x}\right)$ is the migrated image at the image point at $\left(\underline{x}\right)$ and $\varphi_j\left(\underline{x},\delta_k\right)$ is the j^{th} migrated shot record, limited to those traces whose delta angles fall in bin δ_k. In practice, $\varphi_j\left(\underline{x},\delta_k\right)$ are produced by migrating each shot record into delta-limited output volumes.

4.3 Application in 2D

The delta weighting technique was applied to the same 2D footprint study shown in Chapter 3. Figure 4.8 is a repeat of the results shown in Chapter 3 where delta weights were not used, to serve as a comparison for the results produced with the delta weighting methods. Figure 4.9 shows the results from prestack migration of the same six datasets, with delta-ratio weights implemented when migrated traces were stacked together. Equal width delta dip bins of 5 degrees were used, with a bin centred on zero delta and bins distributed symmetrically for positive and negative deltas. The image from the exhaustive survey is identical in Figure 4.9 to what it is in Figure 4.8. This is because the ratio weights for the exhaustive dataset are just one for all delta angles, as shown in Figure 4.5. The images from the five decimated datasets have changed, though. The residual migration wavefronts that form the footprint artefacts in Figure 4.8 have become less pronounced in Figure 4.9. This is particularly apparent for the 50m shot spacing in

d) and the 100m shot spacing in e). The image from the 200m shot spacing shows a reduction of the wavefronts, but it does show some degree of horizontal striping, which is likely related to the binning of the delta angles. The images of the highly decimated datasets have not been improved to the point where they are identical to the image from the exhaustive dataset, but they are an improvement over the same decimated surveys migrated without using the delta weights. Also, the image of the reverse polarity anomaly and the rest of the flat reflector have remained similar to the case without the delta weights, so the image of the target has not been degraded by application of this weighting scheme.

Figure 4.10 shows the same six prestack migrations using delta-fold weights instead of delta-ratio weights. Unlike in the case of delta-ratio weights, the image of the exhaustive dataset using delta-fold weights is not identical to the case where no delta weights were used (Figure 4.8). Figure 4.10 shows that the fold weights cause an enhancement of artefacts from the edge of the surveys. However, the fold weights have helped compensate for the limited aperture of the surveys. Amplitudes decay at the edges of the images in Figure 4.9, while the amplitudes remain more constant towards the edges in Figure 4.10. This benefit, though, came in association with the enhancement of edge artefacts. Possibly, these artefacts at the edges of the survey could be reduced by tapering before migration, in the same way that poststack migration edge artefacts are avoided. However, the wavefronts from the edges of the images do not appear to be the only wavefronts remaining in the images from the decimated datasets. The fold weights do not appear to reduce the presence of the wavefronts in the same way as the ratio weights do. Figure 4.10 also shows the same horizontal striping as was apparent in the

most severe decimations in Figure 4.9. Figure 4.10 helps to show the connection between the horizontal stripes and the delta binning; the way in which the wavefronts from the edges of the survey are segmented is similar to the way the migration impulse response in Figure 4.3 was divided into delta bins. A different way of binning delta, as opposed to this boxcar method, may produce less of this type of horizontal striping. Figure 4.11 shows a detailed comparison between the prestack migrations without delta weights and with the two types of delta weights for the 50m decimation and 100m decimation.

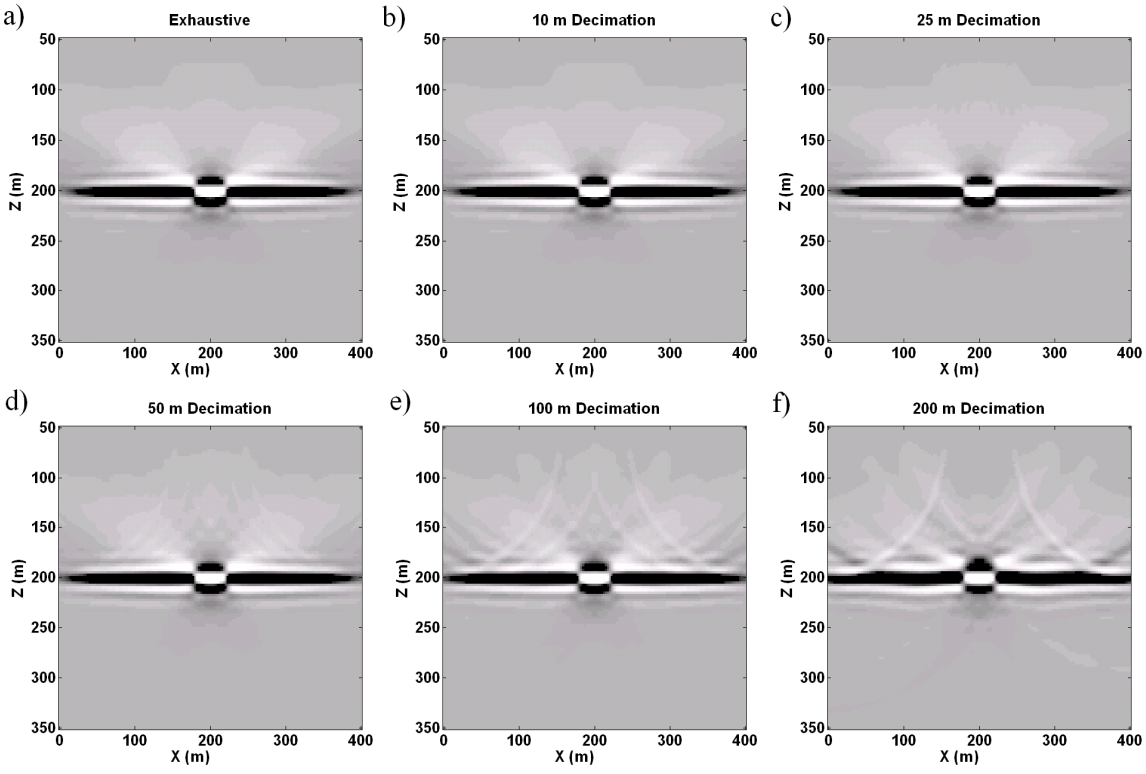


Figure 4.8: Repeat display of images produced from stacking migrated shot records from the 2D exhaustive dataset and the five 2D decimated datasets, using the prestack migration method from Chapter 3.

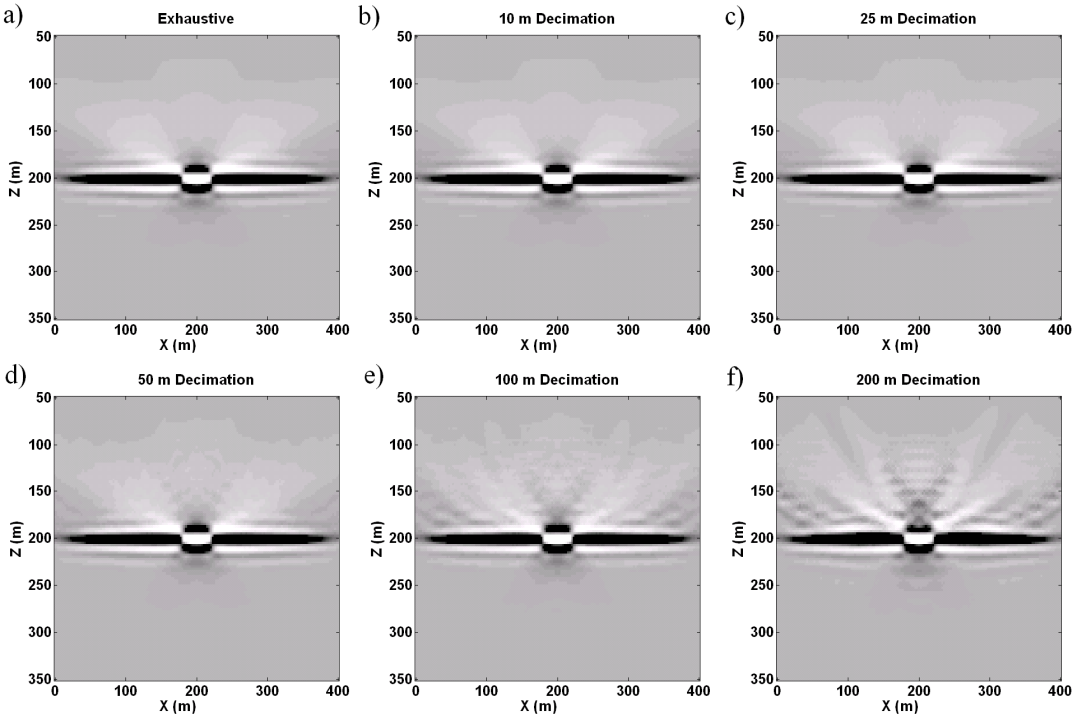


Figure 4.9: Images produced from stacking migrated shot records from the exhaustive dataset and the five decimated datasets. Similar to Figure 4.8 except here delta-ratio weights were applied when migrated traces were stacked. Compared to Figure 4.8, residual migration wavefronts are less pronounced.

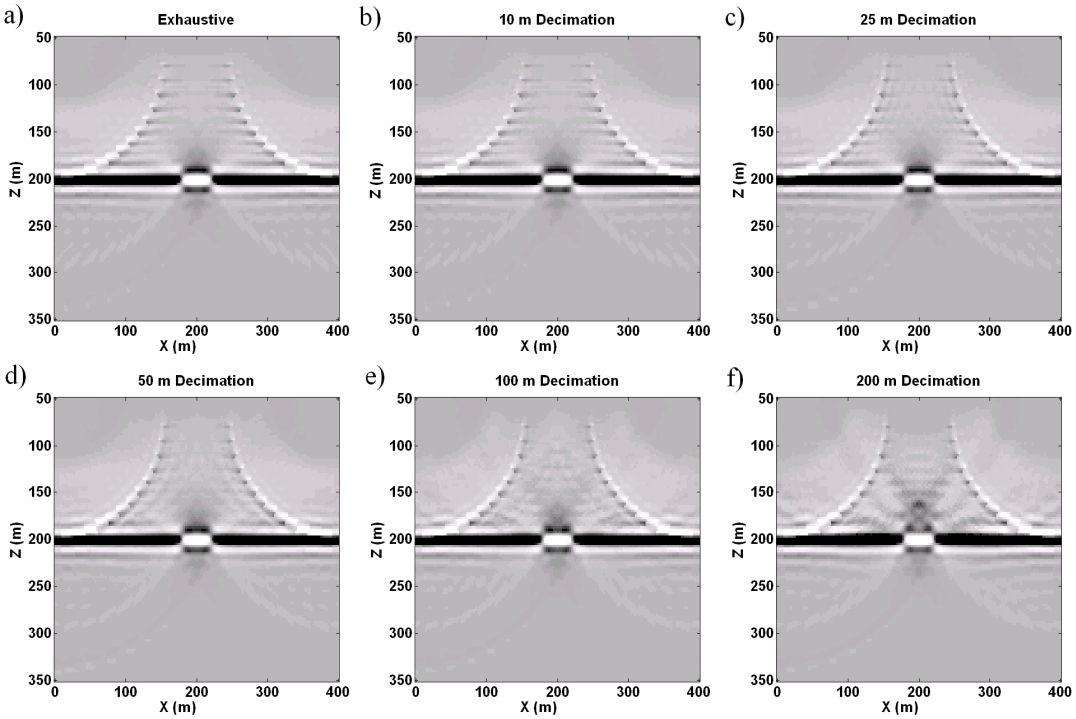


Figure 4.10: Same as Figure 4.9 except delta-fold weights were used instead of delta-ratio weights. Fold weights do not appear to be as effective as ratio weights in reducing footprint, though they do compensate for limited aperture more effectively than the ratio weights.

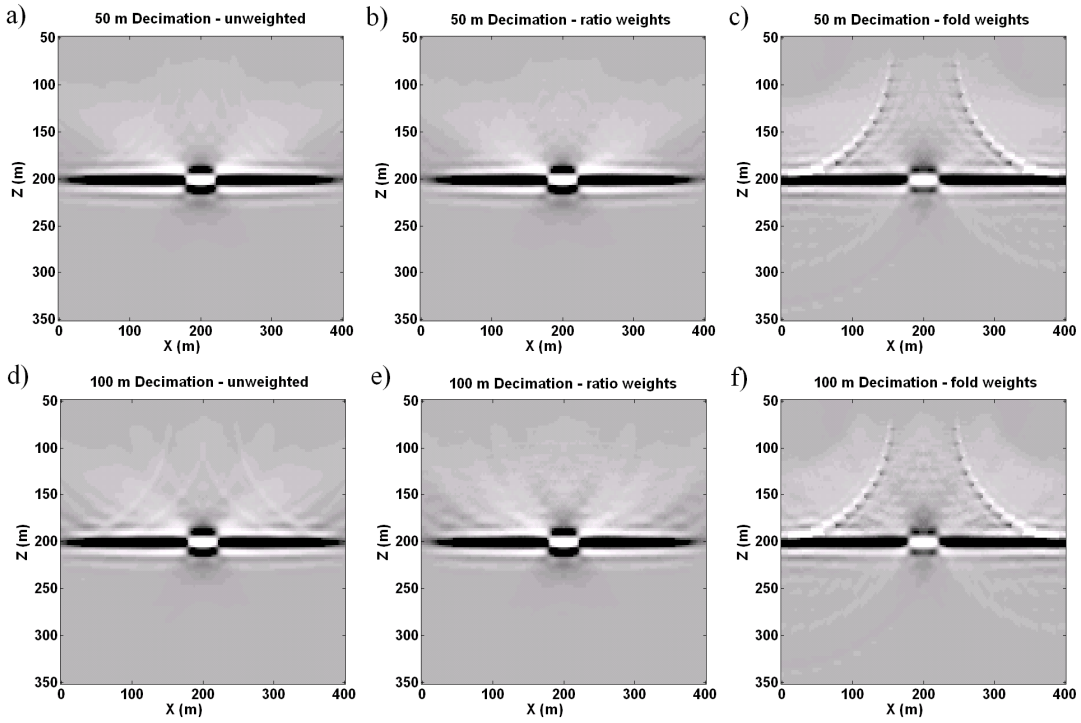


Figure 4.11: Detailed comparison of images produced without delta weights (left), with delta-ratio weights (middle), and with delta-fold weights (right), for the 50m decimated dataset (top row) and the 100m decimated dataset (bottom row).

Since binning of delta angles is an integral part of the weighting method, altering the bin width was performed to assess the impact of this binning. In this 2D investigation, bins with irregular widths were not explored; this could be the subject of future work. Figure 4.12 shows the results from using 1 degree bins for the delta-ratio weights, compared to Figure 4.9 which involved using 5 degree bins. Figure 4.13 shows results using 15 degree bins. Figure 4.14 shows a detailed bin width comparison for the 50m and 100m decimated datasets. These figures suggest that the bin width does have a significant impact on the effectiveness of the delta-ratio weights. Large bins do not seem to reduce the footprint artefacts as effectively, as they are not able to capture the detailed changes in hit counts as a function of delta angle. However, very small bins may make

the weights too irregular with lateral position of the image point, resulting in some chatter in the image. This is especially apparent in the image of the 200m decimated dataset using 1 degree bins. There may be a trade-off between amount of decimation and bin width. Highly decimated datasets may benefit from larger bins, while less decimated datasets may show the most improvement with smaller bins. Figure 4.13 also shows that the horizontal striping is indeed related to the delta binning, since on the image from the 200m decimation the horizontal stripes are still noticeable but are at a larger separation than when the smaller delta bins were used. The 1 degree bins are so small that horizontal stripes do not seem to be present.

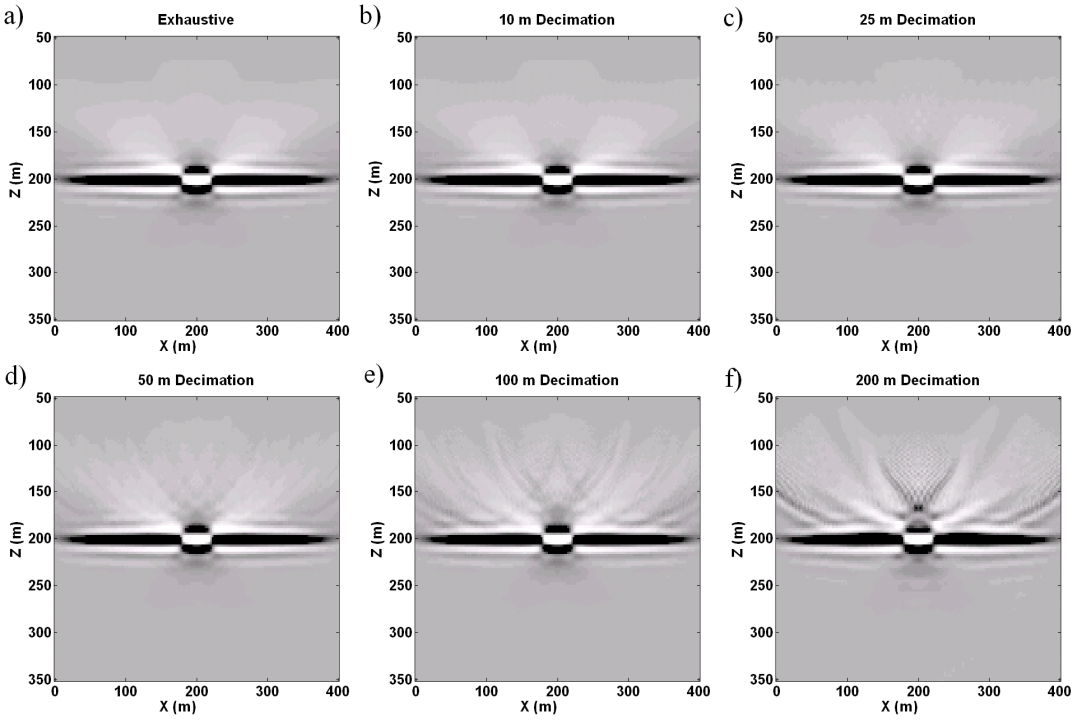


Figure 4.12: Same as Figure 4.9 except 1 degree delta bins were used instead of 5 degree bins for calculating delta-ratio weights.

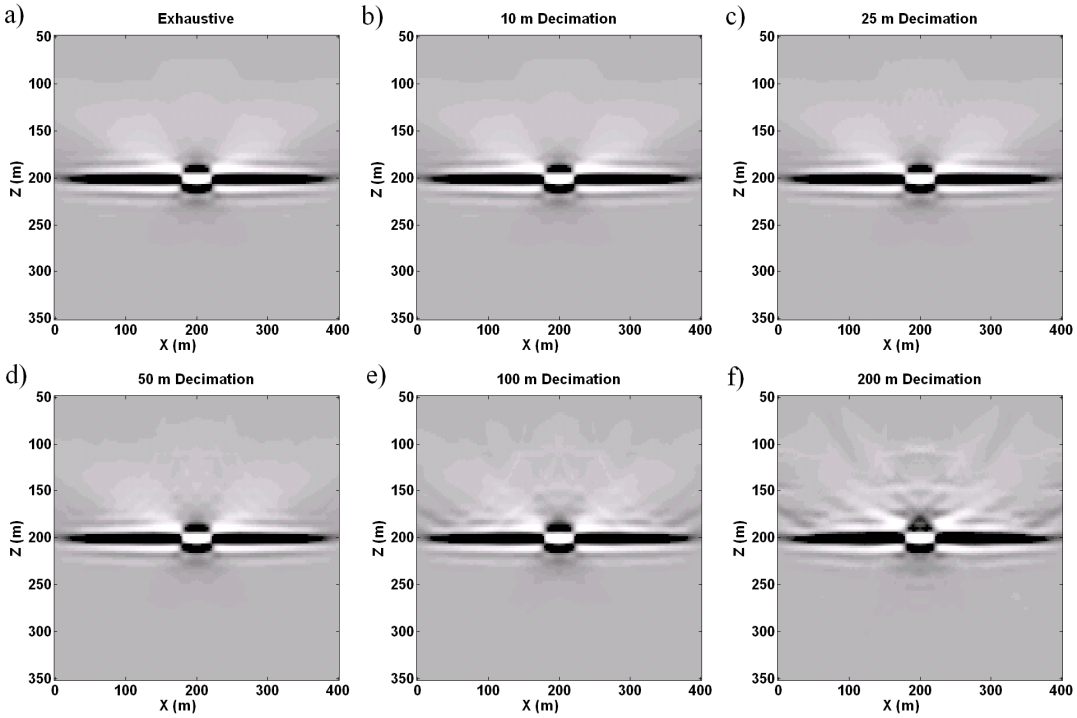


Figure 4.13: Same as Figure 4.9 except 15 degree delta bins were used instead of 5 degree bins for calculating delta-ratio weights.

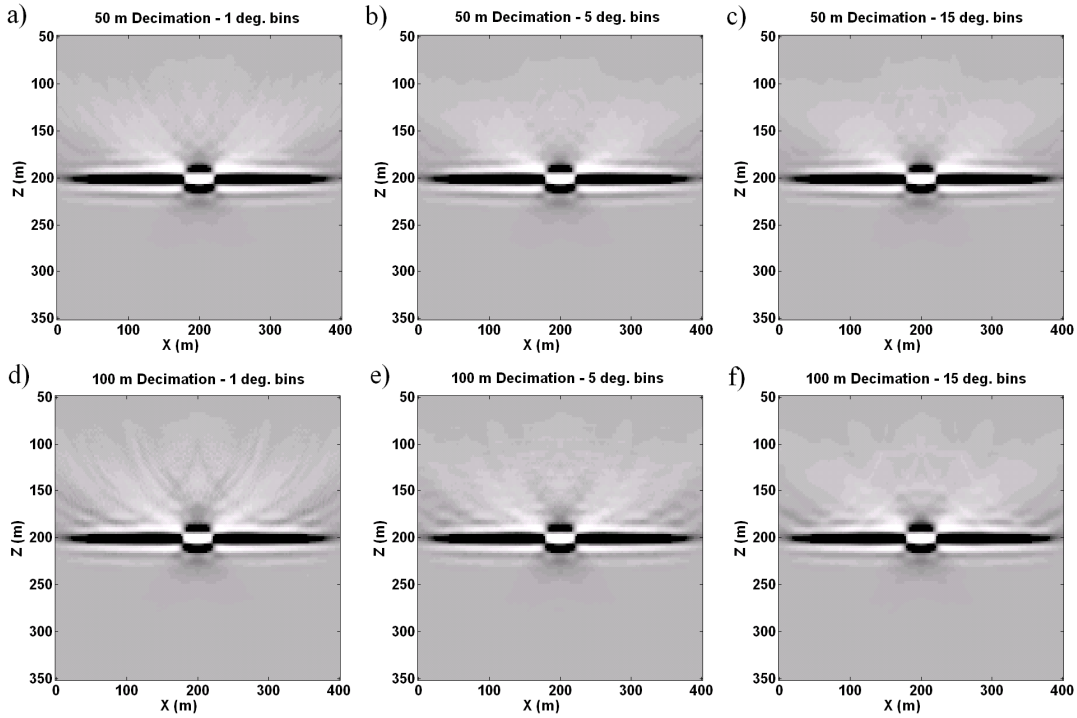


Figure 4.14: Detailed comparison of using different delta bin widths for calculation of delta-ratio weights for the 50m decimated dataset (top row) and the 100m decimated dataset (bottom row). The three different bin widths used were 1 degree (left), 5 degrees (middle), and 15 degrees (right).

As a last comparison using 2D delta weights, the effect of ignoring the azimuth of delta was examined. In other words, binning of the absolute value of delta, instead of signed delta, was performed. Figure 4.15 shows the results of using the absolute value of delta for the delta-ratio weight computations. While the residual migration wavefronts have been reduced slightly, they have not been reduced as much as when the sign of delta was considered (Figure 4.9). Figure 4.16 shows the detailed comparison between not using delta weights, and using both signed and unsigned delta weights. Not surprisingly, these results suggest that it is important to consider the sign (in 2D) or equivalently the

azimuth (in 3D) of delta angles when implementing this type of illumination compensation.

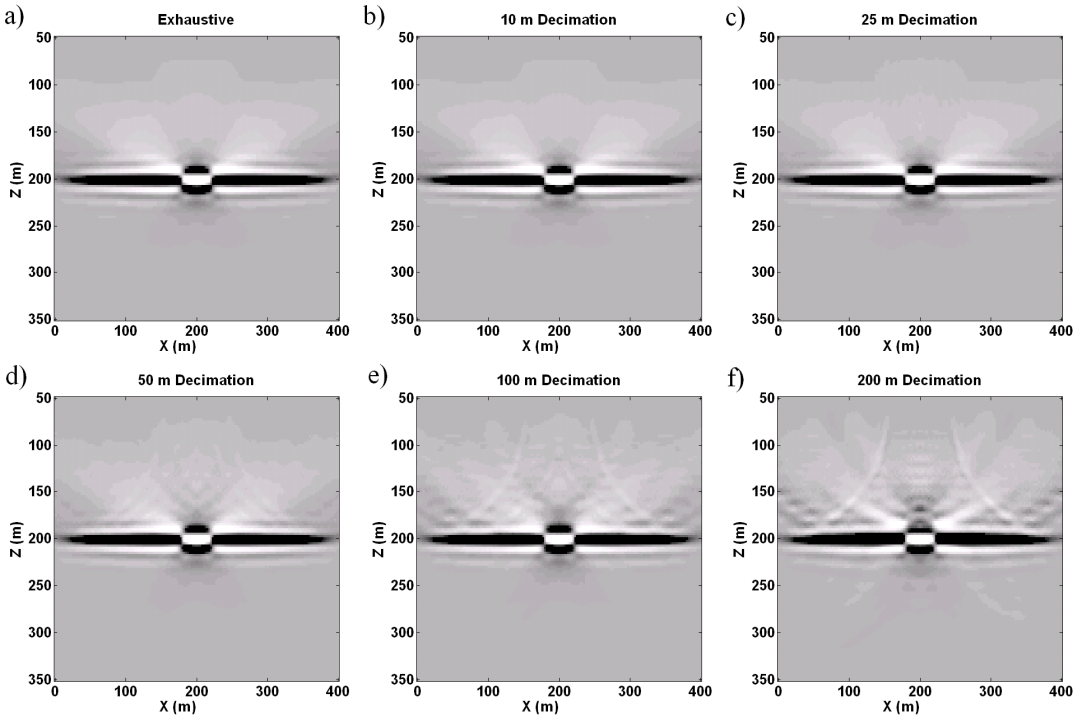


Figure 4.15: Similar to Figure 4.9 except the absolute value of delta was used in binning instead of signed delta. This simulates not considering the azimuth of the delta angle when computing the delta-ratio weights.

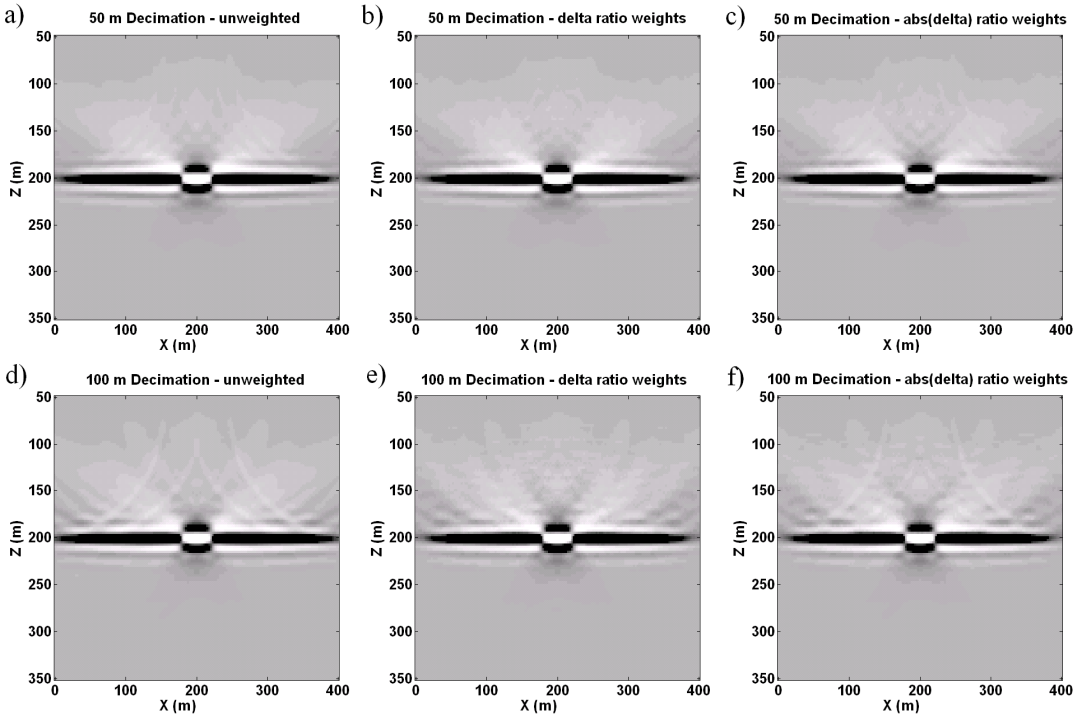


Figure 4.16: Detailed comparison of images produced without delta weights (left), with signed delta-ratio weights (middle), and with absolute value of delta-ratio weights (right), for the 50m decimated dataset (top row) and the 100m decimated dataset (bottom row).

4.4 Application in 3D

Figure 4.17 reproduces the shot-record migrations of the exhaustive and decimated datasets from Chapter 3. As in the 2D case, the delta weighting methods were applied to the decimated dataset in an attempt to reduce the footprint artefacts. Figure 4.18 shows the results from prestack migrations of the 3D decimated dataset using delta-ratio weights with different choices of delta binning. In all cases, the delta dip binning was in 5 degree bins, which was the optimal bin width in the 2D simulations from Section 4.3. However, the azimuthal binning varied; from top to bottom in the figure the binning involved 1 azimuth bin (i.e. no azimuthal binning), 4 azimuth bins, 8 azimuth

bins, and 16 azimuth bins. Compared to Figure 4.17, the delta-ratio weighted migrations show fewer footprint artefacts than the migrations without delta weights. This is especially apparent on the 100m and 180m deep featureless reflectors. At the channel level, the delta-ratio weight images show that the weighting scheme preserves the resolution of the channel edges and point diffractors. Comparing the different azimuth binnings, there is a significant improvement in the images moving from 1 azimuth bin to 8 azimuth bins. However, using 16 azimuth bins does not produce much of an improvement over 8 azimuth bins. The specific observation of the optimal number of azimuth bins could of course change with a different survey aperture and decimation. However, the more general observation here is similar to the 2D simulations from the previous section, where considering the sign of delta (equivalent to keeping track of azimuth) was more effective than considering only the absolute value of delta. The 3D results are also consistent with the findings in 2D that there was an optimal bin size; finer binning generally produced better results. However, at a certain point, the bins were too small to be effective. In 3D, the 16 azimuth bins are small enough to not yield any considerable improvement over 8 azimuth bins, but are not fine enough to produce degradation of the image, as was seen with the very fine delta dip binning in 2D.

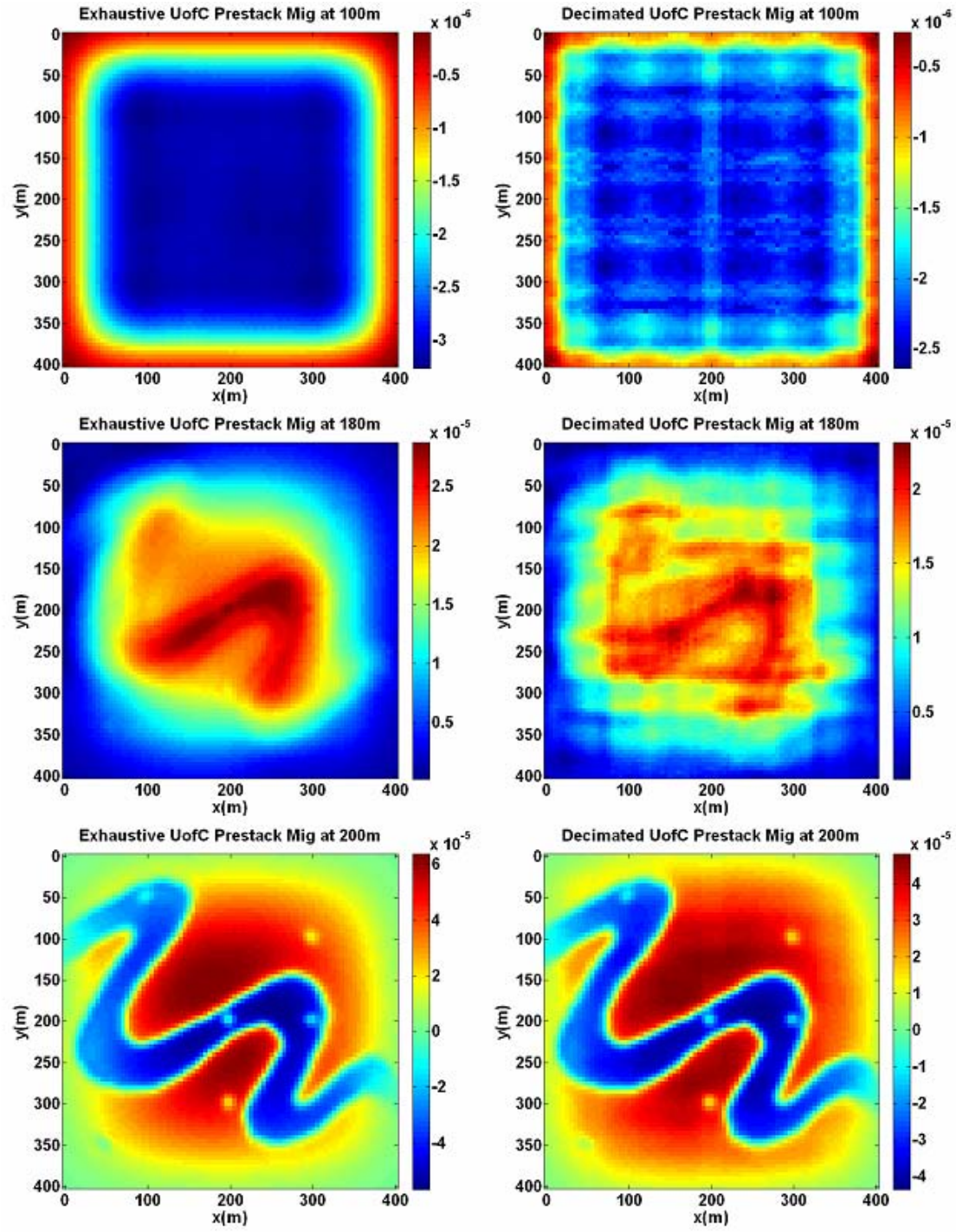


Figure 4.17: Repeat display of depth slices from UofC prestack migrations for the exhaustive and decimated datasets, from Chapter 3.

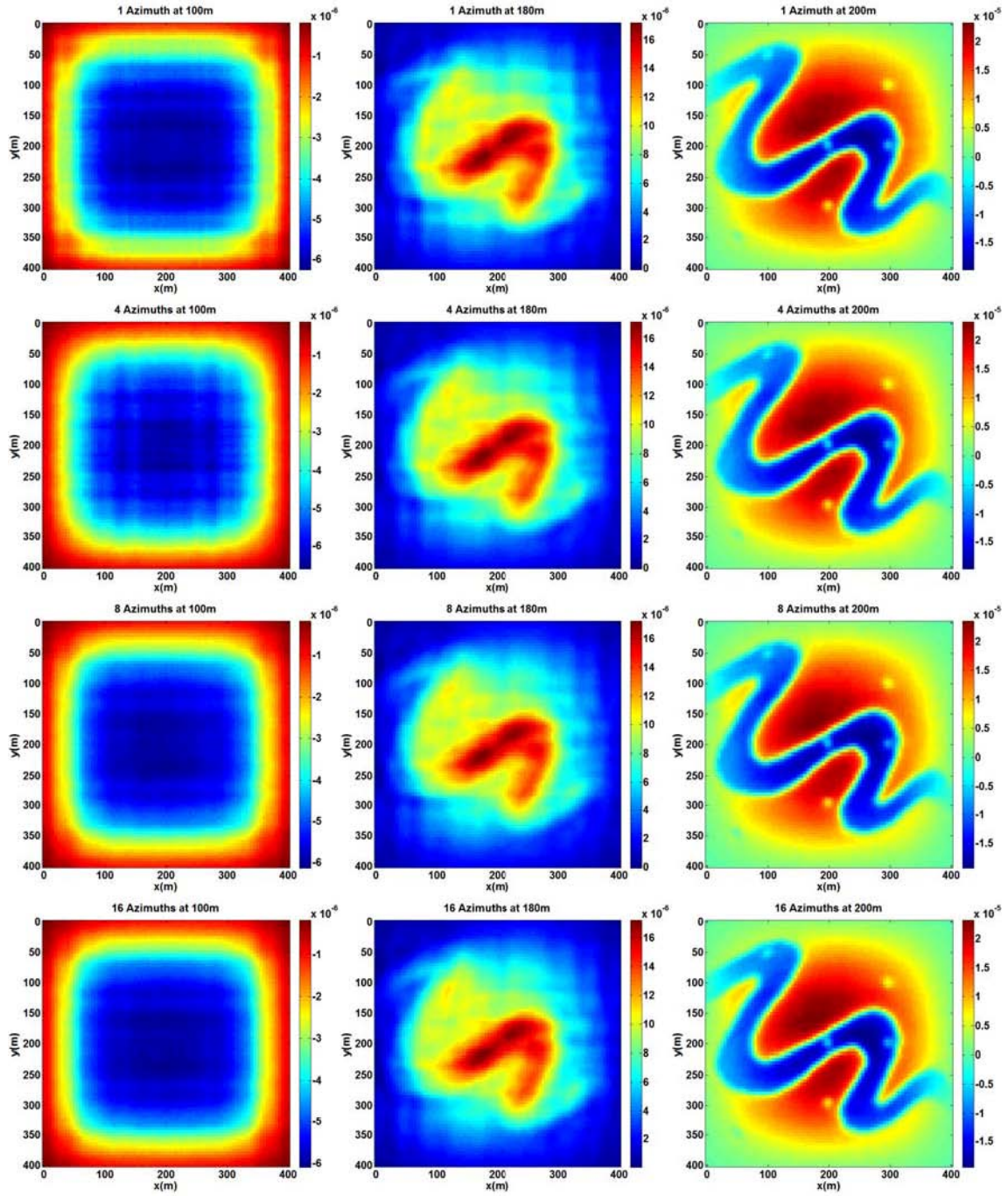


Figure 4.18: Depth slices from delta-ratio weighted prestack migrated images at the three reflectors: 100m featureless (left), 180m featureless (middle), and 200m channel (right). From top to bottom, the azimuthal binning involved 1, 4, 8, and 16 azimuth bins.

Figure 4.19 shows depth slices from the prestack migration using the delta-fold weights for the decimated dataset and the same binning that was used to create the 8 azimuth bins delta-ratio weight image from Figure 4.18. As observed using the delta-fold weights in 2D, the weights are very successful in removing the aperture imprint of the survey; however, they produce edge artefacts which appear as lineations on the two shallow slices in Figure 4.19. The 100m deep featureless reflector also displays some residual internal amplitude variations or footprint. Perhaps of even more significance is something not observed previously in 2D but very apparent in 3D, namely that the delta-fold weights also appear to reduce resolution of the channel edges and especially of the point diffractors, compared to the migrations with no delta weights and those with the delta-ratio weights. As a result, this weighting scheme does not seem to be successful.

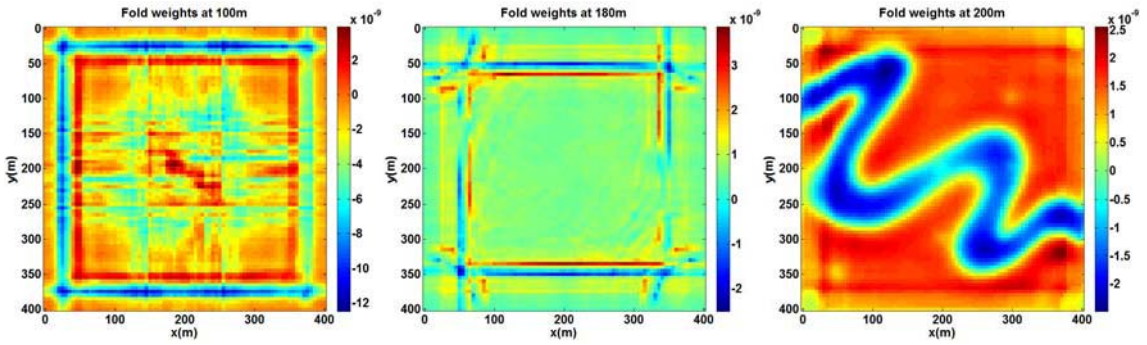


Figure 4.19: Depth slices at 100m, 180m, and 200m from delta-fold weighted prestack migrations of the decimated dataset.

4.5 Comparison to 3D common-offset weighting

Though the 3D delta-ratio weighting scheme does appear to reduce footprint artefacts, the simulations from Chapter 3 demonstrated that industrial common-offset and common-offset-vector migration algorithms were also successful in reducing the

artefacts. So, a comparison was made between the delta-ratio weighting technique and one of these more conventionally used methods. However, the delta-ratio weight shot-record migration algorithm used here does not include any optimizations generally incorporated in industrial algorithms (such as smoothing of weights, borrowing of traces from adjacent bins to fill holes, etc.). As a result, in order to make an objective comparison, a version of a Kirchhoff common-offset-weighted prestack migration was coded in MATLAB, such that it was of comparable sophistication to the shot-record migration. As described in Section 3.4, the method involves computing offset-limited fold volumes, and then pre-weights traces by the offset-limited fold that corresponds to the offset bin into which the trace falls. Because the weights are applied before migration, the migration does not technically need to be performed in the common-offset domain; in fact, in the implementation used here the algorithm is still a shot-record migration. An important parameter in the method is the choice of offset bins. The idea is to have as many offset bins as possible, while still keeping each bin populated at every midpoint, or as close as possible. Here three choices of binning are shown: a single offset bin (which amounts to simply pre-weighting the traces by conventional CMP fold), two offset bins of 0-250m and >250m, and six offset bins of 0-100m, 100-200m, 200-300m, 300-400m, 400-500m, and 500-600m. Figure 4.20 shows the results of these common-offset-weighted migrations. Even though these are likely not optimal choices of binning, the results using six offset bins show the ability of the method to compensate for aperture, still resolve edges very well, and do some internal footprint compensation.

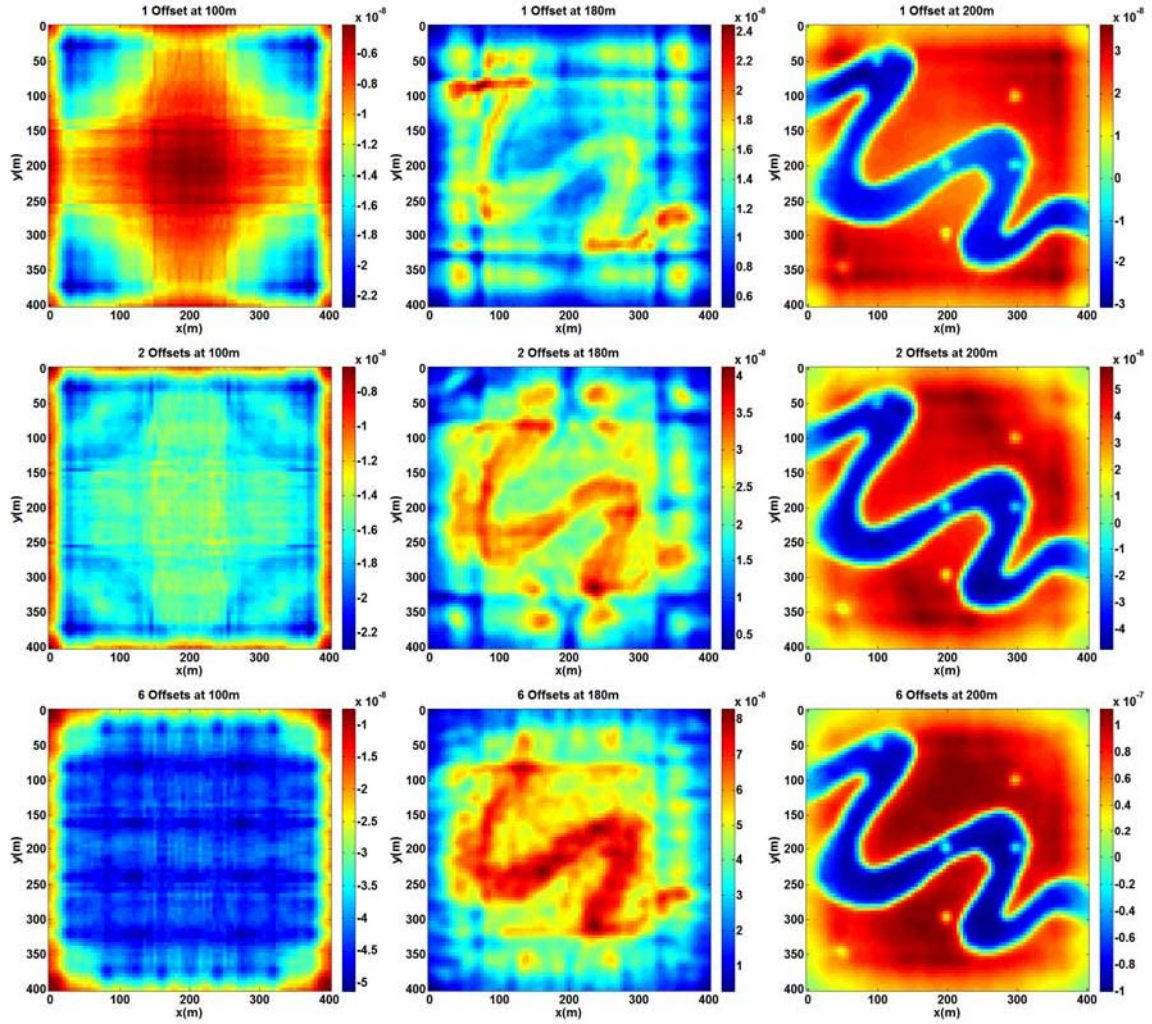


Figure 4.20: Depth slices from common-offset-weighted prestack migrated images at the three reflectors: 100m featureless (left), 180m featureless (middle), and 200m channel (right). From top to bottom, the offset binning involved 1, 2, and 6 offset bins.

While qualitative comparisons are informative, differences in scaling of individual images can be misleading; as a result, it is useful to find a means to quantify the differences between the methods. The best way to do this is to compare the migrated images to the known answer, i.e. the true reflectivity slices (e.g. Figure 3.10 for the channel level). One complication in the case of the delta-ratio weights is that the aperture

imprint of the survey is still quite strong, meaning that those differences will dominate the comparison between migrated result and true reflectivity. In order to be able to compare the delta-ratio method to the other weighting schemes, an attempt was made to remove the aperture imprint on the ratio-weighted slices. The aperture imprint should be a smooth, symmetric amplitude decay away from the centre of the survey area. The approach taken was to create an estimate of the aperture imprint by severely smoothing the absolute value of the migrated slice via 2D convolution with a boxcar. Then, the migrated slice was divided by this aperture estimate, to produce an aperture-removed image. Figure 4.21 shows the aperture imprint estimate and the results of its removal for the 8 azimuth bin delta-ratio weight migrations at the three reflectors. By removing the aperture imprint, the pure internal footprint artefacts are isolated and it allows for the direct comparison of the three weighting schemes. Figure 4.22 shows the difference between the true reflectivity and the migrated images using delta-ratio weights, delta-fold weights, and common-offset weights, for the 100m and 180m deep featureless reflectors as well as the 200m deep channel reflector. The differences are expressed in percent, after a bulk scaling of the mean of each migrated slice to match the mean amplitude of the reflectivity slice. Aperture removal was performed on the delta-ratio and common-offset slices. The delta-ratio and delta-fold images had 8 azimuth bins; the common-offset images had 6 offset bins. Examination of the channel reflector shows the ability of each method to resolve edges and points, whereas the featureless reflectors reveal the severity of the internal periodic amplitude variations. From these results, the delta-ratio weight method appears to produce the images with the least residual footprint compared to the migration without additional weights and the two other weighting schemes.

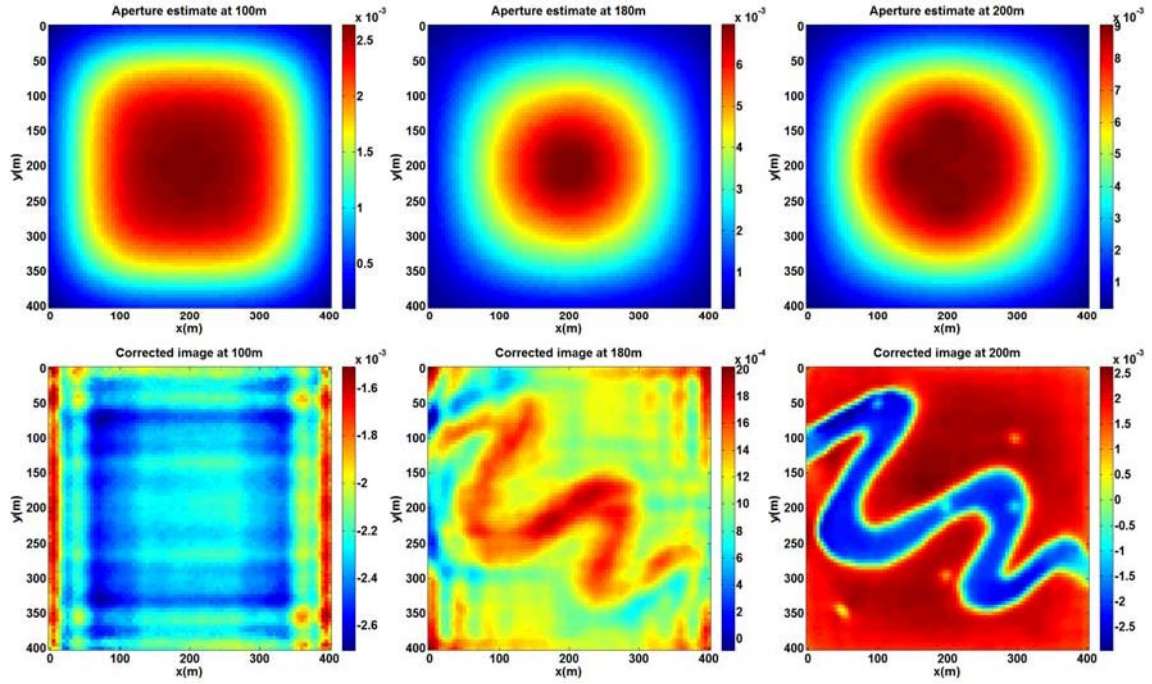


Figure 4.21: Aperture estimate (top) and aperture-removed migrated depth slices (bottom) at 100m, 180m, and 200m for the delta-ratio weighted prestack migration of the decimated dataset with 8 azimuth bins.

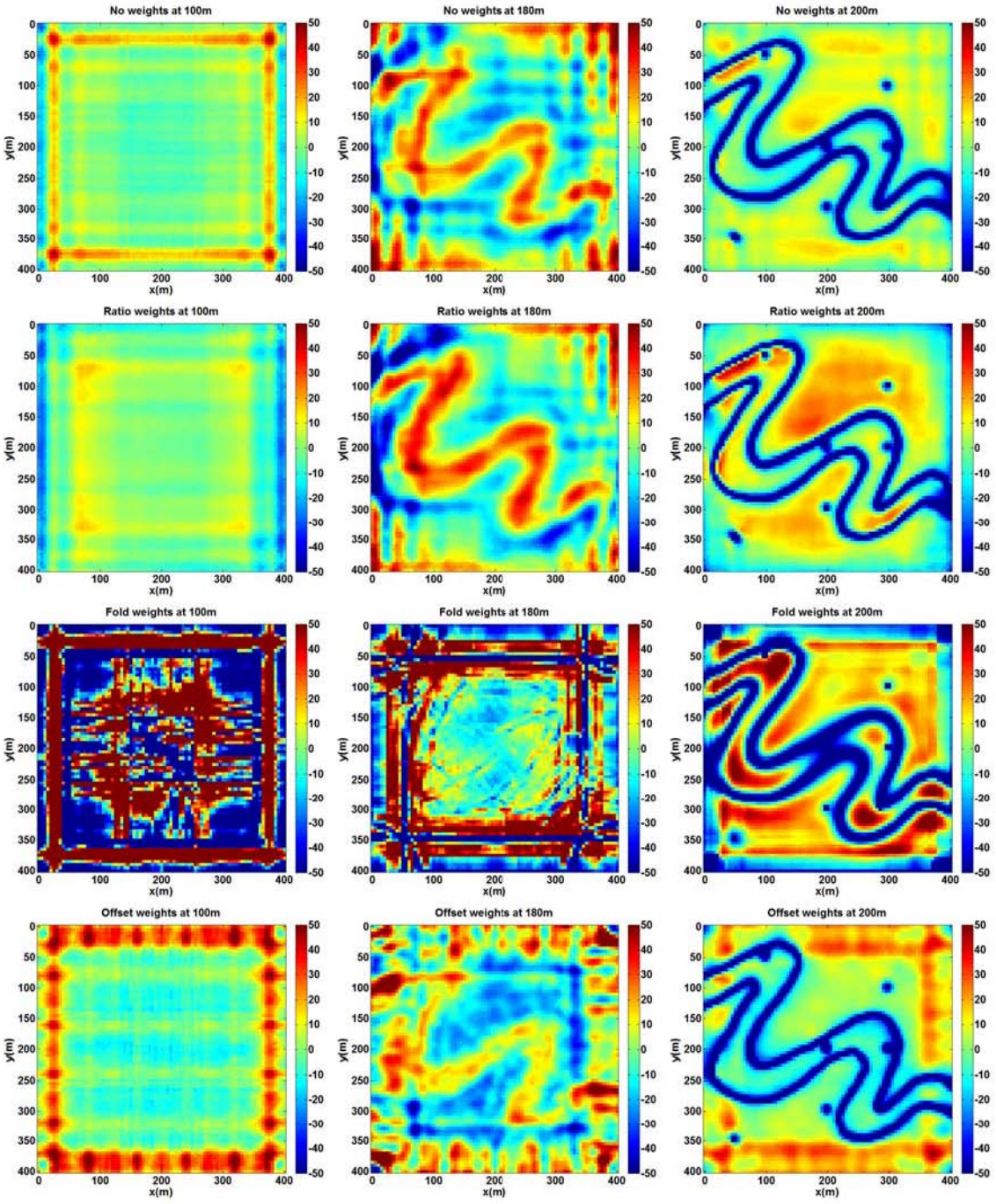


Figure 4.22: Percent difference between migrated depth slices and the true reflectivity at 100m (left), 180m (middle), and 200m (right). Top to bottom: no weights (reference), delta-ratio weights, delta-fold weights, and common-offset weights.

4.6 Application to additional 3D decimations

Since the severity of the footprint in a migrated image is a function of not only the migration algorithm but also the survey geometry, an examination of the performance of the delta-ratio weighting with a different sampling decimation was conducted. Figure 4.23 shows two alternate decimated surveys, which are identical to the original decimated survey from Figure 2.27b except that they contain a hole in the shot coverage, as might occur in the presence of some obstacle in the field. One version (Figure 4.23a) involves shot lines that end abruptly at the obstacle, while the other (Figure 4.23b) has shot lines that smoothly bend around the obstacle. These surveys are of course not the only possibility for another survey geometry, but they do serve as a test of the weighting scheme in a situation with slightly more irregular sampling, rather than just sparse but still regular sampling.

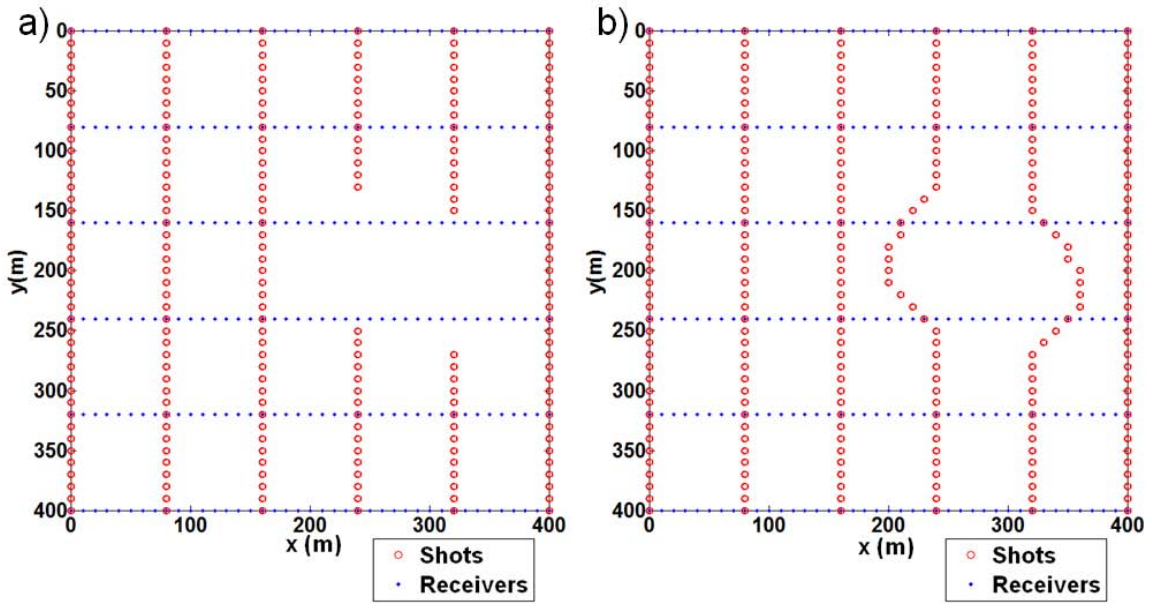


Figure 4.23: Geometry of decimated surveys with a hole introduced by removing shots (a) and by moving shots (b).

Figure 4.24 and Figure 4.25 show the results from the prestack migration of these new decimated datasets, for the case without weights (comparable to Figure 4.17), and the case with the three different weighting schemes (comparable to Figure 4.18, Figure 4.19, and Figure 4.20). Figure 4.26 and Figure 4.27 show the percent difference plots comparing the migrations to the true reflectivity (comparable to Figure 4.22). The migrated images now display the effect of a hole in the survey, in addition to the effect of a regular decimation. The hole affects the amplitudes most dramatically on the 100m featureless reflector. At the channel level, the hole seems most apparent in the common-offset images. For these decimations, the delta-ratio weights again appear to improve the images of the 100m and 180m deep featureless reflectors, and they preserve resolution of the channel edges and point diffractors. Comparing the survey with removed shots to the one with moved shots shows that the second method produces much better images with all of the migration algorithms. The delta-ratio weights outperform the common-offset weights for both surveys.

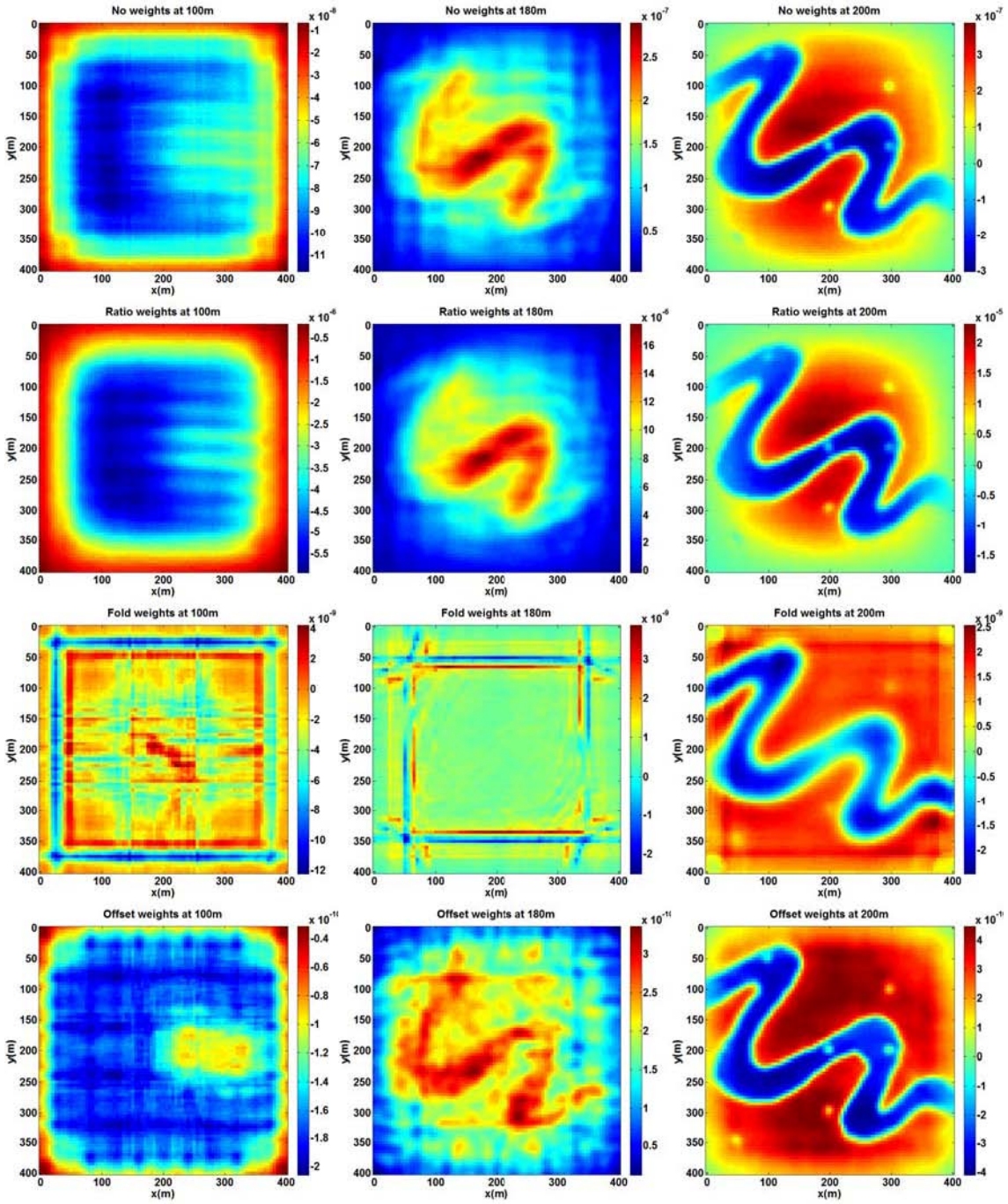


Figure 4.24: Prestack-migrated depth slices at 100m (left), 180m (middle), and 200m (right) for the survey with removed shots. Top to bottom: no weights (reference), delta-ratio weights, delta-fold weights, and common-offset weights.

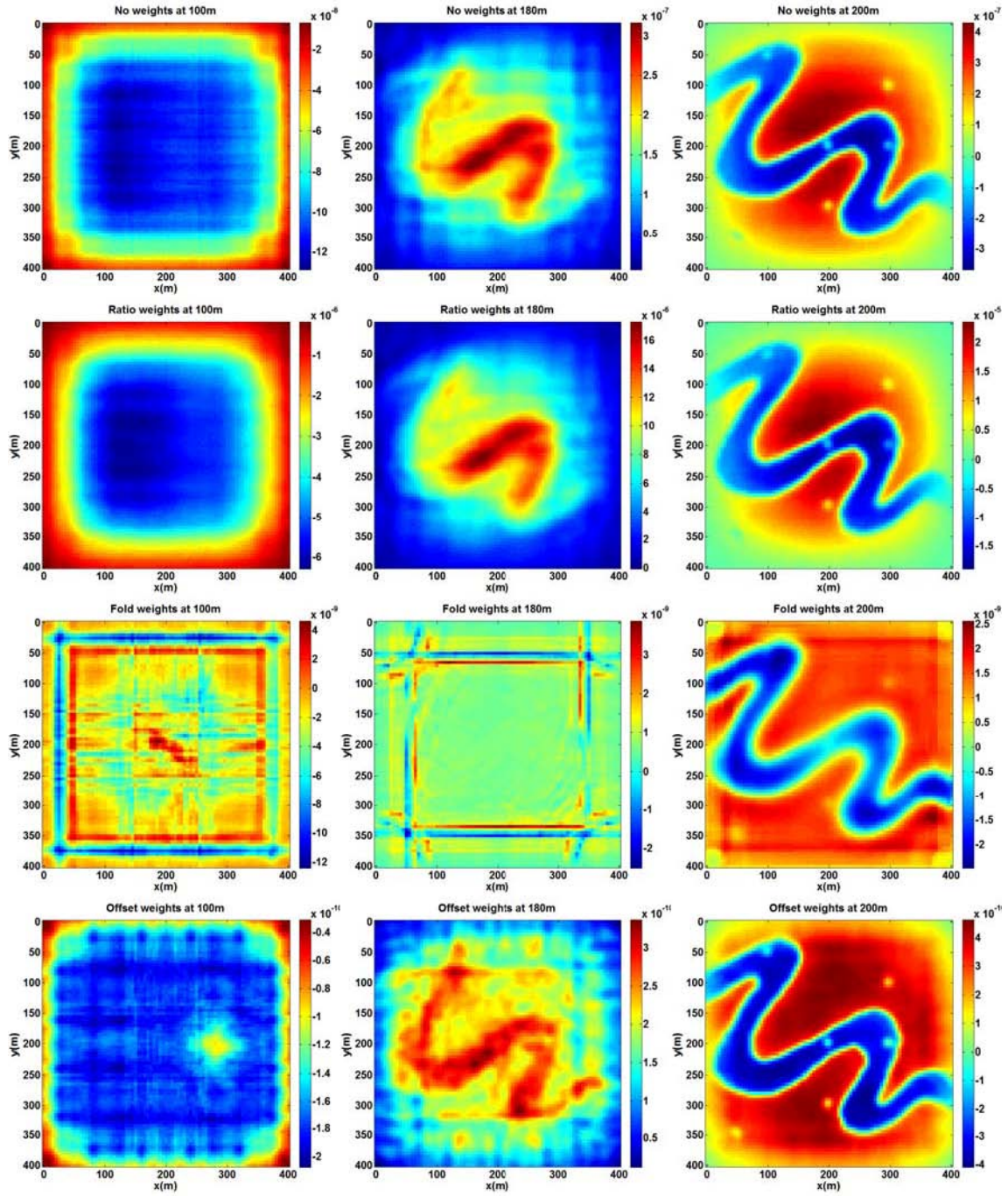


Figure 4.25: Prestack-migrated depth slices at 100m (left), 180m (middle), and 200m (right) for the survey with moved shots. Top to bottom: no weights (reference), delta-ratio weights, delta-fold weights, and common-offset weights.

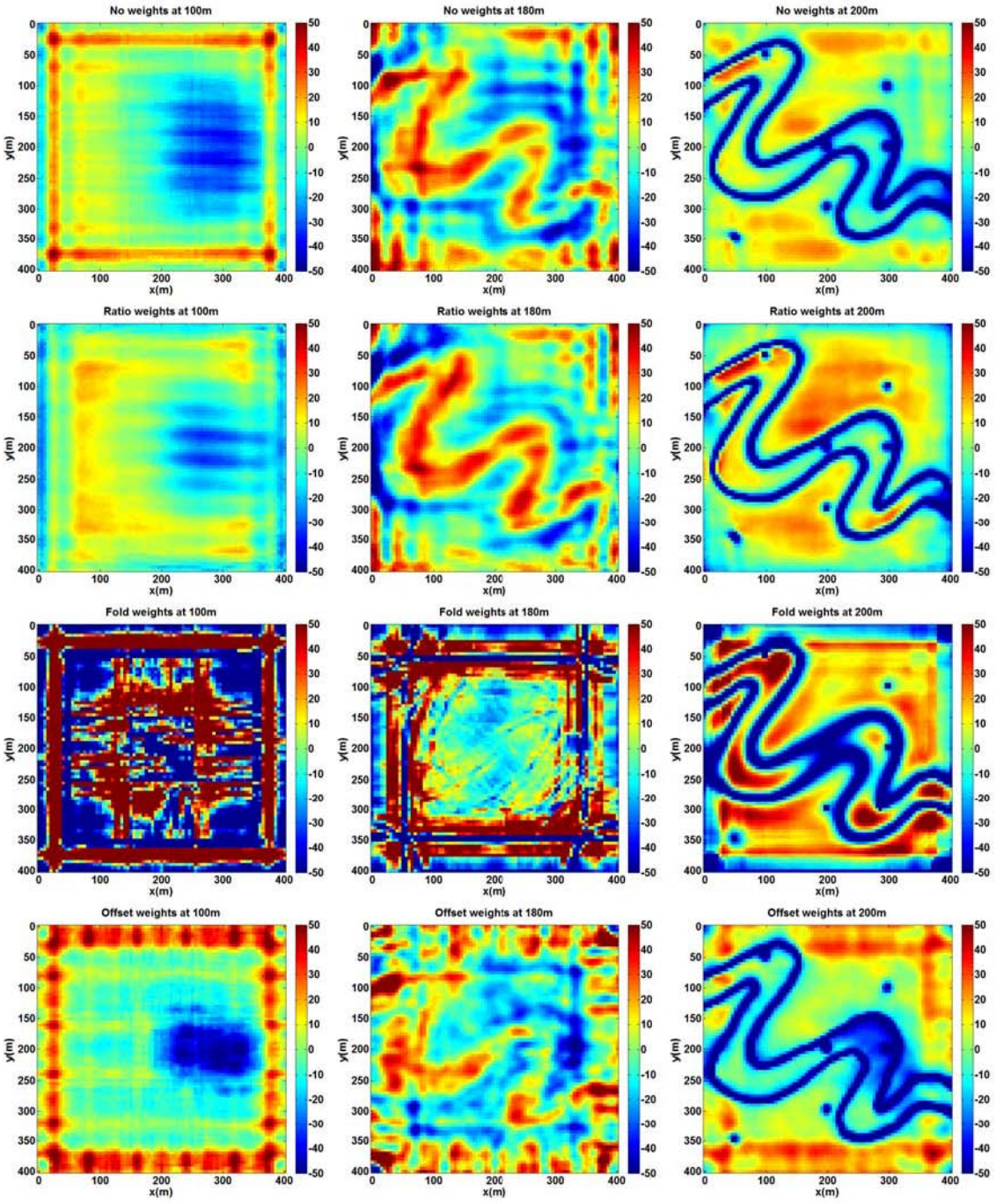


Figure 4.26: Percent difference between migrated depth slices and the true reflectivity at 100m (left), 180m (middle), and 200m (right) for the survey with removed shots. Top to bottom: no weights (reference), delta-ratio weights, delta-fold weights, and common-offset weights.

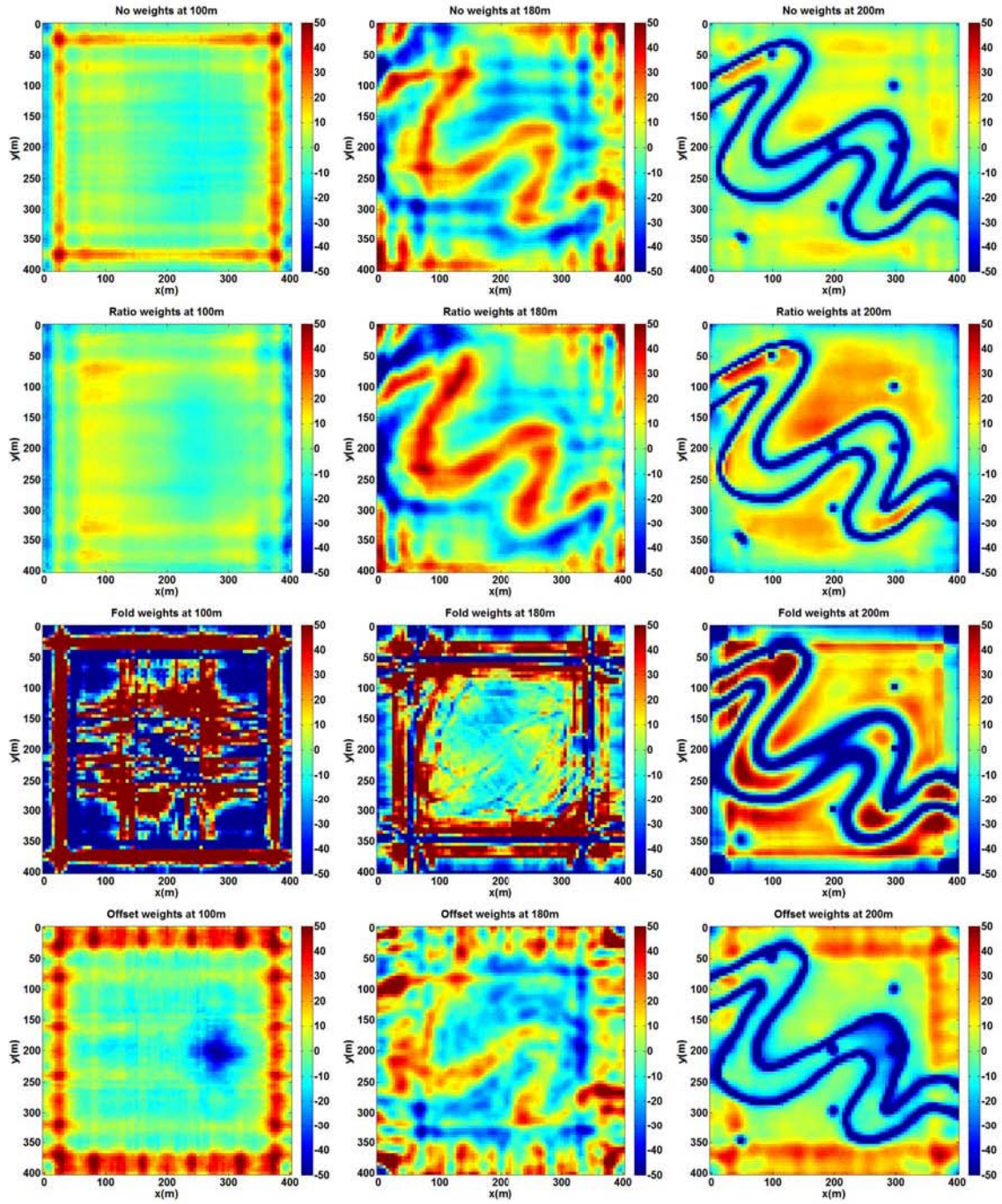


Figure 4.27: Percent difference between migrated depth slices and the true reflectivity at 100m (left), 180m (middle), and 200m (right) for the survey with moved shots. Top to bottom: no weights (reference), delta-ratio weights, delta-fold weights, and common-offset weights.

4.7 Discussion

Applying weights based on the distribution of raypath opening angle bisector directions to attempt to compensate for irregular image point illumination appears to reduce the presence of footprint produced when migrated shot records are stacked. The 2D simulation of decimated datasets shows that the weighting scheme is not a substitute for proper sampling and cannot reproduce the quality of images produced from the exhaustive dataset, but the results do show that this type of compensation provides some benefit. The migrated sections incorporating delta-ratio weights during stacking are an improvement over simple stacking of migrated shots.

An aspect that was not investigated is the manifestation of footprint in common-image gathers and whether this type of weighting would also show a benefit in that context. However, because the ability of delta-ratio weights to produce better migrated images must be due to improved weighting of the individual traces contributing to each stacked trace, it is likely that in a common-image gather, where those individual contributions are displayed, improvement would also be achieved. In this study, however, the aim was simply to produce a final image from stacking migrated traces that exhibits the least footprint. In the shot-record migration used here, this means that the focus is not on producing the best migration of a single shot record, but the best stack of all migrated shots. Since the final image produced will result from stacking many migrated shots it makes sense that any weighting scheme used should have weights that depend on the distribution of shots as well as the distribution of receivers. Perhaps the apparent advantage of common-offset migration methods compared to a shot-record migration in the 3D simulations from Chapter 3 is related to this; common-offset

migrations necessarily incorporate both source and receiver sampling because of the coordinate transform to midpoint and offset. However, if no partial stacking is being done before migration, it should not matter what type of gather is being migrated. Each migrated trace should be able to be weighted appropriately to get the most accurate amplitudes in the final image as possible. The delta weights for any migrated trace are a function of the distribution of all shots and receivers in the survey and are independent of whether the trace was in a shot record or in a common-offset gather.

The idea of these delta hit counts is appealing because the zero delta dip bin is the same as common-midpoint fold for flat reflectors and the concept of dividing by fold when we do stacking is very well established. The non-zero delta hit counts extend the idea of fold to prestack data. The fact that the ratio weights do nothing in the case of the exhaustive survey is also good, since we consider the exhaustive survey to already have ideal sampling. However, it would be beneficial for the weighting scheme to remove the strong aperture effect, which plagues even the exhaustive survey, and fold weights have the ability to do this, while ratio weights do not. Overall, in these simulations, the ratio weights perform better than pure fold weights. This may be related to the fact that we are combining the delta weights applied after migration with Bleistein weights that get applied during the migration.

As shown in the 2D simulations, binning is an important factor in the method. The binning appears to result in some horizontal striping in the images in some cases. It is possible that Gaussian windows in delta instead of boxcar windows would reduce this problem. It is also unclear at this stage whether bins should be equal in size or not; in the 2D simulations the bins used were all regular in size, while the 3D delta hit count maps

involved unequal bins. In 3D the choice of binning is even more complicated than in 2D because bins could be either on a polar grid or a rectangular grid; this is similar to the choice in binning offset in 3D into polar coordinates (offset and azimuth) or rectangular coordinates (inline offset and crossline offset).

In the 3D simulations, delta-ratio weights helped reduce internal footprint artefacts when compared to a migration algorithm that did not include additional weights. The method also performed better than an implementation of a more conventionally used common-offset weighting scheme. It was again observed that delta-ratio weights do not compensate for the aperture imprint of the survey, but it may be possible to use another method for aperture compensation, as was attempted in this study. Or, if delta-ratio weights which involve dividing hit counts from an *aperture-limited* exhaustive survey by decimated hit counts reduce internal footprint but do not compensate for aperture, then perhaps dividing hit counts from an *infinite-aperture* exhaustive survey by decimated hit counts would compensate for aperture while still producing the footprint reduction. In contrast, delta-fold weights and common-offset weights do remove the aperture effect. However, fold weights appear to reduce spatial resolution in the 3D migrated images and overall do not produce good images. Since resolution is achieved in migration by careful weighting of angular contributions at each image point, the delta-fold weights must work against this process, while the delta-ratio weights preserve it.

As shown in the simulations in Chapter 3, common-offset weights are able to produce better images than those shown in this chapter, when implemented in an industrial-strength algorithm. However, the same methods of weight smoothing and borrowing of traces from adjacent bins included in such an algorithm could also be

implemented in a delta weighting algorithm, and would likely result in improvements for that method as well. In addition, both methods could be applied with a different choice of binning, which could also produce improvements. One advantage of the delta-ratio weights over common-offset weights is that the common-offset weights are strictly a midpoint concept, and as such are depth-independent and are limited to flat reflectors. The delta-ratio weights are image-point based, and as such they can vary with depth and can apply to any dip.

The images of the decimated datasets produced by all of the migration algorithms display footprint artefacts. This emphasizes the importance of proper sampling of the seismic wavefield during acquisition, and demonstrates that processing, prestack migration in particular, cannot be relied upon to completely compensate for poor sampling. In the case of a hole in the survey, the survey with smooth variations in shot positions produced better images than the survey with abrupt gaps in the shot lines, though the first case did involve more total shots than the second case, and as such may not be an ideal comparison. Despite the inability of prestack migration to suppress all footprint artefacts induced by the decimated survey geometries, the delta-ratio weights do have a theoretical and intuitive foundation and they produce some improvement in the images, which suggests that future work is warranted.

4.8 Summary

As shown in Chapter 3, when compared to prestack-migrated images of a fully-sampled (“exhaustive”) numerical model seismic dataset, images from decimated (under-sampled) datasets display acquisition footprint artefacts. In this chapter, a weighting

scheme in a Kirchhoff shot-record migration, which partially compensates for irregularities in the angle-dependent illumination of an image point, was described and assessed. The method was applied to the exhaustive and decimated datasets, with the purpose of examining its ability to suppress footprint artefacts. Although the weights were applied in the context of migrating common-source gathers, the weights are dependent on the locations of all shots and receivers in a survey, and are applied to traces during the stacking process after migration; they are therefore not limited to the case of shot-record migrations. The weights are a function of image point location and delta, an angle describing the direction of the vector that bisects the opening angle formed by source-to-image-point and receiver-to-image-point rays. Hit counts at each image point are computed for different delta bins and these are used to compute weights that are applied to delta-limited Kirchhoff migrations. The zero delta dip hit count is identical to traditional common-midpoint fold and collectively these hit counts generalize the fold concept to prestack migration. Though the method does not address footprint related to the aperture of the survey, it does appear to reduce the severity of footprint artefacts consisting of periodic amplitude variations in the interior of the survey, without losing the ability to resolve edges in the migrated images. The method produced results that are better than a comparable common-offset-weighted migration.

Chapter Five: Conclusions

In this study, the topic of seismic acquisition footprint was examined using a numerical modelling approach. Both Kirchhoff and Rayleigh-Sommerfeld modelling methods were shown to be effective for producing datasets suitable for this type of footprint study. In 3D, the efficiency of the Rayleigh-Sommerfeld method with respect to other methods was found to be necessary in order to produce datasets with exhaustive sampling. The approach used in this study, based on producing exhaustive datasets with no spatial aliasing and then decimating those datasets to simulate more realistic but spatially aliased datasets, was shown to be very effective in studying footprint. Using numerically modelled data instead of field seismic data allowed for the true reflectivity to be known so footprint artefacts could be identified conclusively. The approach used in the study also allowed for comparison of different processing methods, in particular prestack migration algorithms, to examine the resulting footprint. The primary conclusions of this study are:

1. Footprint occurs even in images from the exhaustive dataset, manifesting as edge artefacts and aperture imprints. This type of footprint was also observed in the decimated datasets. However, footprint consisting of spatially periodic amplitude variations in the interior of the surveys, similar to that observed in field data and likely produced by inadequate spatial sampling, occurs in images produced from the decimated datasets. This type of footprint varies in strength between images, depending on the different processing algorithms used.

2. Acquisition footprint artefacts manifest as residual migration wavefronts in prestack migrated seismic data. Due to inadequate spatial sampling, the wavefronts do

not interfere completely; i.e. constructively where reflectors and scatterpoints exist, and destructively elsewhere. In 2D source-decimated datasets, the presence of these residual migration wavefronts is coincident with the presence of spatial aliasing in common-receiver gathers; the residual migration wavefronts do not appear to be present in the datasets where common-receiver gathers are unaliased.

3. Prestack migration algorithms have different ways of sorting, regularizing, and weighting the input data, which results in differing abilities to deal with poor sampling. Additional normalizations are performed on traces after migration but before stacking to form the final migrated image. A new method developed in this study, known as delta-ratio weighting, shows potential for reducing footprint artefacts when applied to 2D and 3D model data. Though the method does not address footprint related to the aperture of the survey, it does reduce the severity of footprint artefacts consisting of spatially periodic amplitude variations in the interior of the survey, without losing the ability to resolve edges in the migrated images. In 3D, the method produced results that are better than a comparable common-offset-weighted migration.

Despite the results of this study, many aspects related to the causes and prevention of seismic acquisition footprint in field data remain uncertain. This is partly due to the complexity of the problem. As discussed and demonstrated in this thesis, footprint results from an interaction between many factors, especially in the case of field seismic data. However, the remaining uncertainty surrounding footprint can also be attributed in part to the limitations of this study. In particular, the numerical modelling approach was limited to very simple reflectivity structure, with a small number of flat reflectors and no lateral velocity variations, which is unlike the true subsurface. A more complex

subsurface would result in more complicated wave propagation and scattering, which would affect the manifestation of footprint artefacts. Another factor is related to the acquisition geometries simulated in the study, which were limited to regular decimations with sources and receivers on a flat recording surface, and no moving patch of live receivers, as is common in most industrial surveys. As a result, the conclusions from this study cannot be extrapolated with certainty to apply to these more complicated acquisition and subsurface conditions.

The processing methods used in the study were also limited in some significant ways, which contributed to restricting the applicability of the study. Only a single migration method, Kirchhoff, was used even though other methods are also used in practice. These other methods do not necessarily lend themselves to the application of delta angle weighting schemes as were applied in this study; as a result, the study does not provide insight into footprint reduction in images produced by these other techniques. Also, interpolation was not considered in this study as a means to compensate for poor sampling and to reduce footprint, despite the fact that the technique appears to be gaining favour as the methods become more sophisticated and more effective at dealing with aliased data. Interpolation likely has significant potential to address footprint because, in principle, it is a means for producing exhaustive datasets from more sparsely sampled datasets, and it could be used in conjunction with migration methods other than Kirchhoff.

Of other factors related to footprint that were not considered in this study, amplitude variation with offset (AVO) and noise are likely the most important. While reflection coefficients varied with position in the models, they did not vary with angle of

incidence, and thus did not vary with source-receiver offset, as is the case in the real Earth. This factor is an important consideration as it makes the offset distribution of a given survey geometry more critical. Also, analysis of AVO effects is often carried out in common-image gathers, and the presence of footprint in such gathers can complicate the process. However, this was not examined during the course of the thesis work. Noise is another factor that is likely to have a significant effect on footprint. It is always present in many different forms in field data and in many cases dominates signal in the recorded data and remains with varying severity during processing. The presence of random noise makes the fold distribution of a survey important since stacking is one of the most effective noise attenuation techniques. Coherent noise produces an additional complication as it is generally associated with the slowest velocities in the data and is therefore the most demanding on sampling criteria, and thus most likely to be aliased severely. Coherent noise is also often offset-dependent and as a result, its presence emphasises the effect of the offset distribution of a survey.

To address some of these unresolved issues related to footprint, this study identifies some directions for future work. The first of these suggestions is that noise should be included in future models. Random noise could be easily included, whereas coherent noise simulating surface waves would be more difficult, as it would force the processing applied to the datasets to be more sophisticated; it would need to include some noise attenuation attempts since data entering a stacking or migration process do not usually contain unattenuated coherent noise. Including noise in the modelling would provide insight into footprint in all three processed products (CMP stacks, poststack migrations, and prestack migrations), by producing more realistic footprint artefacts. In

particular, it might help to explain the discrepancy between observations from this study and those from field data processing with regards to the severity of footprint in poststack migrations. The second avenue for future work would be the inclusion of AVO effects and the examination of footprint in common-image gathers. This would help expand our understanding of how the prestack migration weighting schemes affect footprint artefacts before the final stack is produced. Further exploration of the delta weighting schemes is also an area for future work, in terms of more testing of the effectiveness of the method on different datasets with different decimations, and also with different parameters. One such parameter is the choice of binning, which could be extended to include unequal bins, or Gaussian-type bins that overlap, etc.

Nevertheless, this thesis represents a significant step forward in the understanding of seismic acquisition footprint and consists of several original contributions to the subject. In particular, the work demonstrates an effective methodology of numerically modelling exhaustive datasets for the purpose of studying footprint. Also, the particular focus on aliasing and exhaustive vs. decimated sampling was distinct. The study also demonstrated the effectiveness of Rayleigh-Sommerfeld modelling, an often overlooked modelling method, in the production of exhaustive datasets. The model datasets and modelling and migration codes produced will be able to contribute to future studies of footprint. Perhaps most importantly, despite the remaining unanswered questions, it seems clear that the delta-ratio weighting method developed during this study can reduce certain classes of footprint in a Kirchhoff migration algorithm. The method has the potential to be effective in reducing footprint in the processing of field data, or at the very least paves the way for future work in this area.

References

Abma, R., C. Kelley, and J. Kaldy, 2007, Sources and treatments of migration-introduced artifacts and noise: 77th Annual International Meeting, SEG, Expanded Abstracts, 2349-2353.

Aki, K. and P. G. Richards, 2002, Quantitative Seismology, Second Edition: University Science Books.

Al-Bannagi, M. S., K. Fang, P. G. Kelamis, and G. S. Douglass, 2005, Acquisition footprint suppression via the truncated SVD technique: Case studies from Saudi Arabia: The Leading Edge, 24, 832-834.

Albertin, U., H. Jaramillo, D. Yingst, R. Bloor, W. Chang, C. Beasley, and E. Mobley, 1999, Aspects of true amplitude migration: 69th Annual International Meeting, SEG, Expanded Abstracts, 1358-1361.

Audebert, F., P. Froidevaux, L. Nicoletis, and H. Rakotoarisoa, 2003, Migration in the angle domain: an inside view: 65th Conference and Technical Exhibition, EAGE, Expanded Abstracts.

Bancroft, J. C., 2006, A Practical Understanding of Pre- and Poststack Migrations: Society of Exploration Geophysicists.

Beckmann, P., and Spizzichino, A., 1963, The Scattering of Electromagnetic Waves from Rough Surfaces: Pergamon Press Ltd.

Beylkin, G., 1985, Imaging of discontinuities in the inverse scattering problem by inversion of a causal generalized Radon transform: Journal of Mathematical Physics, 26, 99-108.

Bleistein, N., 1987, On the imaging of reflectors in the earth: Geophysics, 52, 931-942.

Bleistein, N., J. K. Cohen, and J. W. Stockwell, Jr., 2001, Mathematics of Multidimensional Seismic Imaging, Migration, and Inversion: Springer.

Canning, A., and G. H. F. Gardner, 1996, Regularizing 3-D data sets with DMO: Geophysics, 61, 1103-1114.

Canning, A., and G. H. F. Gardner, 1998, Reducing 3-D acquisition footprint for 3-D DMO and 3-D prestack migration: Geophysics, 63, 1177-1183.

Cary, P. W., 1999a, Generalized sampling and “beyond Nyquist” imaging: CREWES Research Report, 11, 42.1-42.23.

Cary, P. W., 1999b, Common-offset-vector gathers: an alternative to cross-spreads for wide-azimuth 3-D surveys: 69th Annual International Meeting, SEG, Expanded Abstracts, 1496-1499.

Cary, P., 2007, 2-D Migration Footprint: CSEG Recorder, 32, no. 6, 22-24.

Chiu, S. K., and R. Stolt, 2002, Applications of 3-D data mapping – azimuth moveout and acquisition-footprint reduction: 72nd Annual International Meeting, SEG, Expanded Abstracts, 2134-2137.

Cooper, N., 2004a, A world of reality – Designing land 3D programs for signal, noise, and prestack migration: The Leading Edge, 23, 1007-1014.

Cooper, N., 2004b, A world of reality – Designing land 3D programs for signal, noise, and prestack migration – Part 2: The Leading Edge, 23, 1230-1235.

Cordsen, A., M. Galbraith, and J. Peirce, 2000, Planning Land 3-D Seismic Surveys: Society of Exploration Geophysicists.

Drummond, J. M., A. J. L. Budd, and J. W. Ryan, 2000, Adapting to noisy 3D data – attenuating the acquisition footprint: 70th Annual International Meeting, SEG, Expanded Abstracts, 9-12.

Ebrom, D. A., and J. A. McDonald, eds., 1994, Seismic Physical Modeling: Society of Exploration Geophysicists.

Ersoy, O. K., 2007, Diffraction, Fourier optics, and imaging: Wiley-Interscience.

Gardner, G. H. F., and A. Canning, 1994, Effects of irregular sampling on 3-D prestack migration: 64th Annual International Meeting, SEG, Expanded Abstracts, 1553-1556.

Gazdag, J., 1978, Wave equation migration with the phase-shift method: Geophysics, 43, 1342-1351.

Gazdag, J., 1981, Modeling of the acoustic wave equation with transform methods: Geophysics, 46, 854-859.

Gazdag, J., and P. Sguazzero, 1984, Migration of seismic data by phase shift plus interpolation: Geophysics, 49, 124-131.

Gesbert, S., 2002, From acquisition footprints to true amplitude: Geophysics, 67, 830-839.

Gray, S. H., 1998, Speed and accuracy of seismic migration methods, in L. R. Lines, S. H. Gray, and D. C. Lawton, eds., Depth Imaging of Foothills Seismic Data: Canadian Society of Exploration Geophysicists, 47-83.

Gülünay, N., 1999, Acquisition geometry footprints removal: 69th Annual International Meeting, SEG, Expanded Abstracts, 637-640.

Gülünay, N., F. Martin, and R. Martinez, 1994, 3D data acquisition artifacts removal – spot editing in the spatial-temporal frequency domain: 56th Annual Meeting, EAGE, Abstracts Book, Paper H054.

Jackson, J. D., 1999, Classical Electrodynamics: John Wiley & Sons, Inc.

Jousset, P., P. Thierry, and G. Lambaré, 1999, Reduction of 3-D acquisition footprints in 3-D migration/inversion: 69th Annual International Meeting, SEG, Expanded Abstracts, 1354-1357.

Jousset, P., P. Thierry, and G. Lambaré, 2000, Improvement of 3D Migration/inversion by reducing acquisition footprints: application to real data: 70th Annual International Meeting, SEG, Expanded Abstracts, 866-869.

Krebes, E. S., 2005, Geophysics 551 Seismic Theory and Methods Course Notes: University of Calgary.

Larner, K., R. Chambers, M. Yang, W. Lynn, and W. Wai, 1983, Coherent noise in marine seismic data: Geophysics, 48, 854-886.

Lee, S., J. Willis, and S. Lin, 2005, Migration weights for pre-stack converted wave data to reduce the acquisition footprint: 75th Annual International Meeting, SEG, Expanded Abstracts, 2041-2044.

Liner, C. L., 2004, Elements of 3D Seismology: Pennwell Corporation.

Loewenthal, D., Lu, L., Roberson, R., Sherwood, J., 1967, The wave equation applied to migration: Geophysical Prospecting, 24, 380-399.

Manin, M., and S. Spitz, 1995, Wavefield de-aliasing for acquisition configurations leading to coarse sampling: 65th Annual International Meeting, SEG, Expanded Abstracts, 930-932.

Marfurt, K. J., R. M. Scheet, J. A. Sharp, and M. G. Harper, 1998, Suppression of the acquisition footprint for seismic sequence attribute mapping: Geophysics, 63, 1024-1035.

Margrave, G. F., 2005, Footprint: A look at seismic acquisition geometries using 3D prestack depth migration: CREWES Research Report, 17, Ch. 9.

Margrave, G. F., and R. J. Ferguson, 1999, Wavefield extrapolation by nonstationary phase shift: Geophysics, 64, 1067-1078.

Robinson, E. A., and M. T. Silvia, 1981, Digital Foundations of Time Series Analysis: Volume 2 – Wave-Equation Space-Time Processing: Holden-Day, Inc.

Shearer, P. M., 1999, Introduction to Seismology: Cambridge University Press.

Sheriff, R. E., 2002, Encyclopedic Dictionary of Applied Geophysics, 4th Edition: Society of Exploration Geophysicists.

Trad, D., 2009, Five-dimensional interpolation: Recovering from acquisition constraints: Geophysics, 74, V123-V132.

Trickett, S. R., 2003, F-xy eigenimage noise suppression: Geophysics, 68, 751-759.

Vermeer, G. J. O., 1990, Seismic Wavefield Sampling: Society of Exploration Geophysicists.

Vermeer, G. J. O., 1998, 3-D symmetric sampling: Geophysics, 63, 1629-1647.

Vermeer, G. J. O., 2001, Understanding the fundamentals of 3D seismic survey design: First Break, 19, 130-134.

Wisecup, R. D., 1998, Unambiguous signal recovery above the Nyquist using random-sample-interval imaging: Geophysics, 63, 763-771.

Zhang, Y., J. C. Sun, and S. H. Gray, 2003, Aliasing in wavefield extrapolation prestack migration: Geophysics, 68, 629-633.